

DISSERTATION

FRAGILITY APPROACH FOR PERFORMANCE-BASED DESIGN IN FLUID-STRUCTURE  
INTERACTION PROBLEMS, PART I: WIND AND WIND TURBINES,  
PART II: WAVES AND ELEVATED COASTAL STRUCTURES

Submitted by

Trung Quang Do

Department of Civil and Environmental Engineering

In partial fulfillment of the requirements

For the Degree of Doctor of Philosophy

Colorado State University

Fort Collins, Colorado

Summer 2016

Doctoral Committee:

Advisor: John W. van de Lindt

Paul R. Heyliger  
Hussam N. Mahmoud  
Sammy Zahran

Copyright by Trung Quang Do 2016

All Rights Reserved

## ABSTRACT

### FRAGILITY APPROACH FOR PERFORMANCE-BASED DESIGN IN FLUID-STRUCTURE INTERACTION PROBLEMS, PART I: WIND AND WIND TURBINES, PART II: WAVES AND ELEVATED COASTAL STRUCTURES

This dissertation focuses on a methodology for performance-based design using fragilities in fluid-structures interaction problems. Two types of fluid-structure interaction problems are investigated in this dissertation: Part I: wind-structure interaction (for wind turbine tower-base fatigue), and Part II: wave-structure interaction (for elevated coastal structures subjected to shear and uplift loading).

The first problem type focuses on performance-based design of a wind turbine tower base connection subjected to wind loading using a fatigue limit state. A finite element model for wind turbines is subjected to nonlinear wind loading in the time domain. The relative motion of the actual wind speed and velocity of the moving blades in the along-wind direction creates force nonlinearity for the applied wind load, and hence, necessitates a fluid-structure interaction model. Then, a model for fatigue assessment including crack propagation was developed for the tower base connection. The inclusion of crack propagation is expected to extend the service life of the tower compared to conventional fatigue life analysis using the characteristic S-N approach. By varying the tower thickness, diameter, and considering predefined levels of crack propagation, fragility curves based on a fatigue life limit state are developed for the application of performance-based design. The desired fatigue life of a wind turbine tower for different wind sites can be obtained based on the fragilities. Finally, an illustrative example of performance-

based design for a typical 5-MW wind turbine throughout Colorado is used as an illustrative example in this study.

The second type of problem focuses on development of a performance-based design methodology for elevated coastal structures such as bridges and buildings. Initial numerical results are compared to existing data from a large-scale bridge section test and a full-scale transverse wood wall tested previously at the O.H. Hinsdale Wave Research Laboratory at Oregon State University. These validations provide the foundation for developing a method of wave generation for interaction with bridge and building models. By introducing fragility modeling, a variety of design options can be considered consisting of either raising the elevation of the bridge or strengthening the structure itself in order to obtain the desired probability of failure for a specified of hurricane surge and wave intensity.

## ACKNOWLEDGEMENTS

This material is based upon work supported by the National Science Foundation under Grant No. 1266101 and 1301016 and partial from the DHS Coastal Resilience Center. This material are those of the author and do not necessarily reflect the views of the National Science Foundation.

Sincere thanks to the Vietnam International Education Development - Ministry of Education & Training (VIED-MOET) and the George T. Abell Professorship at Colorado State University for the financial support over the first two years.

I would like to express my deepest gratitude to my advisor, Dr. John van de Lindt, who has supported me kindly and patiently throughout my PhD studies.

My special thanks would be for Dr. Daniel Cox at Oregon State University, the PI of the NSF and DHS projects, who lead me to the coastal engineering field; and Dr. Hussam Mahmoud at Colorado State University whom expertise in fatigue play an important role in my research.

I would like to recognize Dr. Paul Heyliger, Dr. Ellingwood, at Colorado State University who taught me advanced courses in structural engineering, which will guide throughout my academic career.

Finally, I would like to extend my special thanks to my family who always encourage and support my time to study and work in the US.

## DEDICATION

*To my families, my wife Vi Nguyen Thi Diem; my son Kevin Do Kien Vinh; and*

*To the people who suffered from hurricane in coastal area in the world.*

## TABLE OF CONTENTS

ABSTRACT.....	ii
ACKNOWLEDGEMENTS.....	iv
DEDICATION.....	v
TABLE OF CONTENTS.....	vi
LIST OF TABLES.....	viii
LIST OF FIGURES.....	ix
Chapter 1 . INTRODUCTION.....	1
1.1. Wind turbine and fatigue problems.....	1
1.2. Elevated structures in coastal areas.....	6
1.3. Objectives of this Dissertation.....	9
1.4. Organization of This Dissertation.....	10
Chapter 2 . FLUID-STRUCTURE INTERACTION METHODOLOGY.....	12
2.1. Wind and Moving Structures using Finite Element Method (FEM).....	12
2.2. Fluid-Structure interaction modeling.....	15
2.3. ABAQUS modeling for fluid/structure interaction.....	18
2.4. ANSYS modeling for fluid/structure interaction.....	19
Chapter 3 . PROCEDURE FOR FATIGUE LIFE CALCULATION.....	20
3.1. Service fatigue life using S-N curve model (crack initiation).....	21
3.2. Fatigue life after a through-thickness crack (crack propagation).....	23
Chapter 4 . METHOD FOR SIMULATION OF RANDOM PROCESSES.....	27
4.1. Wind field simulation.....	27
4.2. Wave power spectrum for deep and shallow water.....	31
4.2.1. JONSWAP spectrum for deep water waves.....	31
4.2.2. The Texel-MARSEN-ARSLOE (TMA) spectrum for shallow water waves.....	32
4.3. Hurricane Wave Simulation.....	33
Chapter 5 . PERFORMANCE-BASED DESIGN OF A WIND TURBINE USING WIND- STRUCTURE INTERACTION MODEL.....	37
5.1. Fatigue life of a wind turbine tower base connection.....	37
5.1.1. Wind turbine configuration and FEM modeling.....	37
5.1.2. Colorado wind distribution.....	40
5.1.3. Wind turbine under Colorado wind field.....	43
5.1.3.1. Dynamic response of wind turbine FEM model.....	43
5.1.3.2. Fatigue life using S-N curve model (crack initiation).....	46
5.1.3.3. Fatigue life using Paris’s Law Model (crack propagation).....	51
5.2. Performance-Based Design Example Using Fragilities.....	53
Chapter 6 . WAVE-STRUCTURE INTERACTION MODEL VALIDATION USING EXISTING DATA.....	58
6.1. Tsunami loads on wood-frame wall at full scale test.....	58
6.2. Uplift forces on a large scale bridge superstructure.....	62
Chapter 7 . PERFORMANCE-BASED DESIGN OF ELEVATED COASTAL STRUCTURES: ILLUSTRATIVE EXAMPLES.....	66
7.1. Wave loading on elevated coastal structures.....	66

7.1.1. Wave loading on bridges using ABAQUS model.....	66
7.1.2. Wave loading on buildings using the ANSYS Fluent Model.....	73
7.1.2.1. One-story elevated residential building .....	73
7.1.2.2. Two-story elevated residential building.....	83
7.2. Performance-Based design of elevated coastal structures using fragility methodology ....	88
7.2.1. Performance-Based design concept of elevated costal structures .....	88
7.2.2. Performance-Based design of coastal bridge using fragility curves .....	90
7.2.3. Fragility surfaces for Performance-Based design of coastal residential buildings.....	94
Chapter 8 . SUMMARY, CONCLUSIONS, CONTRIBUTIONS, AND FUTURE WORK.....	98
REFERENCES .....	102



## LIST OF TABLES

Table 3-1. Material constants for ASTM A36 Steel (BS7910) .....	26
Table 5-1. Distributed blade structural and aerodynamic properties (Jonkman et al. 2009) .....	37
Table 5-2. Tower properties for the 5-MW wind turbine (Jonkman et al. 2009) .....	38
Table 5-3. Comparison of the FEM model: Natural frequencies comparison .....	40
Table 5-4. Weibull parameters and wind power classification for Colorado sites .....	42
Table 7-1. Sea state from 100-year PDF environmental contour for Gulf of Mexico.....	69

## LIST OF FIGURES

Figure 3-1. Flowchart outlining the procedure for the fatigue life calculation.....	20
Figure 3-2. Development of tower wall through-thickness crack at base.....	24
Figure 4-1. Wind field simulation for 7m/s mean wind speed at 80m.....	28
Figure 4-2. Wind speed at 10m and 80m generated from 7 m/s mean wind speed at 80m .....	29
Figure 4-3. Lognormal PDF mean wind speed distribution for different annual mean wind speeds .....	31
Figure 5-1. Sketch of wind tower and FEM discretization.....	39
Figure 5-2. Weibull distribution for annual mean wind velocity at 90m for Colorado sites.....	43
Figure 5-3. Compare velocity at tip of blade and top of tower to wind velocity for 12m/s mean wind speed at 80m.....	44
Figure 5-4. Acceleration at blade tip and tower top; Stress at tower base for 12m/s mean wind speed at 80m .....	45
Figure 5-5. Shear at blade bases for 12m/s mean wind speed at 80m .....	46
Figure 5-6. Base shear at each blade and total base shear due to blade angles .....	46
Figure 5-7. Fatigue life of a typical 5-MW wind turbine at 8 Colorado sites.....	47
Figure 5-8. Fatigue life due to thicknesses and diameters at 7m/s annual mean wind speed.....	49
Figure 5-9. Wind velocity probability density and output power at four typical sites .....	50
Figure 5-10. Annual mean output power and Fatigue life at 8 sites when TI=14% .....	51
Figure 5-11. Crack growth rate.....	52
Figure 5-12. Maximum crack length .....	52
Figure 5-13. Extended service life after first through-thickness crack.....	53
Figure 5-14. Level 1A FAD (BS7910:2005) .....	53
Figure 5-15. Fatigue life fragility for base Diameter =6.0m, Thickness =35mm.....	55
Figure 5-16. Fatigue life Fragility for Performance-Based Design varying with different base outside diameters (D) and base thicknesses (T).....	56
Figure 5-17. Combination Fatigue Life Fragility for crack propagating to different crack lengths .....	57
Figure 6-1. Tsunami on wall modeling configuration and meshes.....	59
Figure 6-2. Numerical validation for Tsunami loads on transverse wall test at full scale.....	62
Figure 6-3. Test model set up for bridge subjected to waves .....	64
Figure 6-4. Comparison between tested and modeled uplift loading .....	65
Figure 7-1. Full scale bridge section model and numerical wave flume .....	67
Figure 7-2. Environmental contours from deep to shallow water .....	68
Figure 7-3. Transform action for the JONSWAP spectrum to the TMA spectrum for $H_s = 12 m$ , $T_p = 13 s$ , shallow water at height $h = 3 m$ .....	70
Figure 7-4. Generated versus Simulated wave spectrum and generated sea state for $H_s = 12 m$ , $T_p = 13 s$ , $h = 3 m$ .....	70
Figure 7-5. Wave height distribution.....	70
Figure 7-6. Weibull fit for generated wave height distribution .....	70
Figure 7-7. Maximum impact loadings on bridge model .....	72
Figure 7-8. Example of one –story elevated residential building in Carolina Island (www.coastaldesign.com).....	74

Figure 7-9. Model of the one-story elevated near coast building in ANSYS, all windows and doors are opened .....	75
Figure 7-10. Fluid domain meshed for one-story elevated building in ANSYS .....	76
Figure 7-11. Define of surge level and clearance height .....	77
Figure 7-12. Rendering of the volume fraction for the sea water phase.....	78
Figure 7-13. Total shear force for different wave heights at surge level = 3m.....	79
Figure 7-14. Total shear force for different surge levels at $H_s = 9$ m, $T_p = 10.8$ sec .....	80
Figure 7-15. Total uplift force for different wave height at surge levels of 3.0 m .....	81
Figure 7-16. Total uplift force for different surge levels at $H_s = 9$ m, $T_p = 10.8$ sec .....	82
Figure 7-17. Mean of peak up lift and shear per unit width for one-story building .....	83
Figure 7-18. Example of two –story elevated building in Carolina Island (www.coastaldesign.com).....	84
Figure 7-19. Model for two-story elevated building in ANSYS, all windows and doors are closed .....	85
Figure 7-20. Mesh of the fluid domain for two-story building in ANSYS with smaller elements near the building surfaces .....	86
Figure 7-21. Wave-structure interaction for $H_s = 12m$ , $S = 1.5m$ .....	87
Figure 7-22. Mean of shear force and uplift force per unit width for the two-story building .....	88
Figure 7-23. Conceptual fragility curves for elevated coastal structures.....	89
Figure 7-24. Procedure for constructing a fragility curve for structure under wave load .....	90
Figure 7-25. Fragility curves for impact loading on structure .....	92
Figure 7-26. Design example using fragility curves for the same probability of failure.....	93
Figure 7-27. Design example using fragility curves to reduce probability of failure.....	94
Figure 7-28. Fragility surfaces for shear during a 3-hour hurricanes .....	96
Figure 7-29. Fragility surfaces for uplift during 3-hour hurricanes.....	96
Figure 7-30. Fragility curves for shear at surge level of 3.0m during three-hour hurricanes .....	97
Figure 7-31. Fragility curves for uplift at surge level of 3.0m during three-hour hurricanes .....	97

## Chapter 1 . INTRODUCTION

This dissertation is a combination of two projects. The first project focuses on a modeling of wind turbine using Morison's equation special for fatigue life estimation and performance based design of wind turbine tower based connection. The second project focuses on developing a performance based design methodology for elevated coastal structures such as bridges and buildings. In order to predict the hurricane wave uplift and shear forces on elevated structure, numerical model for fluid/structures interaction problem has been employed. Since the two projects share the same procedure for wind/wind turbine and wave/elevated coastal structure, the dissertation is organized to cover the two problems in one general fluid/structure interaction problem. The results presented in this dissertation have been published in three journal papers<sup>1,2,3</sup> with one additional paper in progress.

### 1.1. Wind turbine and fatigue problems

Wind energy is systematically becoming a more economical, sustainable, and safe solution for alternative energy in lieu of fossil fuels. After the 2011 earthquake in Japan, nuclear leaks from the Fukushima nuclear plant have highlighted the need for adopting safer energy sources. The vast increase in the use of hydro power in developing countries this decade, on one hand, has been protested by environmental activists because of its impact to the environment

---

<sup>1</sup> Do, T., Mahmoud, H., and van de Lindt, J. (2014). "Fatigue Life of Wind Turbine Tower Bases throughout Colorado." *Journal of Performance of Constructed Facilities*, ASCE, 10.1061/(ASCE)CF.1943-5509.0000612, 04014109.

<sup>2</sup> Do, T. Q., van de Lindt, J. W., and Mahmoud, H. (2015). "Fatigue Life Fragilities and Performance-Based Design of Wind Turbine Tower Base Connections." *Journal of Structural Engineering*, ASCE, 141(7), 1–13.

<sup>3</sup> Do, T. Q., van de Lindt, J. W., and Cox, D. T. (2016). "Performance-Based Design Methodology for Inundated Elevated Coastal Structures Subjected to Wave Load." *Engineering Structures*, Elsevier, 117, 250-262. [doi:10.1016/j.engstruct.2016.02.046](https://doi.org/10.1016/j.engstruct.2016.02.046).

which remains unknown for years. Solar energy, although one of the most reliable sources of energy, is still considered by most to be too expensive for general use. Wind energy, which is available almost anywhere, is a reasonable alternative over conventional energy in the modern world (Morgan 2010). In the early 1990s the wind energy industry experienced rapid growth and construction increased by more than 500%. This decade was also marked by a shift to megawatt-size wind turbines as well as offshore wind power (Manwell et al. 2009). Generally, wind energy is harvested by wind turbines, which generate electricity from rotating motion excited by wind force.

Since 2011 the U.S. has experienced a 90% increase in installation of wind power equipment, leading to a significant increase in wind energy production in 2012, which contributed to 42% of the total annual energy capacity additions. In the U.S., Colorado is among the top ten states producing wind power with a cumulative contribution of 3.8% (3,301 MW) in place as of the end of 2012 (Wiser and Bolinger 2013). Although the cost of installing onshore wind farms in the U.S shows a slightly decreasing trend (from 2,154 USD/kW in 2010 down to 1,940 USD/kW in 2012), it is still too high compared to other countries such as China, Denmark, and India, with the cost of 1,354, 1,367, 1,460 USD/kW in 2010, respectively (IRENA 2012). In the breakdown of onshore wind power cost, the wind turbine typically accounts for 64% of the total cost. The tower itself accounts for a quarter of the cost (IRENA 2012). Refined the design of the wind turbine tower may reduce the cost of wind power.

From the structural engineering perspective, wind turbines can be compared to high rise buildings with a low frequency and heights ranging from 60m-160m. A typical modern wind turbine consists of a 3-blade- upwind-horizontal axis rotor mounted on top of a fabricated steel tube tower. Wind towers and rotor blades with lengths reaching up to 60-100m are more

sensitive to aerodynamics but are becoming quite common in wind farms around the world. A number of research projects have been conducted to develop coupled numerical models for wind towers and blades that are capable of modeling response to wind load. Current wind turbine practices use aerodynamic analysis tools such as the FAST (Fatigue, Aerodynamic, Structures, and Turbulence) code (Jonkman and Buhl Jr. 2005) and ADAMS (Automatic Dynamic Analysis of Mechanical Systems) with A2AD (ADAMS to Aero Dynamic) code (Laino and Hansen 2001).

Another common method of wind turbine analysis is the so called multi-body dynamics approach (Murtagh et al. 2005; Saravia et al. 2013). The idea of this method is to set up the equations of motion for each part of a structure separately and then apply compatibility conditions (constraints) to link these parts. Therefore, some higher vibration modes can be considered or eliminated in the analysis due to the level of accuracy required such as coupling of bending and torsion (Jeong et al. 2013; Kooijman 1996). Murtagh et al. (2005) developed a model to couple the rotating blades and tower under wind loading using modal analysis. Because of the large size of the rotating blades, wind forces acting on blades can change depending on the position of blades. The base shear that results from this complex dynamic interaction of the blades will then be transferred to the tower, thereby changing its dynamics. Chen et al. (2009) used the same procedure to investigate the coupling vibration and applied the finite element method (FEM) to analyze turbine behavior. Their study indicated that there is a significant difference in the top tower displacement for the coupled and non-coupled models. Quilligan et al. (2012) developed a Lagrangian energy conservation method to construct the equation of motion in the fore-aft direction. These equations are solved in the time-domain. Wind data is typically processed in the frequency-domain since it is a stationary Gaussian process. However, a method for converting

the wind spectral density based on an inverse Fourier Transform to a wind velocity time series is often applied (e.g. Aas-jakobsen and Strommen 2001; Murtagh et al. 2004).

Unlike many other engineering structures, wind turbines are designed for a target economical life of 20 years (Manwell et al. 2009; Nijssen 2007), primarily because of fatigue related failure of the turbine components. Since wind turbines are not designed for occupant comfort, wind-induced vibrations can be higher than in a typical building. However, large vibrations can lead to damage accumulation resulting in fatigue failure, especially at the tower base connections where dynamic stress concentrations are generally high. This type of damage has also been observed in other slender structures subjected to wind loads such as transmission towers and traffic poles (e.g. Dawood et al. 2013; Goode and van de Lindt 2007; Madsen and Frandsen 1984; Repetto and Solari 2010).

The total fatigue life of any detail generally consists of the crack initiation stage and the crack propagation stage. Fatigue analysis of the initiation phase is typically conducted using the “S-N curve” approach (AASHTO 2012; Goode and van de Lindt 2007) while the crack propagation phase is analyzed using different crack propagation models; the most common of such is the “Paris Law” (Paris and Edorgan 1963). In structural engineering design codes such as the American Society of Testing and Material (ASTM) and the American Association of State Highway and Transportation Officials (ASSHTO), the aforementioned approach is used to provide a relationship between stress range and number of cycles that will produce a through-thickness crack under service live load. However, the development of a through-thickness crack does not mean that the detail has reached the end of its fatigue life. Fatigue cracks are known to propagate in a stable manner until the crack length is too large to tolerate and fracture occurs.

The S-N curve fatigue assessment method is based on time domain as well as frequency domain. In frequency domain, a stationary Gaussian processes is assumed for wind loading effects developed from the assumption of a narrow-band process (Crandall and Mark 1963), Closed-Form Solution (CFS) based on a wide-band process (Holmes 2002) or even a combination of narrow-banded Gaussian processes (Jiao and Moan 1990). Recently, an improvement to CFS was proposed by Repetto et al. (2009; 2012), which is believed to provide slightly conservative approximations for predicting total damage and fatigue life. While not much computational demand is needed in the frequency domain, complex vibration response calculations under various loading conditions as well as large computer memory are required in order to apply a time domain approach. Numerical algorithms are adopted for constructing the histogram for the number of cycles at each stress level (stress-range histogram) in order to calculate the accumulated fatigue damage (Frese and Dalhoff 2000; Goode and van de Lindt 2006, 2007; Kumar and Stathopoulos 1998; Xu et al. 2009). Despite its computational demand, the benefits of working in the time domain is that it can capture the force nonlinearity in the fluid/structure interaction problem (Morison 1953). This approach was utilized in this study to apply the nonlinear wind loading in the coupled dynamic model.

In part I of this dissertation, the focus will not be on developing a new advanced model for wind turbine analysis. However, a simplified model using FEM, which considers the along-wind vibration only in the time-domain, is developed to obtain the bending stress as a time series. This time-history stress is an essential input for the fatigue assessment including fatigue crack propagation as a post analysis stage. The developed FEM is validated by comparing the predominate frequencies and mode shapes to the those presented in Jonkman et al. ( 2009) to ensure that the simplified model is a close representation to their system analysis. It is worth



noting that the simplified model used herein does not account for the variation of wind speed along the horizontal plane, which will result in torsional effects. The results of the simulations are used to develop fragilities for application of performance-based design to the wind turbine baseplate-to-tower welded connection. The design charts are based on key design variables (tower base diameter, thickness, and a predefined level of crack propagation) for a welded connection at the tower base only.

## **1.2. Elevated structures in coastal areas**

Part II of this dissertation focuses on another performance-based design type. As a result of global climate change, many experts anticipate an increase in hurricane disasters along the coastal area of the U.S. with potential implications demonstrated by hurricane Ivan (2004), Katrina (2005) and Ike (2008), and most recently Sandy (2012). Elevated structures are one of the solutions to mitigate the damage and reduce risk to buildings and bridges along the coast by reducing the impact flow of surge and/or waves during hurricanes. In some surveys, structures fail or survive with just 0.5 m (1.6 ft) difference in elevation (Kennedy et al. 2011). The wave impact forces include shear (lateral wave force), uplift from underneath the structure, and overturning moment which all can result in significant damage to many types of structures including highway bridges (Cuomo et al. 2009; Padgett et al. 2008). In addition, coastal and near-coast structures must resist forces due to buoyancy and hydrodynamic drag resulting from currents associated with hurricane surge.

A large body of research exists for wave loading on fixed and floating ocean and coastal structures and was conducted for offshore oil platforms, rubble-mound port structures and vertical caisson, etc. (Goda 2000; Sarpkaya and Isaacson 1981). Early laboratory studies in shallow water wave loading on elevated structures were conducted using small scale hydraulic

models under simplified geometry and wave forces (Gramhry 1963; Kaplan 1992; Kaplan et al. 1995; Wang 1970). These studies focused on predicting the uplift forces including buoyancy, slamming force, drag force as well as inertial force. These forces reflect not only the wave characteristics but also the dynamic response of the structures and often the fluid-structure interaction between the waves and structure. Later in 1999, a series of tests on the offshore oil platforms exposed to hurricane wave-in-deck load (Bea et al. 1999) in Gulf of Mexico were conducted. Those tests showed that clearance height between still water level and the lower deck of the platform is the critical parameter for designing an elevated structure subjected to waves as one might expect. Other important parameters are the wave height crest and its probability distribution such as the peakedness of the sea state. Some follow up research projects used different probability distributions such as the Rayleigh distribution for the wave crests in deep water (Kriebel and Dawson 1993), wave overtopping (Cox and Scott 2001) or a truncated Weibull distribution for significant wave height ( $H_s$ ) and peak period ( $T_p$ ) (Mori and Cox 2003) were also conducted. However, most of the research has focused on deep water waves, and there is less guidance for shallow water impacts, particularly for elevated coastal structures.

A series of wave loading tests were conducted in the O.H. Hinsdale Wave Research Laboratory at Oregon State University to determine quasi-static equations for wave loadings on structures. In 2011, Bradner et al. performed a test on a 1:5 scale concrete bridge superstructure section under hurricane wave loads (Bradner et al. 2011). Differences between dynamic and static forces have been observed experimentally. In 2013, a full scale test of light frame wood shear wall under tsunami load was tested by Linton et al. (2013) and confirmed that the transient loading was 2.2 times that of the quasi-static force. The Goda equation (Goda 2000) is felt by many to present state-of-the-art for predicting the static shear and uplift loading on a vertical

caisson. Following this equation, Wiebe et al. (Wiebe et al. 2014) developed the Goda pressure formula for horizontal wave loads on elevated structures and validated it with small scale tests.

Laboratory testing is both time consuming and costly and thus many researchers have focused on development of robust computational fluid dynamics (CFD) models that can replicate test results. In a CFD model, Navier Stokes equations are the governing equations and the basic tool for modeling fluid dynamics in both deep and shallow water. In 2010, Bozorgnia et al. (Bozorgnia et al. 2011) used the commercial CFD code STAR CCM+ to apply the finite volume method to solve the governing fluid equations. Using this method, the effect of entrapped air on wave impact and uplift forces on a 2D model of a bridge section was investigated. Recently, Chen et al. (Chen et al. 2014) used another open source package called OpenFOAM to investigate wave-structure interaction. ABAQUS is a robust general commercial tool that can also be applied to this type of problem. In 2013, Como and Mahmoud (Como and Mahmoud 2013) used the Eulerian-Lagrangian model in ABAQUS to study the impact loading on light-frame wood walls subjected to tsunami debris.

In order to introduce performance-based design for elevated coastal structures, one option is the development and application of fragility curves. Fragilities are conditional probability distributions which represent the conditional probability of the demand exceeding a specific limit state or capacity as a function of one or more hazard intensities. Constructing fragility curves for performance-based design using fragility curves is not a new design concept. In 1996, the Federal Emergency Management Agency (FEMA) funded a large project in performance-based design for buildings subjected to earthquake (FEMA 1996). The fragility concept was then studied by Rosowsky and Ellingwood (Rosowsky and Ellingwood 2002) for wood frame housing for both wind and earthquake hazard. In earthquake engineering, the hazard intensity can be the

spectral acceleration for a specified fundamental period of building. In wind engineering, performance based design for wind turbine tower base connections was introduced recently by Do et al. (Do et al. 2015).

In part II of this dissertation, a procedure for performance-based design of elevated coastal structures for hurricane waves using the fragility methodology is introduced and demonstrated on several illustrative examples. ABAQUS finite element and ANSYS models were validated based on existing laboratory test data. A series of numerical simulations using an Eulerian-Lagrangian formulation for a variety of combinations of significant wave height and peak wave period were conducted. Then, fragilities for bridges and buildings designs (elevation and inundation level) were developed. The procedure to select a combination of structure elevation and strength/capacity using fragilities to achieve the desired performance level (in this case failure probability) is then illustrated on several examples.

### **1.3. Objectives of this Dissertation**

This doctoral dissertation entitled: “*Fragility Approach For Performance-Based Design in Fluid-Structure Interaction Problems*” is presented in two parts with part I with the following objectives:

Part I: Performance-Based Design of wind turbine support towers:

- 1) Method for the design of wind turbine for fatigue related problem of the tower base connection.
- 2) Development of a simplified but fully coupled dynamic model for investigation of the effects of rotating blades on vibration of wind turbines with the movement of the flexible structure in a simulated wind field; specially for use in fatigue studies.

- 3) Develop fragility curves that can be used as design aids for selection of basic wind turbine tower design parameters based on a specific site location having a specific average mean wind speed.
- 4) Develop method for performance-based design for fatigue.
- 5) Method for estimating service life of wind turbine tower based on fatigue and crack propagation.

#### Part II: Performance-based Design of Elevated Coastal Structures

- 6) Model of wave-structure interaction for quantitative understanding the reactions of elevated coastal structures subjected to hurricane wave and surge in a combination based on the comprehensive analytical and experimental test results.
- 7) Develop performance-based design methodology for coastal elevated structures based on a conditional probability for exceeding key thresholds such as collapse, and force levels under various combination of statistical sea states
- 8) Provide basic engineering approaches for improving structure safety for those types of buildings and mitigating property loss.

### **1.4. Organization of This Dissertation**

This dissertation is divided into eight chapters.

Chapter 1 entitled “*Introduction*”, presents the background and development of performance-based design using fragility curves with potential applications for wind turbines and coastal structures.

Chapter 2 entitled “*Fluid-Structure interaction methodology*” introduces two different models: wind/wind turbine using finite element method, and wave/elevated coastal structures using ABAQUS and ANSYS packages.

Chapter 3 entitled “Procedure for Fatigue Life Calculation” explains the model for estimating fatigue life of a connection based on fatigue and crack propagation.

Chapter 4 entitled “*Method for simulation of random processes*” explains the methods for wind field and hurricane wave simulation which generate time series of wind and wave data from statistical data (power spectrum and type of distribution).

Chapter 5 entitled “*Performance-based design and fatigue life of wind turbine tower base connections*” introduces performance-based design for fatigue, and the estimation of fatigue life of wind turbine tower based connections based on the remaining life cycles to initiate a crack and crack propagation until the structure collapses.

Chapter 6 entitled “*Wave-structures interaction model validation using existing data*” uses the two existing data sets to validate the ABAQUS and ANSYS models.

Chapter 7 entitled “*Performance-based design of elevated coastal structures: illustrative examples*” presents several illustrative examples for elevated coastal structures using numerical models developed earlier in this dissertation.

Chapter 8 is entitled “*Summary, Conclusions, Contributions, and Future work*”

### 2.1. Wind and Moving Structures using Finite Element Method (FEM)

The dynamic model for a wind turbine can be found in many commercial structural analysis soft-ware packages. In general, they can be classified in three types as described by Lee et al. (2002). The classifications include a combination of multi-body dynamics and assumed-modes or modal analysis approach which are widely adopted in wind turbine analysis to capture the coupling between the rotating blades and flap-wise vibration of the blades and towers (Murtagh et al. 2004, 2005; Quilligan et al. 2012). The finite element method is believed to provide more robust results but at high computational cost (Lee et al. 2002). Chen et al. (2009) used this approach together with Newmark's method for analyzing a coupled dynamics model in the time domain. For most of the aforementioned methods, a quasi-static model representing the wind loading is applied. However, Goode and van de Lindt (2006, 2007) used a FEM to analyze the dynamic response of a high mast lighting support in which the relative wind velocity acting on a moving tower (Morison's model) was taken into account. The approach presented in the current study proposes combining a FEM and multi-body dynamics to describe not only the coupling between the rotating blades and tower but also the coupling between the moving structure and wind loading (resulting in nonlinear forces) in the time domain. Thus, the quasi-static loading hypothesis is no longer adopted.

First, the vibrations of the rotating blades are considered. While the blades rotate, wind loads acting on the blades will change due to the position of the blades. Since the lengths of the blades are quite large (60 to 100m), there is a substantial difference in wind velocity at the base and tip of the blade. Therefore, the rotating speed of the blades will affect the wind load cycles

and load intensities on the blades. In this model, the blades and tower are simplified and divided into frame elements. The equation of motion for a blade in the flap-wise direction only can be written as:

$$M_B(\ddot{x}_B + \ddot{x}_{Ttop}) + C_B\dot{x}_B + K_Bx_B = F_B(t) \quad (2-1)$$

where,  $M_B$ ,  $C_B$ , and  $K_B$  are mass, damping and stiffness matrices of a blade;  $\ddot{x}_{Ttop}$  is the acceleration of top tower;  $\ddot{x}_B$ ,  $\dot{x}_B$  and  $x_B$  are the acceleration, velocity and displacement vectors of the blades, respectively.

While the mass and stiffness matrix can be obtained directly from blade geometry, the damping matrix was computed assuming Rayleigh damping. The appearance of  $\ddot{x}_{Ttop}$  in Equation (2-1) is analogous to ground acceleration which is well recognized in earthquake engineering. However, this term was eliminated in this study if the top tower acceleration is very small compared to the blade tip acceleration.

As passing through the wind turbine, wind flow generates both lift force and drag force on the blades. In this paper, only drag force, which is normal to the rotating plane is considered since the lift force has a minor effect on the flap-wise direction compared to the drag force (Quilligan et al. 2012). This is felt to be consistent with the simplified numerical model employed for the purposes of investigating fatigue estimation modeling of wind turbine tower bases in this paper. Also in this direction, by taking into account the moving speed of blades and tower the wind load on each blade,  $F_B(t)$ , is determined based on the relative wind velocity at each node on the blade (Morison 1953) as:

$$F_B(t) = \frac{1}{2} \rho_{air} A_n C_d u_{rel}(t) |u_{rel}(t)| \quad (2-2)$$



where,  $\rho_{air}$  is air density;  $A_n$  are vector of nodal projected areas in wind direction;  $C_d$  is the vector of drag coefficients, which change along the blade because of blade twisting and geometries over its length.

While only flap-wise vibration is considered, the relative velocity of wind at each blade node is represented as:

$$u_{rel}(t) = u_{wind}(t) - \dot{x}_B(t - \Delta t) - \dot{x}_{Ttop}(t - \Delta t) \quad (2-3)$$

where  $\dot{x}_{Ttop}(t - \Delta t)$  is velocity at the top of the tower at time  $t - \Delta t$ . In this model, the relative velocity at time  $t$  is updated from the velocity of the structure from the previous step  $t - \Delta t$  when  $\Delta t$  is small.

The total base-shear of each blade can be obtained by solving Equation 1 for each time step. By balancing kinetic forces at each node, the total base-shear at the base of each blade can be written as:

$$Q_B(t) = \sum_{i=1}^{n_B} K_B x_B(t) = \sum_{i=1}^{n_B} [F_B(t) - M_B \ddot{x}_B(t) - C_B \dot{x}_B(t)] \quad (2-4)$$

in which,  $n_B$  is the number of blade nodes. This procedure is repeated for the second and third blades. Although all blades have the same characteristics, the difference in their initial positions (angles) results in different base shears at least in their phase angles. So, the total base shear of the three blades is typical not equal to three times the base shear of a single blade at any point in time.

The vibration of the second body in the multi-body problem, namely the tower, can then be expressed as:

$$M_T \ddot{x}_T + C_T \dot{x}_T + K_T x_T = F_T(t) + \sum_{j=1}^3 Q_{B_j}(t) \quad (2-5)$$

in which,  $\sum_{j=1}^3 Q_{B_j}(t)$  is the total base shears from the three rotating blades;  $\ddot{x}_T$ ,  $\dot{x}_T$ ,  $x_T$  are acceleration, velocity and displacement vectors of the tower;  $M_T, C_B, K_T$ : and mass, damping, stiffness matrices of the tower. A concentrated mass at the top of the tower consists of a lumped mass of the top tower element, the mass of the rotor (including the three blades) and the nacelle mass;  $F_T(t)$  is the relative wind force vector acting on the tower nodes and identified by applying the same procedure to the  $F_B(t)$ .

When the blades pass through the tower, there will be a reduction in wind loading acting on the tower. This may affect the fatigue life of the tower but has not been included in this study. The reader is again reminded that this simplified coupled dynamic model is only developed for the fatigue analysis. For design of wind turbines under extreme wind loading, other dynamic effects of wind turbines such as flutter instability as well as responses at non-resonant conditions, the effects of blade and other loading characteristic (time-varying/frequency content) could be taken into account by using the FAST (Fatigue, Aerodynamics, Structures, and Turbulence) or ADAMS (Automatic Dynamic Analysis of Mechanical Systems) codes which are commonly used in practice

## 2.2. Fluid-Structure interaction modeling

The equations of motion for fluid are traditionally expressed by Navier-Stokes equations for mass conservation and momentum conservation.

The principal of mass conservation for fluid problem can be express as change rate of mass in a fix volume in time is equal to the net rate of mass flow across the surface. The mathematical statement is known as the continuative equation as:

$$\frac{\partial \rho}{\partial t} + \frac{\partial \rho u_i}{\partial x_i} = 0 \quad (2-6)$$

where,  $\rho$  is fluid density;  $t$  is time,  $x_i$ 's are coordinate system  $(x, y, z)$ , and  $u_i$ 's are velocity components  $(u, v, w)$ .

For expressing wave/structure interaction, the equations can be limited to incompressible fluids, which means that the fluid density,  $\rho$  is a constant and independent of pressure. Therefore, the continuative equation can be express as:

$$\frac{\partial u_i}{\partial x_i} = 0 \quad (2-7)$$

The full expression of the Equation (2-7) is as below:

$$\frac{\partial u}{\partial x} + \frac{\partial v}{\partial y} + \frac{\partial w}{\partial z} = 0 \quad (2-8)$$

The principal of momentum conservation is expressed based on the Newton's Second Law of motion for fluid dynamic which states that "the time rate of change of linear momentum of a given set of particles is equal to the vector of sum of all the external forces acting on the particles of the set, provided Newton's Third Law of action and reaction govern the internal forces" (Reddy and Gartling 2010). The mathematical statement for near incompressible flow can be written as

$$\rho \frac{\partial u_i}{\partial t} = -\frac{\partial p}{\partial x_i} + \frac{\partial \tau_{ij}}{\partial x_j} + \rho f_i \quad (2-8)$$

where,  $p$  is pressure;  $f_i = (f_x, f_y, f_z)$  are the source term;  $f_x = fu, f_y = fv, f_z = -g$ ;  $f = 2\Omega \sin \phi$  is the Coriolis parameter (earth rotation effect),  $\Omega$  is angular rate of revolution,  $\phi$  is geographic latitude, and  $g$  is gravity acceleration.

For near incompressible Newtonian fluid, the viscous stress tensor,  $\tau_{ij}$ , can be express as the function of the velocity field and viscosity,  $\mu$ , as

$$\tau_{ij} = \rho\mu \left( \frac{\partial u_i}{\partial x_j} + \frac{\partial u_j}{\partial x_i} \right) \quad (2-9)$$

Spatial derivative of stress tensor:

$$\frac{\partial \tau_{ij}}{\partial x_j} = \rho\mu \frac{\partial}{\partial x_j} \left( \frac{\partial u_i}{\partial x_j} \right) + \rho\mu \frac{\partial}{\partial x_j} \left( \frac{\partial u_j}{\partial x_i} \right) = \rho\mu \frac{\partial}{\partial x_j} \left( \frac{\partial u_i}{\partial x_j} \right) + \rho\mu \frac{\partial}{\partial x_i} \left( \frac{\partial u_j}{\partial x_j} \right) \quad (2-10)$$

It is noted that  $\frac{\partial u_j}{\partial x_j} = \frac{\partial u_i}{\partial x_i} = 0$  is the continuative equation stated in Equation (2-7), then

the second term in the right hand side of Equation (2-10) is vanished, therefore:

$$\frac{\partial \tau_{ij}}{\partial x_j} = \rho\mu \frac{\partial}{\partial x_i} \left( \frac{\partial u_j}{\partial x_j} \right) \quad (2-11)$$

Substitute Equation (2-11) into equation (2-8) the equation for conservation of momentum can be written as

$$\rho \frac{\partial u_i}{\partial t} = -\frac{\partial p}{\partial x_i} + \rho\mu \frac{\partial}{\partial x_i} \left( \frac{\partial u_i}{\partial x_j} \right) + \rho f_i \quad (2-12)$$

The full expression of the Navier- Stokes equation with regardless to the earth rotation effects can be written as

$$\begin{aligned} \frac{\partial u}{\partial x} + \frac{\partial v}{\partial y} + \frac{\partial w}{\partial z} &= 0 \\ \rho \frac{\partial u}{\partial t} + \frac{\partial p}{\partial x} - \rho\mu \frac{\partial}{\partial x} \left( \frac{\partial u}{\partial x} + \frac{\partial u}{\partial y} + \frac{\partial u}{\partial z} \right) &= 0 \\ \rho \frac{\partial v}{\partial t} + \frac{\partial p}{\partial y} - \rho\mu \frac{\partial}{\partial y} \left( \frac{\partial v}{\partial x} + \frac{\partial v}{\partial y} + \frac{\partial v}{\partial z} \right) &= 0 \\ \rho \frac{\partial w}{\partial t} + \frac{\partial p}{\partial z} - \rho\mu \frac{\partial}{\partial z} \left( \frac{\partial w}{\partial x} + \frac{\partial w}{\partial y} + \frac{\partial w}{\partial z} \right) + \rho g &= 0 \end{aligned} \quad (2-13)$$

The above expression is called the Eulerian form of the Navier- Stokes equation which have four equations and four unknowns ( $u, v, w$ , and  $p$ ).

For solving the fluid/structure interaction problem, Lagrangian form should be considered. The relation between the position of a particle and its velocities can be written as

$$x_i = X_i + f(u_i, t, \frac{\partial u_i}{\partial t}) \quad (2-14)$$

where,  $x_i$ 's are the final positions and  $X_i$ 's are the initial positions.

The boundary conditions for the Navier- Stokes equation is usually expressed as

$$\begin{aligned} \tau_{ij}\theta_j - p\theta_i &= \bar{\sigma}_{ni} & \text{on } \Gamma_\sigma \\ u_i\theta_i &= \bar{u}_n & \text{on } \Gamma_n \\ u_i\xi_i &= \bar{u}_t & \text{on } \Gamma_t \end{aligned} \quad (2-15)$$

where,  $\theta_i$ 's are the components of the tangent vector to the surface boundary, and  $\xi_i$ 's are the components of the normal vector to the surface boundary.

### 2.3. ABAQUS modeling for fluid/structure interaction

The coupled fluid/structure in ABAQUS model the structure with a Lagrangian formulation, the fluid with a Eulerian formulation with the underlying assumption that the water can be modeled as a viscous and incompressible Newtonian fluid (ABAQUS 2011a). A linear equation of state represented in the Hugoniot form (ABAQUS 2011b) was also employed to determine pressure as a function of fluid density and internal energy per unit mass. Three parameters are required to define the water using this representation, namely density (1030 kg/m<sup>3</sup> for sea water), the speed of sound in water (1500 m/s), and the dynamic viscosity (0.001 kg/m/s at 20°C). The Eulerian–Lagrangian general contact approach (ABAQUS 2011a) was applied for this analysis with the assumption of zero friction tangential to surfaces.

In this dissertation, the two existing laboratory wave flume test were used to verify the ABAQUS model and were demonstrated in Chapter 6. The simulation method then was applied to investigate wave loading (uplift and shear) on the I-10 bridge section at full scale.

#### **2.4. ANSYS modeling for fluid/structure interaction**

In addition to ABAQUS, ANSYS is another computational tool for modeling hurricane wave and structure. In this dissertation, 3D models for one-story and two-story elevated residential building in coastal region were investigated using ANSYS.

Wave-structure interaction problems can be divided into two types: one-way fluid-structure interaction for a rigid structure (concrete buildings or bridges), and two-way structure interaction for flexible structures with dynamic effects considered (wood/steel buildings). One-way fluid/structure problems can be modeled in ANSYS by using only the Fluent module (ANSYS 2013). For this type of problem, structures are assumed to be rigid and acting as the fixed boundary of the fluid volume.

On the other hand, two-way fluid/structure problems are modeled in two different parts namely the structure domain and the fluid domain. The two domains share common pressure and displacement/velocity at the contact surfaces. After each time step, the stress at the contact surface of the fluid domain will be the load for the structure and then the displacements of the structure are updated for the fluid boundaries.

### Chapter 3 . PROCEDURE FOR FATIGUE LIFE CALCULATION

The procedure for calculating the total fatigue life is outlined in the flowchart shown in Figure 3-1. As shown in the Figure, the total life is comprised of a crack initiation stage and a crack propagation stage. The following two subsections describe the analysis associated with crack initiation and crack propagation in more detail.

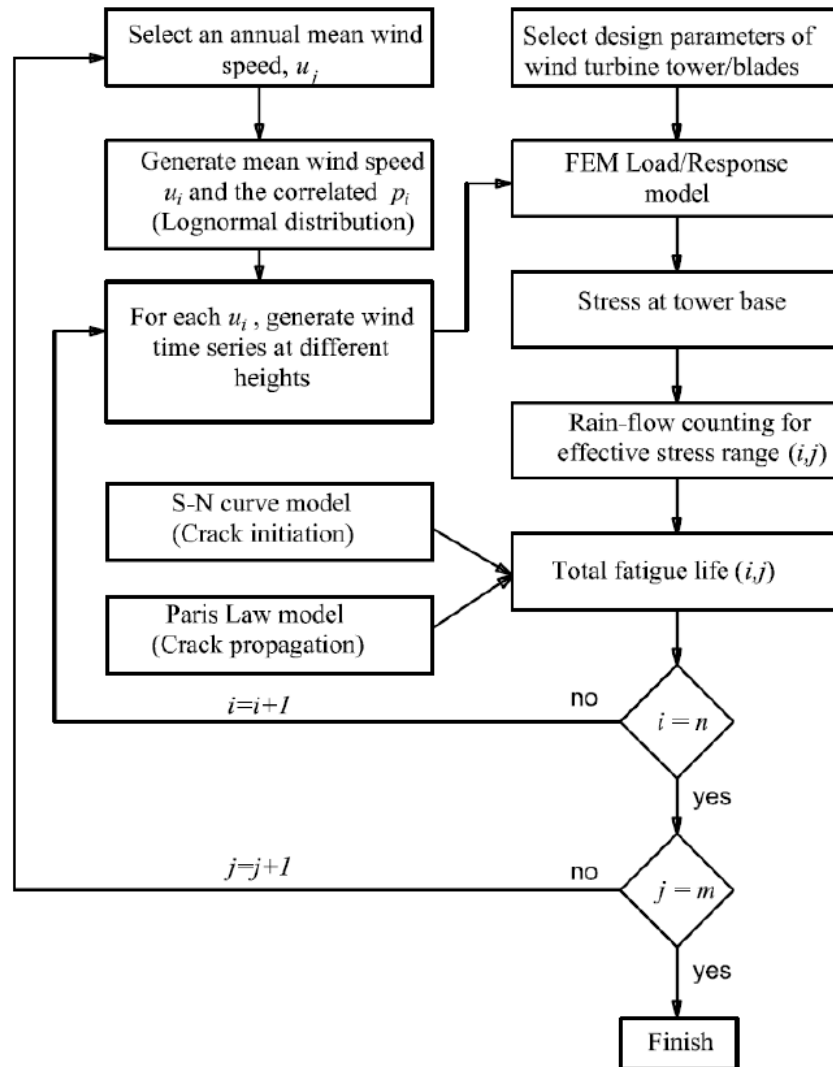


Figure 3-1. Flowchart outlining the procedure for the fatigue life calculation

### 3.1. Service fatigue life using S-N curve model (crack initiation)

For a given time series of wind velocity, the equation of motion for the tower is solved numerically using Newmark's method (Newmark 1959). The method had been condensed in step-by-step for easier use by Chopra (Chopra 2012). Then, moment at the tower base,  $M(t)$  can then be obtained from the finite element model (FEM) as:

$$M(t) = \sum_{k=i}^{n_T} h_k F_k(t) \quad (3-1)$$

where  $n_T$  is the number of tower nodes,  $h_k$  is the lever arm of the total nodal force in the flap-wise direction at node  $k$  (distance from tower base to node  $k$ );  $F_k = K_T x_T(t)$  is the dynamic force in the flap-wise direction at node  $k$ .

Once stress at the tower base is obtained by applying basic mechanics, a rain-flow counting method (Matsuichi and Endo 1968) is applied to construct the stress histogram. The effective stress range is then obtained using Palmgren-Miner's rule (Miner 1945)

$$S_{reff} = \left( \sum f_i S_{ri}^3 \right)^{\frac{1}{3}} \quad (3-2)$$

where  $S_{ri}$  and  $f_i$  are the  $i^{th}$  stress range and its probability of occurrence from the stress histogram. Based on S-N curve approach (AASHTO 2012), the number of cycles of the weld connection at tower base for the  $i^{th}$  wind speed can be determined as:

$$N_i = AS_{reff}^m \quad (3-3)$$

where  $A$  and  $m$  are the fatigue constant parameters for each detail category.

For a narrow-band random stress history, the expected frequency is the average number of zero up-crossings per unit time,  $\nu_0^+$  (Crandall and Mark 1963). Therefore, if only the  $i^{th}$  mean wind speed is acting on the wind turbine for the entire year, the expected fatigue life for the tower base connection can be expressed as:



$$FL_i = \frac{N_i}{v_0^+(365)(24)(3600)} [\textit{year}] \quad (3-4)$$

Using the service life over the yearly cycle and the assumed damage accumulation, the total service life to crack initiation can be computed using the Palmgren-Miner rule (Miner 1945), as:

$$F_{life} = \frac{1}{\sum_{i=1}^n D_i P_i} [\textit{year}] \quad (3-5)$$

in which,  $F_{life}$  is the computed fatigue life in years,  $P_i$  is the probability of occurrence of the  $i^{th}$  wind speed, and  $D_i = \frac{1}{FL_i}$  is the expected damage corresponding to the  $i^{th}$  wind speed.

Regarding fatigue constant parameters, many studies have shown that the slope of the S-N curve does not change much while the fatigue constant has substantial uncertainty (Hanaki et al. 2010). Although the standard for wind turbines is the International Electro-technical Commission (IEC) 61400 (Manwell et al. 2009), fatigue and fracture assessment also can be considered under other codes with more testing data available for fatigue analysis such as American Welding Society (AWS), ASSHTO, and British Standard (BS7910). As defined in ASSHTO, detail category E was assumed for the base fillet welded connection in this study, then  $m = 3.0$  (fixed) and  $A = 36.1 \times 10^{10} \text{ MPa}^3$  which was modeled as a lognormal distribution with mean  $\mu_A = 65.9 \times 10^{10} \text{ MPa}^3$  and  $\text{COV} = 0.26$  (Chung et al. 2003). The Monte-Carlo simulation method was then applied to generate  $A$  (e.g. 10,000 values). For detail category  $E$ , the threshold stress for fatigue was set to  $31 \text{ MPa}$  (AASHTO 2012). Any effective stress range less than half of this threshold value will not affect the service fatigue life (Dowling 2007) and was therefore neglected.

### 3.2. Fatigue life after a through-thickness crack (crack propagation)

After the tower experiences a through-thickness crack, the remaining fatigue life due to crack propagation can still be substantial. In fact, the crack will continue to propagate gradually after each cycle until it reaches the critical size where brittle fracture occurs after certain cycles of loading (Mahmoud and Dexter 2005). However in current design codes, the fatigue life associated with crack propagation is not accounted for. The reason for this is because the philosophy in design codes is that it is more conservative to ignore the fatigue life due to crack propagation. Consequently, most experimental fatigue data do not include the life associated with crack propagation. The procedure for estimating the propagation rate of cracks is determined by the Paris Law (Paris and Edorgan 1963):

$$\frac{da}{dN} = C(\Delta K_{eff})^m \quad (3-6)$$

where  $C$  is the crack growth rate coefficient,  $\Delta K_{eff}$  is the effective stress intensity factor range, which depends on the effective stress range ( $S_{reff}$ ) and crack length ( $a$ ) as well as other geometric factors, and  $m$  is a material constant. Closed-form solutions for the stress intensity factors have been widely published in various resources and are well defined in British Standard (BS7910 2005). Since the ratio of wall thickness and curve radius for this problem exceeds the limit of a defined curve shell member ( $R/T \geq 100$ ), a flat plate for through-thickness crack will be assumed to compute stress intensity range, therefore:

$$\Delta K_{eff} = \Delta K_{Ieff} = Y(S_{reff})\sqrt{\pi a} \quad (3-7)$$

where  $S_{reff}$  can be a value that represents a constant amplitude stress range or an effective stress range that accounts for the time-variation of the stress range.

Since the plate width is very large compared to crack length, the assumption of an infinite width plate will be applied. On the other hand, the tower is under bending stress only (no membrane terms) and it is assumed that there is no misalignment, so,  $Y = 1$ .

By applying a closed-form solution (Dowling 2007), the number of cycles the structure can withstand after the first initial crack ( $N_{if}$ ) for each annual mean wind speed is defined as

$$N_{if} = \frac{a_f^{1-m/2} - a_i^{1-m/2}}{C(\Delta S\sqrt{\pi})^m(1-m/2)} \quad (3-8)$$

where  $\Delta S = S_{reff}$  is the effective stress range for the  $i^{th}$  mean wind speed, and  $a_i$  is initial crack length which can be set as the detectable crack size or the visible through-thickness crack. This crack can be an initial flaw or in this case, is the through-thickness crack due to fatigue defined by the S-N curve. It can be assumed that when a through-thickness crack appears, the crack length is already double the wall thickness (Figure 3-2a).

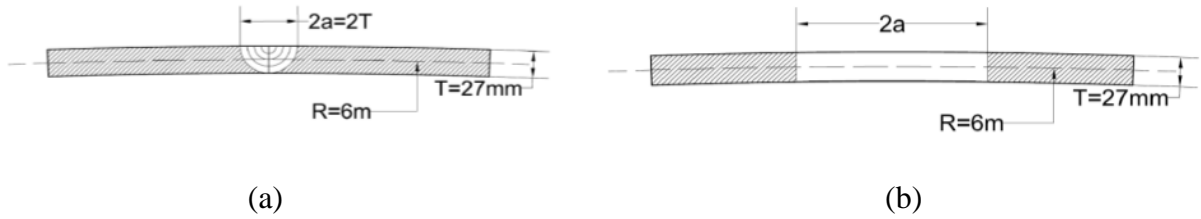


Figure 3-2. Development of tower wall through-thickness crack at base

The final crack length,  $a_f$ , is the crack length that can be tolerated before plastic collapse, and will be determined by applying Fatigue Assessment Diagram (FAD) level 1A represented in BS7910 (2005). Some parameters needed for this procedure are listed below:

Fracture ratio at each mean wind speed

$$K_r = \frac{K_I}{K_{Ic}} \quad (3-9)$$

where  $K_I = S_{t,max}\sqrt{\pi a}$  is stress intensity factor for an infinite width flat plate (BS7910 2005),  $S_{t,max} = \left[SCF \left(\frac{S_{reff}}{2} - \frac{P}{A}\right) + \sigma_s\right]$  is the maximum tensile stress at tower base, and  $\frac{P}{A}$  is the compressive stress due to dead load. The stress concentration factor (SCF) can be taken as 1.5 for a fillet weld (BS7910), and  $\sigma_s$  is the secondary stress or residual stress which is equal to the yield strength of the material (BS7910), and  $K_{Ic}$  the is toughness of the material from a Charpy V-Notch Impact test.

The load ratio at each mean wind speed can be expressed as:

$$S_r = \frac{S_{ref}}{S_f} \quad (3-10)$$

where the reference stress,  $S_{ref} = \frac{S_{reff}}{2} + \frac{P}{A}$  is the primary stress for an infinite width plate and  $S_f = \frac{1}{2}(\sigma_y + \sigma_u) \leq 1.2\sigma_y$  is the mean value of yield strength and ultimate tensile strength.

Based on a level 1A (BS7910) for an acceptable region, while making sure the load ratio ( $S_r$ ) is less than 0.8 (no plastic collapse) and setting the stress intensity factor ( $K_r$ ) equal to 0.707, the critical crack length then can be determined as:

$$a_f = a_c = \frac{1}{\pi} \left( \frac{0.707 K_{Ic}}{S_{t,max}} \right)^2 \quad (3-11)$$

All the material constants in Equations (3-6), (3-8), (3-9), and (3-11), are provided in Table 3-1.

By substituting  $a_f$  into Equation (3-8), the number of cycles the tower base can withstand without plastic collapse while the crack propagates from its initial length ( $a_i$ ) to final length ( $a_f$ ) is determined. If one considers the fatigue life after the first crack (i.e., accounting for the crack propagation), then the extended service life for each annual mean wind speed can be written as:

$$\hat{F}_{life} = \frac{1}{\sum \hat{D}_i \cdot P_i} \quad (3-12)$$

where,  $\hat{D}_i = \frac{v_0^+(3600)(24)(365)}{N_{if}}$  is the expected damage of the  $i^{th}$  mean wind speed,  $P_i$  is the probability of occurrence of the  $i^{th}$  mean wind speed,  $v_0^+$  is the expected frequency of the stress process for each mean wind speed.

Table 3-1. Material constants for ASTM A36 Steel (BS7910)

Variable	Value
$K_{Ic}$	100 $MPa\sqrt{m}$
$C$	$1.65 \times 10^{-11} \frac{m/cycle}{(MPa\sqrt{m})^3}$
$m$	3
$\sigma_y$	250 $MPa$
$\sigma_u$	400 $MPa$

## Chapter 4 . METHOD FOR SIMULATION OF RANDOM PROCESSES

In this Chapter, the generation of two different random processes is explained, namely a wind field and shallow water waves, with applications presented later in this dissertation for wind turbine tower fatigue analysis and uplift forces on coastal structures, respectively. Both provide the loading for their respective analyses and illustration of the fragility methodology for performance-based design.

### 4.1. Wind field simulation

Wind speed at a specific site is normally represented by an “annual mean wind speed” at a reference height from the ground. For each annual mean wind speed and its assumed distribution type, a probability density function (PDF) is plotted. The area under each PDF curve will be divided into a number of bins. The average value of wind speeds at each bin represents the “mean wind speed” at the reference height. Mean wind speeds at different heights are also computed by the logarithmic law. Finally, wind time series or “wind speed” was generated for each mean wind speed. The wind speed in the along wind direction at height  $h$  can be expressed as:

$$U(h, t) = U_m(h) + u_h(t) \quad (4-1)$$

The mean wind speed at height  $h$ ,  $U_m(h)$ , follows the logarithmic law (Holmes 2004):

$$U_m(h) = u_i \frac{\ln(h) - \ln(z_0)}{\ln(h_0) - \ln(z_0)} \quad (4-2)$$

where  $u_i$  is the mean wind speed measured at reference height  $h_0$ ,  $z_0$  is surface roughness.

Fluctuating wind speed at height  $h$ ,  $u_h(t)$  was determined by taking the inverse Fourier Transform of the wind power spectral density (PSD) with spatial correlation (Aas-jakobsen and Strommen 2001). However, only vertical correlation is of interest herein for the Kaimal wind

spectra in the along wind direction instead of the von Kármán spectra (Simiu and Scanlan 1986). With this simple wind field model, every point in the horizontal direction which has the same height will experience the same wind velocity at the same time (Figure 4-1)

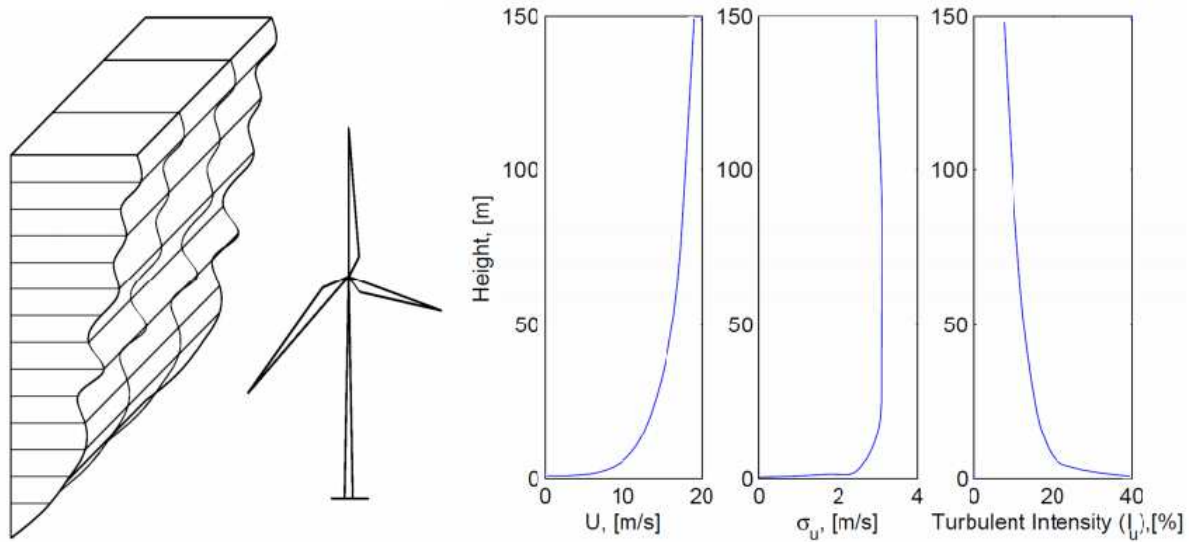


Figure 4-1. Wind field simulation for **7m/s** mean wind speed at **80m**

In order to simulate the wind field, several other parameters must be identified. For discussion, assume the mean wind speed is measured at 80m height for an open terrain site. The vertical height varies from 0 to 150m (the highest position of the wind turbine blades tip) and is modeled in 10m increments. The cut-in and cut-off wind frequencies are selected to capture up to a three-min return period (180 sec) and the frequency range is 0.005Hz to 6Hz with an increment of 0.005Hz. The selection of cut-in frequency and increment are important for wind time-history simulation. A lower cut-in frequency and smaller increment will result in higher turbulence intensity. An example for generating a 7m/s mean wind speed at 80m elevation for a duration of 3600 seconds is illustrated in Figure 4-1 and Figure 4-2. However, this procedure does not need to be used when the wind data in the time domain is available from field measurements.

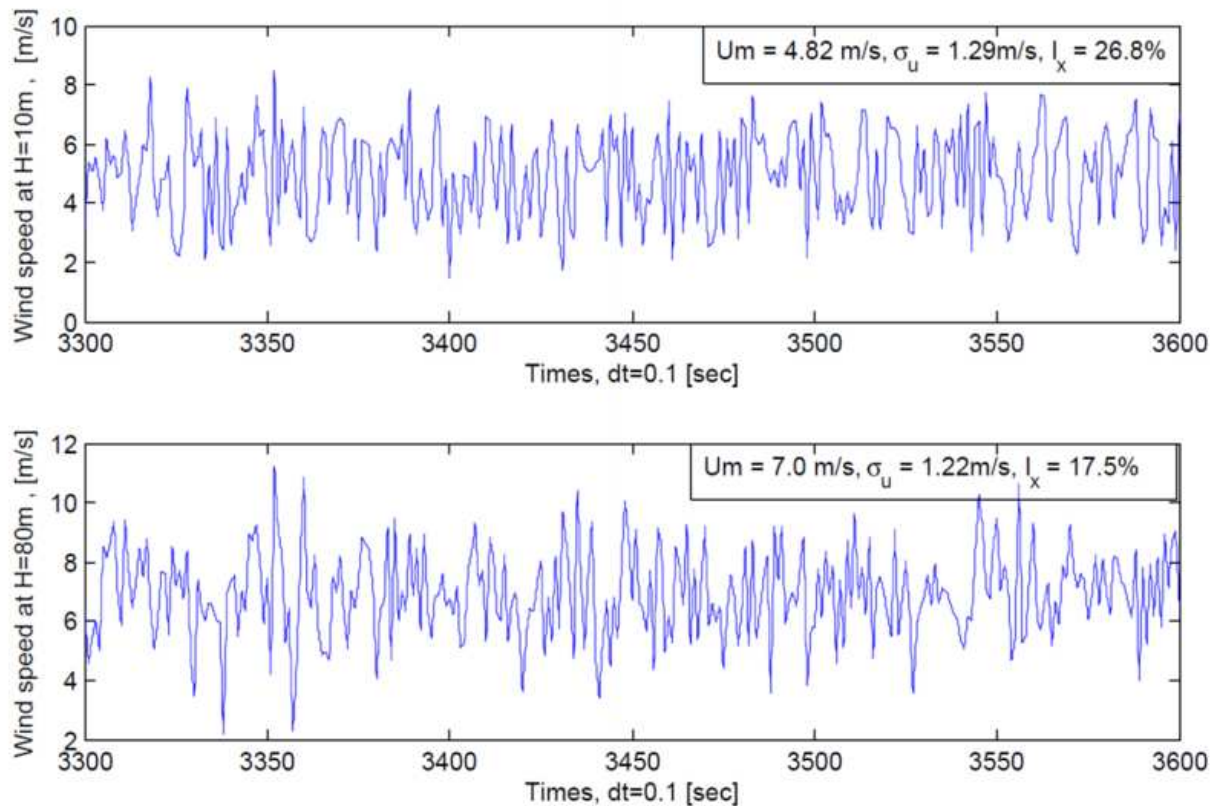


Figure 4-2. Wind speed at 10m and 80m generated from 7 m/s mean wind speed at 80m

The selection of annual mean wind speed and its turbulence intensity depends on the wind site itself. Noda and Flay (1999) indicated that the mean annual wind speed and its turbulence intensity for a typical site in New Zealand are 10m/s and 17.5%, respectively with a mean annual wind speed of 7m/s with 15% turbulence for an overseas site. In this study, the annual mean wind speed at an elevation of 80m was varied from 6 m/s to 12 m/s with 17.5% turbulence. These values are representative of the state of Colorado from 30 years of NOAA data (Atadero et al. 2008). The lognormal distribution produced from the National Oceanographic and Atmospheric Administration (NOAA) data for the contiguous United States was used to generate the time series shown earlier. The probability distribution function (PDF) can be written as:



$$f_U(u) = \frac{1}{\sqrt{2\pi}\zeta u} \exp \left[ -\frac{1}{2} \left( \frac{\ln u - \lambda}{\zeta} \right)^2 \right] \quad (4-3)$$

where,  $\zeta$  and  $\lambda$  are shape and scale parameters (mean and standard deviation of lognormal distribution), and are defined in term of normal mean ( $\mu$ ) and standard deviation ( $\sigma$ ) of annual mean wind speed distribution as  $\zeta^2 = \ln \left( 1 + \frac{\sigma^2}{\mu^2} \right)$  and  $\lambda = \ln \mu - \frac{1}{2}\zeta^2$ . While  $\mu$  can be set to be equal to the selected annual mean wind speed at 80m above ground level,  $\sigma$  was determined by assuming the annual mean wind speed distribution to have the same coefficient of variance ( $\sigma = \mu COV = 0.35\mu$ ). For each selected annual mean wind speed, the corresponding PDF is plotted as shown in Figure 4-3. Each PDF was then divided into 51 bins each representing different mean wind speeds ( $u_i$ ), within the PDF which were used for determining the dynamic response of the wind turbine. The area under each bin represents the probability of occurrence ( $p_i$ ) for each mean wind speed ( $u_i$ ) (Goode and van de Lindt 2007).

It is important to note that the wind speed distribution over a short time period used for dynamic analysis was described by the normal distribution while the annual mean wind speed was defined by the lognormal distribution.

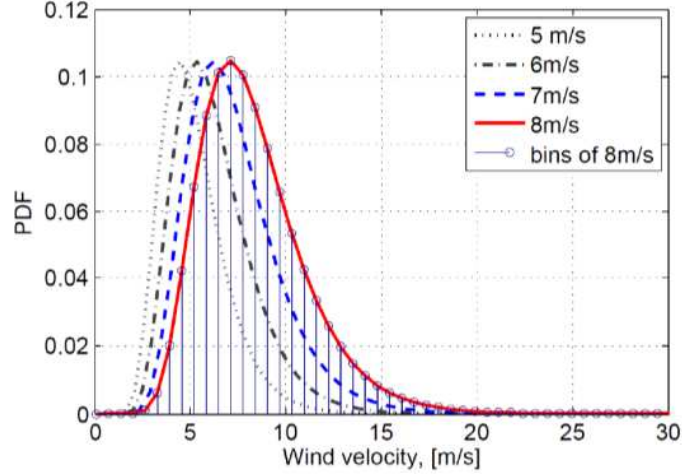


Figure 4-3. Lognormal PDF mean wind speed distribution for different annual mean wind speeds

## 4.2. Wave power spectrum for deep and shallow water

The generation of shallow water waves is typically performed by modifying a deep water sea state power spectral density function.

### 4.2.1. JONSWAP spectrum for deep water waves

The Joint North Sea Wave Observation Project (JONSWAP) started in 1967 and simultaneously measured the wave and wind 160 km away from the island of Sylt in the Germany Bight, and applied the results to develop the JONSWAP spectrum for deep water sea waves (Hasselmann et al. 1973). The original spectral formula,  $S_J(f)$ , showed the fetch dependence of the wave spectrum as

$$S_J(f) = \frac{\alpha g^2}{f^5 (2\pi)^4} \exp\left[-\frac{5}{4}\left(\frac{f}{f_m}\right)^{-4}\right] \gamma \exp\left[-\frac{(f-f_m)^2}{2\sigma^2 f_m^2}\right] \quad (4-4)$$

where  $\gamma$  = peak shape parameter,  $\gamma = 3.3$  as an average;  $f_m$  = model frequency,  $f_m = 3.5(g/U)\bar{x}^{-0.33}$ , also recognized as peak frequency,  $f_p$ ;  $\alpha = 0.076\bar{x}^{-0.22}$ ,  $\sigma = 0.07$  for  $f \leq f_m$  and  $0.09$  for  $f > f_m$ ;  $\bar{x} = gx/U_{10}^2$  dimensionless fetch;  $U_{10}$  = mean wind speed at 10 m;

and  $g =$  gravity. For hurricane-associated wave spectra in the U.S., the JONSWAP spectrum was modified to match the measurement of four major hurricanes (Ochi 2003). The modified JONSWAP spectrum in term of significant wave height and peak frequency is expressed as

$$S(f) = \frac{4.5g^2H_s^2 f_p^4}{(2\pi)^4 f^5} \exp \left[ -0.125 \left( \frac{f}{f_m} \right)^{-4} \right] (9.5f_p H_s^{0.34}) \exp \left[ -\frac{(f-f_p)^2}{2\sigma^2 f_p^2} \right] \quad (4-5)$$

in which the two parameters,  $\alpha$  and  $\gamma$  from the original spectrum can be derived as

$$\alpha = 4.5f_p^4 H_s^2; \quad \gamma = 9.5f_p H_s^{0.34};$$

#### 4.2.2. The Texel-MARSEN-ARSLOE (TMA) spectrum for shallow water waves

The TMA spectrum was developed to reproduce wind-generated finite depth water gravity waves and was named by Hughes (Hughes 1984) as a result of research conducted by Bouws et al. (Bouws et al. 1985), which was used in the field verification and development of the spectrum. The name TMA is a combination of the first three letter of the three data sets: Texel, MARSEN (the Marine Remote Sensing Experiment at the North Sea), and ARSLOE (the Atlantic Remote Sensing Land-Ocean Experiment). The experiments covered the wind speed measured at 10 m ranging from 4 to 25 m/s with a sea bed slope ranging from 1:150 to nearly flat, and with water depths between 5 and 45 m. The TMA spectrum effectively transforms the infinite depth sea spectrum (JONSWAP) to finite depth water,  $h$ , as

$$S_{TMA}(f, h) = S_J(f) \Phi(\omega, h) \quad (4-6)$$

where

$$\Phi(\omega, h) = \left[ \frac{k^{-3}(\omega, h) \frac{\partial k(\omega, h)}{\partial \omega}}{k^{-3}(\omega, \infty) \frac{\partial k(\omega, \infty)}{\partial \omega}} \right] \quad (4-7)$$

is the transform function. The numerical expression for  $\Phi(\omega, h)$  was developed by Kitaigordskii et al (Kitaigordskii et al. 1975) as

$$\Phi(\omega_h) = \{K(\omega_h)\}^{-2} \left[ 1 + \frac{2\omega_h K(\omega_h)}{\sinh(2\omega_h^2 K(\omega_h))} \right]^{-1} \quad (4-8)$$

where  $\omega_h = \omega\sqrt{h/g}$  and  $K(\omega_h)$  can be determined from the constraint  $K(\omega_h) \tanh(\omega_h^2 K(\omega_h)) = 1$ .

### 4.3. Hurricane Wave Simulation

While deep water wind-generated waves can often be treated as Gaussian, waves in shallow water are non-Gaussian due to high crests and shallow troughs as the waves near the shore and the water becomes shallower. Recent studies have focused on the simulation of non-Gaussian time series which match both the power spectral density (PSD) and the probability density function (PDF). These simulation methods vary from direct simulation to iterative methods. Direct simulation includes ARMA models for non-Gaussian signals (Lawrance and Lewis 2014; Li and Li 2012) and Hermite polynomials which generate non-Gaussian processes from a Gaussian process (Winterstein 1988). Iteration methods first generate a Gaussian process from the target PSD then transform them into a non-Gaussian process. The simulated spectrum may be distorted from the target PSD and PDF. The updated PSD is then computed for the next iteration until the simulated PSD and PDF match the target. These iterative methods are well explained by Yamazaki and Shinozuka (Yamazaki and Shinozuka 1988) and further developed by Grigoriu (Grigoriu 1998) by introducing the covariance function of the translation.

Methods for simulating non-Gaussian processes have been developed for more efficient and accurate simulation of the free surface. Deodatis and Micaletti (Deodatis and Micaletti 2001) modified the Yamazaki and Shinozuka iteration algorithm in order to generate a highly skewed probability distribution. Another method introduced by Masters and Gurley (Masters and Gurley 2003) used cumulative distribution function mapping instead of conventional probability

distribution functions. For generating a broad range of non-Gaussian processes using Monte Carlo simulation, Grigoriu (Grigoriu 2009) proposed translation models for the process which can handle both direct and inverse problems of an arbitrary prescribed marginal distribution function. Recently, a simple and efficient translation process has been developed for a general non-Gaussian stationary stochastic vector process (Shields and Deodatis 2013a), and for non-Gaussian and non-stationary stochastic processes (Kim and Shields 2015; Shields and Deodatis 2013b).

The present study focuses on the original iterative method for non-Gaussian simulation proposed by Yamazaki and Shinozuka (Yamazaki and Shinozuka 1988) simply as a tool to reproduce shallow water wave sea states. The non-Gaussian sea state was simulated from the target PSD for shallow water (TMA spectrum), and the prescribed random water wave PDF. After several iterations, the PSD of the simulated wave provides a reasonable match to the target PDS power spectrum as well as the prescribed wave height distribution. A reasonable match is defined here as having an area under the PSD of within 5% of the TMA spectrum. The expression for converting a Gaussian process to a non-Gaussian process was written as

$$\eta = F^{-1}(\Phi(\eta_o)) \quad (4-9)$$

where,  $\eta_o$  is Gaussian sea state,  $\eta$  represents non-Gaussian sea state,  $F^{-1}$  is the inverse of prescribed cumulative distribution function (CDF) of a non-Gaussian sea state, and  $\Phi(\eta_o)$  is standard normal CDF of Gaussian sea state.

The prescribed wave distribution is traditionally assumed to be a Weibull distribution. Once the target TMA spectrum and the sea state are defined, the Biésel transformation function (Biésel and Suquest 1951) is then applied to transform the height of the generated wave to the displacement of the wave paddle in the time domain. For the numerical flume presented by the

simulation procedure described earlier in this paper, the paddle was not modeled. Instead, the movement was replaced by the paddle velocity applied directly to the fluid block as the boundary conditions at one end of the flume. Therefore, the original Biésel transformation function was modified to obtain the paddle velocity instead of the paddle displacement. The procedure for getting wave paddle velocity is as below:

- 1- Choose the cut-in and cut-off frequencies,  $f_{min}$  and  $f_{max}$ , and the resolution of the spectrum,  $N$ . The TMA spectrum is divided into  $N$  bins. The width of each bin denotes the frequency resolution ( $\Delta f = (f_{max} - f_{min})/N$ ). Random sea wave are then assumed to be the combination of  $N$  single harmonic waves.
- 2- The  $i^{th}$  single wave has frequency  $f_i$  ( $f_i = f_{min} + i\Delta f - \frac{\Delta f}{2}$ ). The area under each bin represents the discrete wave energy spectrum,  $\sigma_\eta^2(f_i)$

$$\sigma_\eta^2(f_i) = S_{TMA}(f_i)\Delta f \quad (4-10)$$

- 3- Compute wave amplitude for the  $i^{th}$  wave

$$a_i = \sqrt{2\sigma^2(f_i)} \quad (4-11)$$

- 4- Compute time series elevation for the  $i^{th}$  wave with random phase  $\delta_i$

$$\eta_i(t) = a_i \cos(2\pi f_i t + \delta_i) \quad (4-12)$$

- 5- Compute the Biésel transform function

*For hinged-type wave maker*

$$B_i(z) = \frac{h+z}{h} \frac{k_i h}{2 \sinh(k_i h)} \frac{[\sinh(k_i h) \cosh(k_i h) + k_i h]}{[1 - \cosh(k_i h) + k_i h \sinh(k_i h)]} \quad (4-13)$$

*For piston-type wave maker*

$$B_i = \frac{\sinh(k_i h) \cosh(k_i h) + k_i h}{2 \sinh^2(k_i h)} \quad (4-14)$$

- 6- Transform time series sea state to time series wave paddle movement for single wave

$$x_i(t, z) = B_i(z)\eta_i(t) = B_i(z)a_i \cos(2\pi f_i t + \delta_i) \quad (4-15)$$

$$v_i(t, z) = B_i(z) \frac{\partial}{\partial t} \eta_i(t) = B_i(z)a_i [2\pi f_i \sin(2\pi f_i t + \delta_i)] \quad (4-16)$$

7- Compute the time series sea state and time series wave maker velocity

$$\eta(t) = \sum_{i=1}^N \eta_i(t); \quad x(t, z) = \sum_{i=1}^N x_i(t, z); \quad v(t, z) = \sum_{i=1}^N v_i(t, z) \quad (4-17)$$

8- Apply this velocity profile to the numerical flume model in ABAQUS and get the sea state spectrum at the desire location ( $S_i$ ). Compare the generated wave spectrum and the target TMA spectrum, compute the ratio  $\xi = \frac{S_i}{S_{TMA}}$

9- Multiply  $v(t, z)$  in step 7 with  $\xi$  and repeat step 8 until  $S_i = S_{TMA}$

After obtaining the input velocities ready for wave generation, a finite element model for the water flume was generated in the ABAQUS and ANSYS environments. Details of the finite element model will be discussed later.  $H_s$  and the wave spectrum at a specific location in the numerical wave flume were collected and compared to the values from the TMA spectrum. The values will also depend on the location of the measured point in the flume. Therefore, changing the measuring location allows  $H_s$  to be closed to the target values. A velocity coefficient for different  $H_s$  and the height of the numerical water flume was also applied to obtain the target significant wave. This adjustment coefficient was applied to account for the simplification of the numerical wave flume boundary conditions. In this study, the bottom of wave flume was modeled as having zero velocity or no-slip condition while water can slide freely along the side walls (free slip condition) of the numerical flume.

Chapter 5 . **PERFORMANCE-BASED DESIGN OF A WIND TURBINE USING WIND-  
STRUCTURE INTERACTION MODEL**

**5.1. Fatigue life of a wind turbine tower base connection**

*5.1.1. Wind turbine configuration and FEM modeling*

The configuration of a typical 5-MW wind turbine is described in Table 5-1. Since the configurations of blades are complicated, these numbers will be used as the input to the FEM for the blades. The blades were modeled using 17 frame elements with 6 degrees of freedom at each node. Although only flap-wise vibration was considered, edge-wise stiffness, axial stiffness as well as the torsional constant was also taken into account.

**Table 5-1.** Distributed blade structural and aerodynamic properties (Jonkman et al. 2009)

Node	RNodes (m)	BMassDen (kg/m)	FlpStff (N.m2)	EdgStff (N.m2)	GJStff (N.m2)	EASStff (N.m2)	AeroTwst (°)	Attack angle	$C_d$
1	2.87	767.89	1.91E+10	1.95E+10	5.36E+09	1.07E+10	13.31	103.31	0.50
2	5.60	607.25	1.12E+10	1.54E+10	3.59E+09	7.83E+09	13.31	103.31	0.50
3	8.33	409.22	5.81E+09	8.46E+09	1.69E+09	4.67E+09	13.31	103.31	0.35
4	11.75	425.85	4.65E+09	7.17E+09	8.47E+08	4.17E+09	13.31	103.31	1.35
5	15.85	352.32	2.54E+09	5.03E+09	3.32E+08	3.13E+09	11.48	101.48	1.39
6	19.95	338.17	2.02E+09	4.47E+09	2.57E+08	2.58E+09	10.16	100.16	1.39
7	24.05	320.56	1.55E+09	3.95E+09	1.96E+08	2.11E+09	9.01	99.01	1.38
8	28.15	293.02	1.05E+09	3.38E+09	1.39E+08	1.59E+09	7.80	97.80	1.38
9	32.25	260.56	6.41E+08	2.68E+09	7.79E+07	1.14E+09	6.54	96.54	1.40
10	36.35	234.83	3.78E+08	2.17E+09	5.37E+07	8.70E+08	5.36	95.36	1.45
11	40.45	192.46	2.15E+08	1.49E+09	3.28E+07	6.07E+08	4.19	94.19	1.45
12	44.55	160.55	1.18E+08	1.11E+09	1.99E+07	5.01E+08	3.13	93.13	1.45



13	48.65	134.48	8.40E+07	7.56E+08	1.54E+07	3.53E+08	2.32	92.32	1.46
14	52.75	102.81	5.50E+07	4.85E+08	8.54E+06	2.27E+08	1.53	91.53	1.46
15	56.17	86.87	3.72E+07	3.76E+08	6.62E+06	1.72E+08	0.86	90.86	1.46
16	58.90	67.77	2.54E+07	2.74E+08	5.17E+06	9.69E+07	0.37	90.37	1.46
17	61.63	46.26	7.89E+06	8.73E+07	2.23E+06	3.09E+07	0.11	90.11	1.46

The tower was modeled using ten frame elements with an equal element length. The sketch of the original tower is as shown in Figure 5-1. For the performance-based design, stiffness and mass of the tower elements were computed using the FEM based on Table 5-2.

**Table 5-2.** Tower properties for the 5-MW wind turbine (Jonkman et al. 2009)

Variable	Value	
Tower mass density	8.5	<i>kg/m<sup>3</sup></i>
Base diameter	6	<i>m</i>
Top diameter	3.87	<i>m</i>
Base thickness	0.035	<i>m</i>
Top thickness	0.025	<i>m</i>
The Young's modulus	210	<i>GPa</i>
Shear modulus	80.8	<i>GPa</i>
Tower height	87.6	<i>m</i>
Structural damping ratio	1	<i>%</i>
Hub Mass (at top of tower)	56,780	<i>kg</i>
Nacelle Mass (at top of tower)	240,000	<i>kg</i>
Blades Mass (3 Blades - at top of tower)	35,220	<i>kg</i>
Blades rotation velocity	12.1	<i>rpm</i>

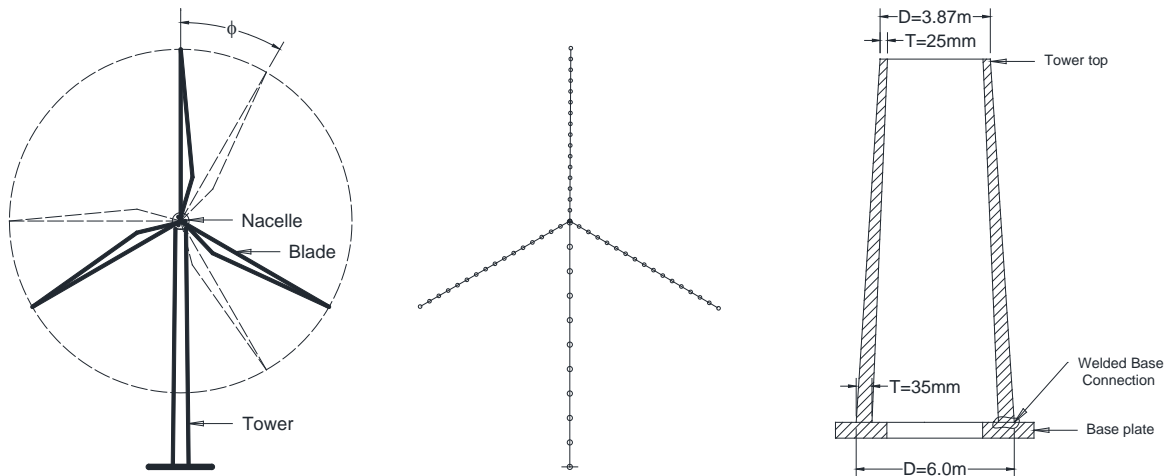


Figure 5-1. Sketch of wind tower and FEM discretization

As defined by Jonkman et al. (2009), the effective mass density of the tower is higher than normal steel mass density to account for paint, bolts, flanges and welds which are not accounted for in the tower thickness. The values of tower thickness shown in this table and the remainder of the paper are the original design thickness. In the analyses, linear tapering of the tower section from bottom to top is also assumed. A comparison between the modal frequencies obtained using the developed FEM used and what is listed in Jonkman et al. (2009) is shown in Table 5-3.

The results are in good agreement with the previously published values and provide the validation of the FEM for use in the present study. In addition, the 1<sup>st</sup> torsional frequency of the tower added to Table 5-3 is about 22.6 times the 1<sup>st</sup> translational vibration (7.00Hz compared to 0.31Hz), which means that torsional vibration can be considered a higher mode. Therefore, it is reasonable to assume no torsional effects for this study of the wind tower.

Table 5-3. Comparison of the FEM model: Natural frequencies comparison

Description of Modes	Natural Frequencies (Hz)	
	FEM model	ADAMS (Jonkman et al. 2009)
Tower 1 <sup>st</sup> Fore-Aft	0.31	0.32
Tower 1 <sup>st</sup> Side-to-Side	0.31	0.32
Tower 2 <sup>nd</sup> Fore-Aft	2.70	2.86
Tower 2 <sup>nd</sup> Side-to-Side	2.70	2.94
Tower 1 <sup>st</sup> Torsion	7.00	Not given
Blades 1 <sup>st</sup> Flap-wise	0.61	0.63
Blades 1 <sup>st</sup> Edge-wise	1.01	1.09
Blades 2 <sup>nd</sup> Flap-wise	1.77	1.65

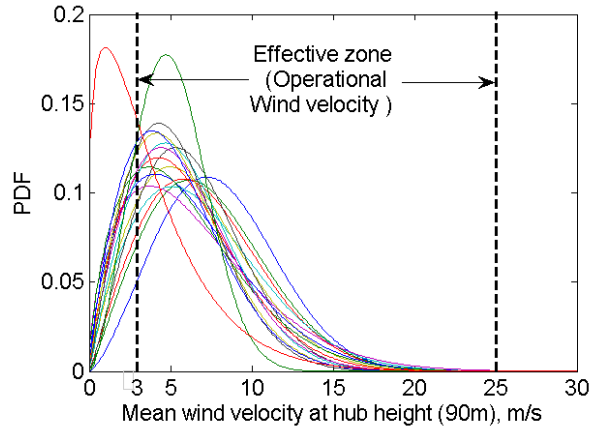
### 5.1.2. Colorado wind distribution

Wind distribution characterization for Colorado sites was investigated by Atadero et al. (2008). Based on this report, a Weibull distribution was adopted to describe the annual wind distributions at a height of 10m for 17 sites spatially distributed throughout Colorado. The scale and shape parameters of the Weibull distribution are taken from Atadero et al. (2008), which were then used for recovering the annual mean wind velocities for these sites at 10m and rank ordered for annual mean wind velocity from highest to lowest value (see Table 5-4). Since the operation of wind turbines is dependent on the wind velocity at the hub height, the Logarithmic law (Manwell et al. 2009) is deemed to be acceptable for estimating the wind velocity at 90m (hub height) with the assumption of “cross terrain” for all the fields in Colorado (surface

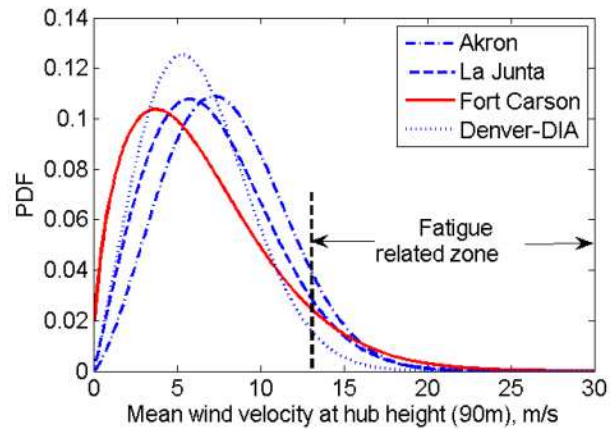
roughness length,  $z_0$ , is  $0.05m$ ). The cut-in and cut-out wind velocities for wind turbine are based on the power curve for each wind turbine system (Manwell et al. 2009). The cut-in velocity is the minimum wind velocity at which useful power can be delivered and the cut-out velocity is the maximum wind velocity which is usually limited by engineering design to prevent the system from instability. For the typical 5-MW wind turbine (Jonkman et al. 2009), the cut-in and cut-out wind velocities are  $3m/s$  and  $25m/s$ , respectively at a hub height of  $90m$ . The probability of the mean wind velocity being between  $3m/s$  and  $25m/s$  is defined as the effective time or the percentage of time when the wind turbine is in operation (Table 5-4). Based on the wind power classification scale (Manwell et al. 2009) which is based on the annual mean wind velocity at  $10m$ , only 8 sites in Table 5-4 (the top eight listed sites) are suitable for wind power development (class 2 or higher) and are investigated in this study. As highlighted in Table 5-4, the wind potential sites are all located in the East side of Colorado. It is interesting to realize that Akron (wind power class 4), which is proper for most wind turbines, and Limon (wind power class 3) experience 93% and 90% effective time, respectively. However, these Figures for wind power class 2 range from 77% to 87% of operational time in a year. The Weibull distributions for the 17 wind sites are presented in Figure 5-2.

Table 5-4. Weibull parameters and wind power classification for Colorado sites

No.	Location	Scale Para. (m/s)	Shape Para.	Mean at 10m (m/s)	Mean at 90m (m/s)	Mean at 90m < 3m/s (%)	Mean at 90m >25m/s (%)	Effect time (%)	Wind power class
1	Akron/Washington County Airport	6.38	2.414	5.66	8.00	6.76	0.001	93.24	4
2	Limon	5.87	2.111	5.20	7.35	11.00	0.004	88.99	3
3	La Junta Municipal Airport	5.69	2.035	5.04	7.13	12.56	0.004	87.44	2
4	Air Force Academy	5.55	1.832	4.93	6.98	15.77	0.024	84.21	2
5	Fort Carson/ Butts	5.13	1.551	4.61	6.53	22.44	0.110	77.45	2
6	Colorado Springs	5.16	1.921	4.58	6.48	16.57	0.002	83.43	2
7	Denver International Airport – (DIA)	5.06	2.136	4.48	6.34	14.45	0.000	85.55	2
8	Pueblo Memorial Airport	4.96	1.671	4.43	6.27	21.47	0.023	78.50	2
9	Alamosa Municipal Airport	4.72	1.617	4.23	5.98	23.98	0.021	75.99	1
10	Buckley ANGB	4.74	1.791	4.22	5.96	21.08	0.003	78.91	1
11	Denver - Stapleton	4.71	1.981	4.17	5.91	18.60	0.000	81.40	1
12	Hayden/Yampa	4.66	1.883	4.14	5.85	20.31	0.000	79.69	1
13	Eagle County Regional Airport	4.38	1.885	3.89	5.50	22.49	0.000	77.51	1
14	Grand Junction	4.33	1.975	3.84	5.43	21.66	0.000	78.34	1
15	Fort Collins	4.24	1.814	3.77	5.33	24.76	0.000	75.24	1
16	Aspen - Sardy Field	4.07	2.534	3.61	5.11	17.44	0.000	82.56	1
17	Craig	2.92	1.214	2.74	3.87	49.25	0.014	50.74	1



a) Distribution for 17 sites



b) Distribution for some typical sites

Figure 5-2. Weibull distribution for annual mean wind velocity at 90m for Colorado sites

Based on the International Electrotechnical Commission (IEC 2005) code, which is the primary standard for wind turbines (Manwell et al. 2009), IEC 61400-1(2005) divides the mean turbulence intensity at wind velocity of 15m/s into three classes. Class A stands for high turbulence intensity from 14%-16%, class B is for medium turbulence intensity from 12-14%, and class C is for low turbulence intensity which is less than 12%. Since the wind turbulence intensity ( $TI$ ) information for Colorado sites is not available, a range of turbulence intensities from 12% to 16% at wind velocity of 15m/s was selected for investigation to cover all cases of turbulent classes mention in the IEC codes.

### 5.1.3. Wind turbine under Colorado wind field

#### 5.1.3.1. Dynamic response of wind turbine FEM model

Dynamic analysis was run for a 3600-second wind duration with an analysis time step of 0.1s while the wind time step was 0.5s. Figure 5-3 shows the velocity time-history response of the blade tip and tower top relative to the fluctuating wind velocity for a 12m/s mean wind speed at elevation of 80m. It is interesting to note that the velocities of the tip blades are close to the wind fluctuation while the velocity of the tower top is relatively small. Therefore, the

assumption of steady state or quasi-static behavior is clearly no longer valid for analyzing blade dynamics.

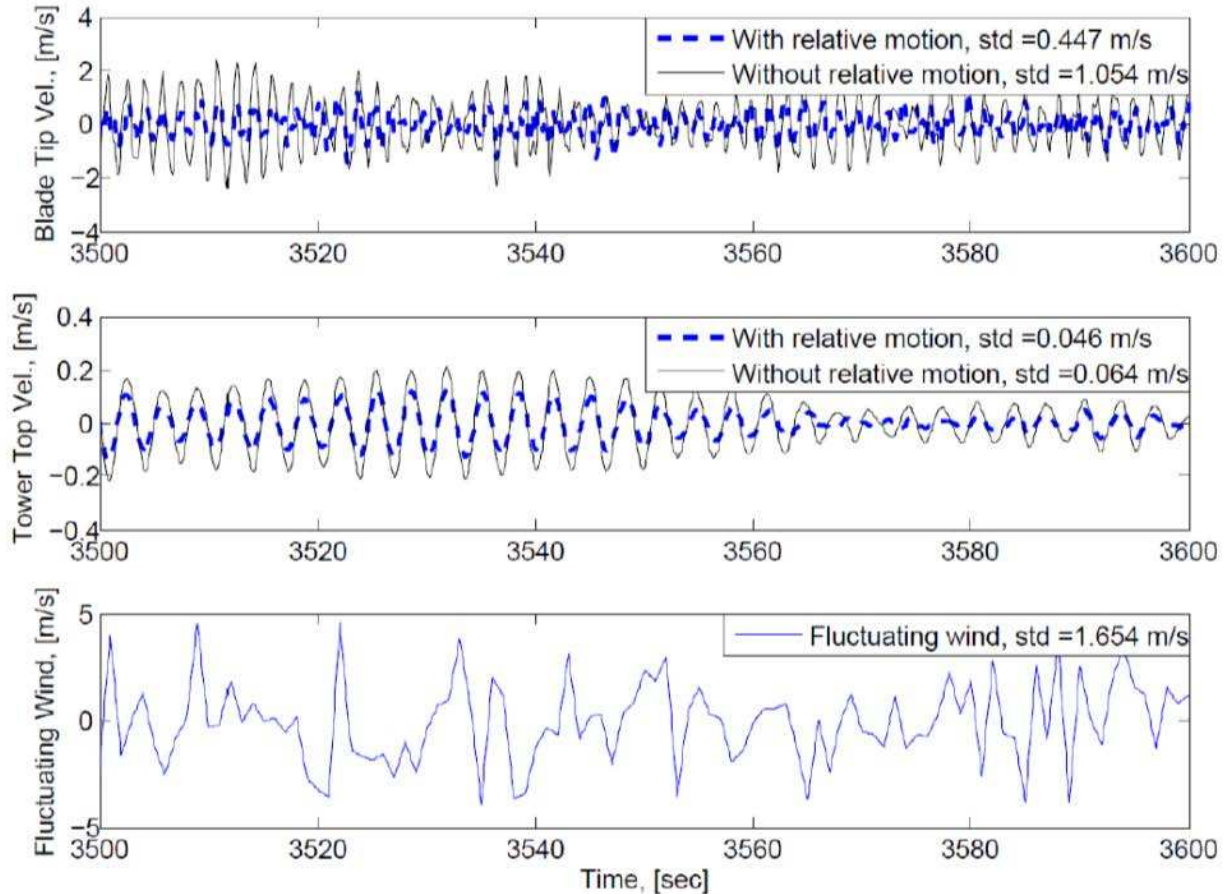


Figure 5-3. Compare velocity at tip of blade and top of tower to wind velocity for **12m/s** mean wind speed at **80m**

When relative motion between the blades and the top of the tower is calculated, the velocity as well as the acceleration at the tip of the blades experience significant reduction when compared to those without relative motion (Figure 5-4). It is clear that the root mean square (RMS) acceleration at the top of the tower is  $0.009g$ , much higher than the acceleration limit of  $0.005g$  for a commercial building (Griffis 1993). In addition, the tower top acceleration (RMS= $0.009g$ ) is very small compared to blade tip acceleration (RMS= $0.280g$ ). Therefore, the

top tower acceleration presented in Equation (2-1) can be eliminated. Figure 5-4 also shows some level of reduction of stress at the tower base when relative motion is applied.

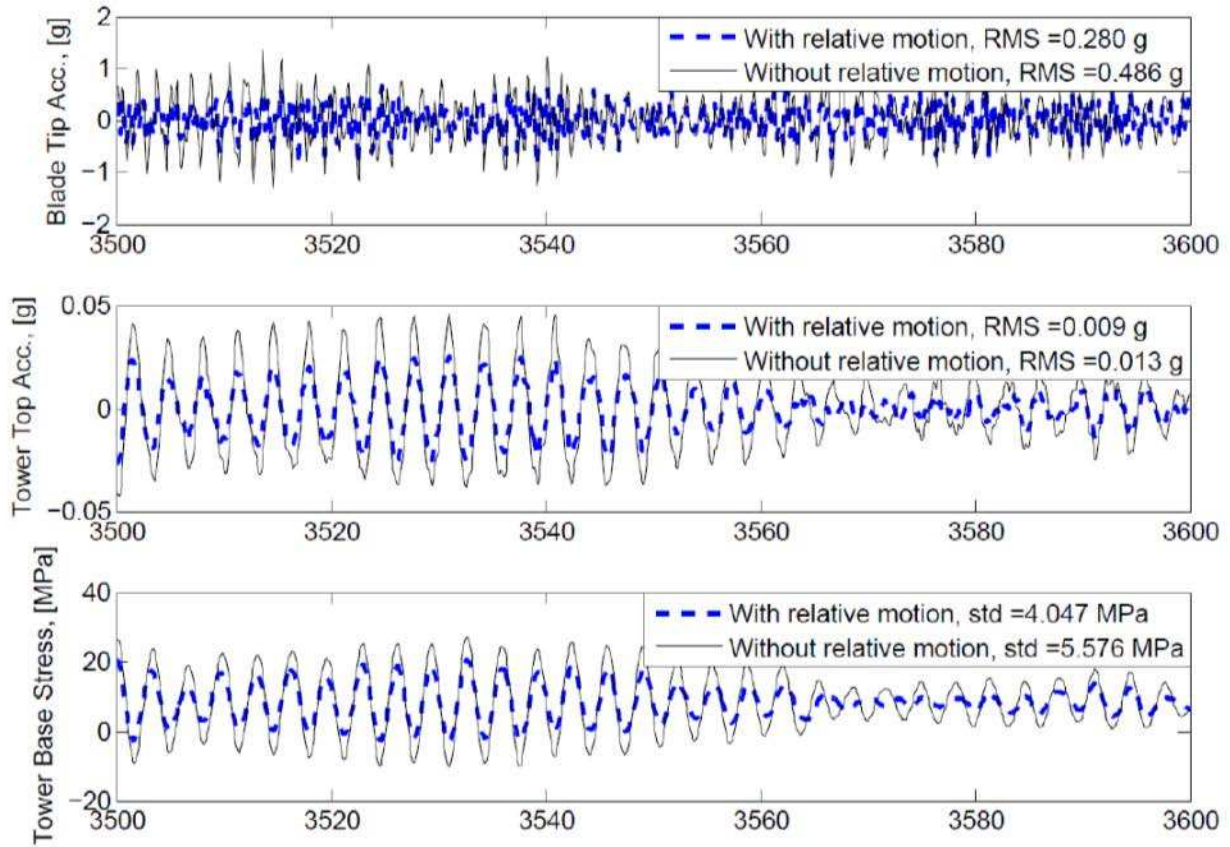


Figure 5-4. Acceleration at blade tip and tower top; Stress at tower base for 12m/s mean wind speed at 80m

The effect of relative motion can be viewed as added aerodynamic damping. In this case, aerodynamic damping of blades is much higher than that of the tower. In addition, Figure 5-3 shows the base shear at each blade and the total base shear for the last 10 seconds.



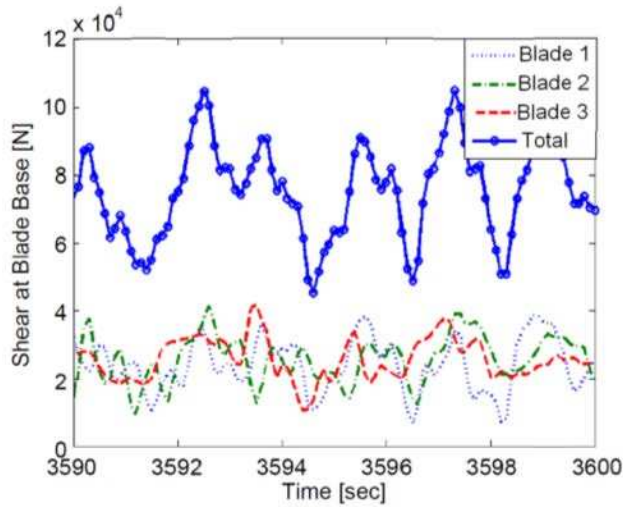
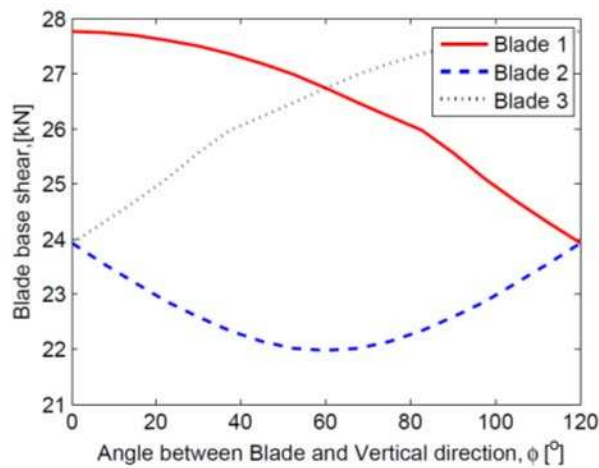
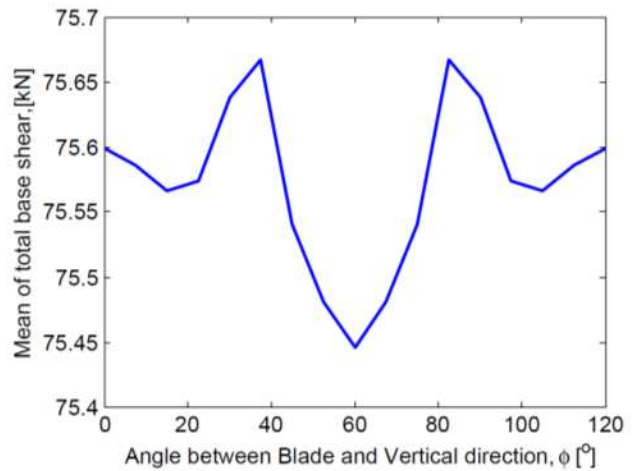


Figure 5-5. Shear at blade bases for 12m/s mean wind speed at 80m

Base shear at blade based is presented in Figure 5-6. A blade experience maximum base shear and stress range at  $\phi = 0^\circ$ . The structure system experiences the maximum base shear at  $\phi = 37.5^\circ$ .



a) Blade Base Shears



b) Total Mean Blade Base Shears

Figure 5-6. Base shear at each blade and total base shear due to blade angles

### 5.1.3.2. Fatigue life using S-N curve model (crack initiation)

Fatigue life from the S-N curve model in Chapter 3 are shown in Figure 5-7, which presents the fatigue life for the eight potential wind sites in Colorado listed in Table 5-4 for

different turbulence intensities. As shown in the figure, fatigue life varies widely with turbulence intensities and sites. At site 1 (Akron), for example, fatigue life of a typical 5-MW wind turbine is only 24 years for 16% turbulence intensity. However, for 14% and 12% turbulence intensity, fatigue life is extended by two times (55 years) and seven times (176 years), respectively. In other words, fatigue life increases rapidly with the decrease of turbulence intensity, as one might expect. It is worth noting that it is quantified here thereby enabling fully informed decision making during the wind turbine farm planning process.

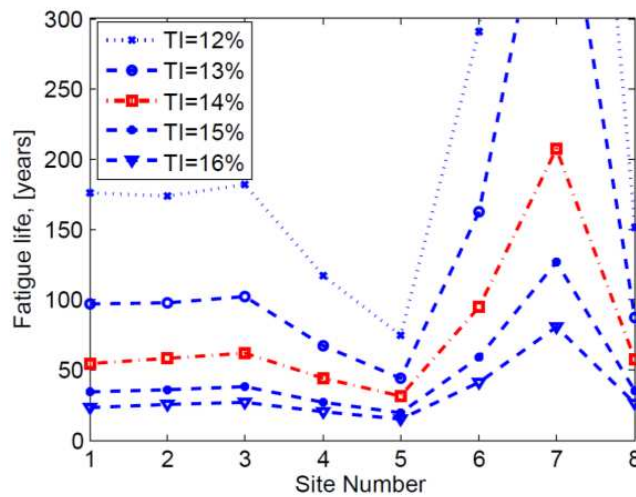
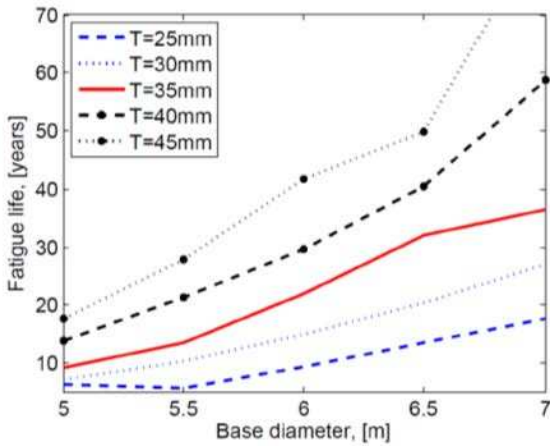


Figure 5-7. Fatigue life of a typical 5-MW wind turbine at 8 Colorado sites

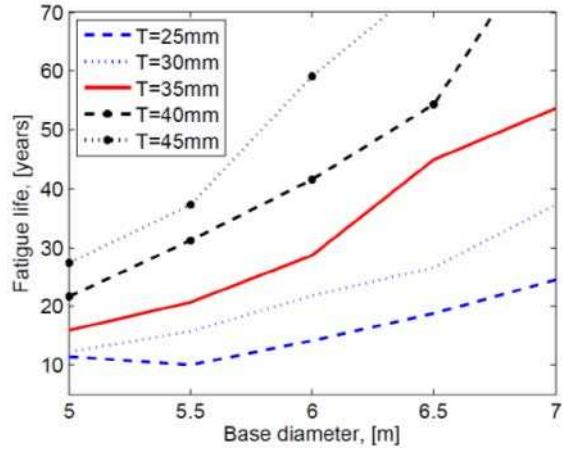
On the other hand, fatigue life also depends heavily on the annual mean wind velocity and the distribution of wind velocity at each site. In general, sites with the higher annual mean wind velocities experience the lower fatigue life, which is intuitively obvious. However, depending on the variance of wind velocity in a year (the shape parameter of Weibull distribution), fatigue life may not be proportional to the annual mean wind velocity. For instance, as shown on Figure 5-7, fatigue life at the first three sites is around 50 years when turbulence intensity is 14% and increases gradually with the decrease of annual mean wind velocity. At site 4 (Air Force Academy) and site 5 (Fort Carson), however, fatigue life drops to only 44 and 31

years although these two sites experience the lower annual mean wind velocities than the first three sites. The same trend is also identified for site 8 (Pueblo Memorial Airport) where the annual velocity is smaller than all the other seven sites even when it experiences a relatively low fatigue life (about 50 years). On the other hand, for the same turbulence intensity (14%), fatigue life at site 7 (Denver -DIA) increased significantly to 207 years (more than six times the fatigue life at site 5) even though the annual mean wind velocities at site 7 and 5 are not much different (see Table 5-4). This is because of the differences in wind distribution for each site. A smaller shape parameter results in a longer tail of the Weibull distribution (Figure 5-2b). As mentioned previously, only wind velocities large enough to result in an effective stress range greater than half of threshold stress will affect the service life. As shown in Figure 5-2b, Fort Carson, with the smallest shape parameter (1.551) has the highest probability of wind velocity falling in the fatigue related zone which results in the lowest fatigue life. Conversely, Denver- DIA experiences the largest shape parameter (2.316) and has the lowest probability of wind velocity in the fatigue zone; therefore, highest fatigue life is predicted. Since the tail property of wind distribution is in the fatigue related zone, shape parameter of Weibull wind distribution is very important for predicting the fatigue life of a wind turbine.

Figure 5-8 shows the fatigue life vulnerability as a function of base thickness and base diameter when the blades do not rotate (Figure 5-8a) and at normal rotating speed (Figure 5-8b). In both cases, increasing the wall thickness or base diameter improves the fatigue life in a different way.



a) Blade Rotating Speed = 0rpm

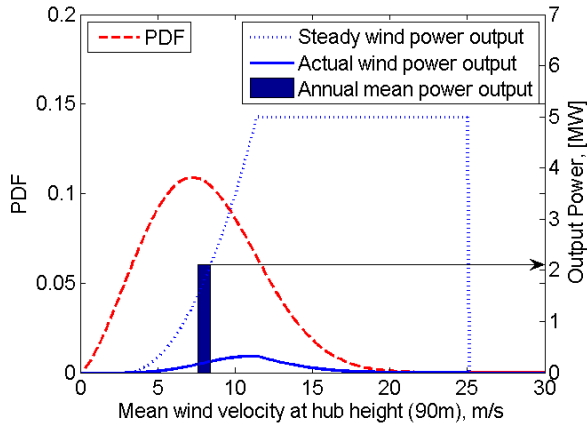


a) Blade Rotating Speed = 12.1rpm

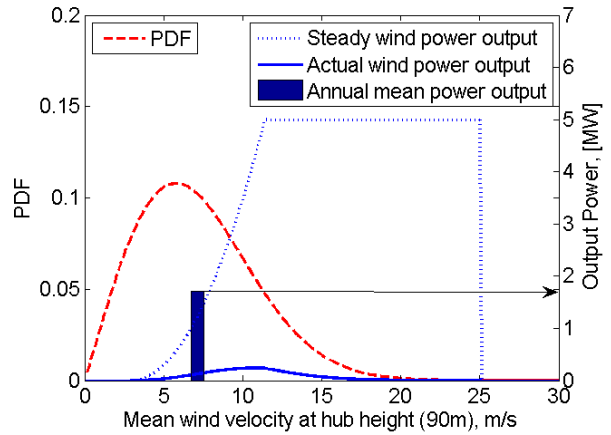
Figure 5-8. Fatigue life due to thicknesses and diameters at 7m/s annual mean wind speed

It is worth noting that at the parked state (blades are not rotating), fatigue lives are less than those in the case of normal rotation. The reason behind this is that under wind loading, uplift and drag forces will drive the rotation of the blades. If blades are forced to stop or not allowed to rotate, shear forces at blade bases will increase in order to hold the blades in place and therefore, bending stress at tower base will increase and the fatigue life will decrease. However, detailed investigation of this comparison is felt to be beyond the scope of the current study and will be investigated in a forthcoming study.

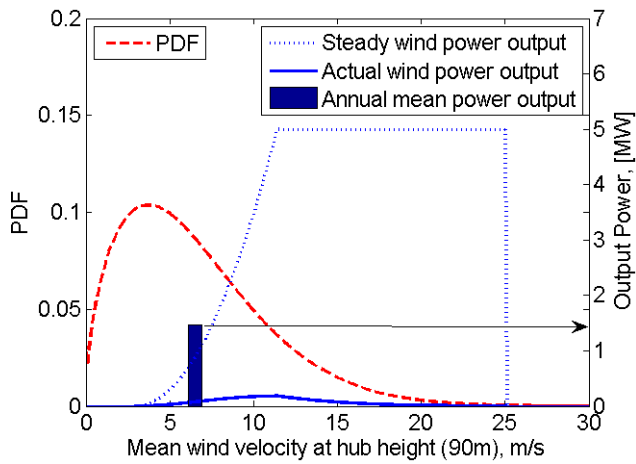
In addition, the relationship between wind distribution and output power is presented in Figure 5-9. This figure shows that although the designed capacity of the wind turbine is 5 MW, the annual mean power harvested may be closer to 2 MW (40% of the designed capacity) at Akron and La Junta (wind power class 4 and 3, respectively). The value for Fort Carson and Denver- DIA is just around 1.5 MW (30% of the designed capacity). This is because the wind distribution is not contained within the bounds of the power curve of the wind turbine. However, these numbers are also in the range of the average capacity factor for US wind turbine from 20% to 50% (Wiser and Bolinger 2013), and are therefore considered acceptable.



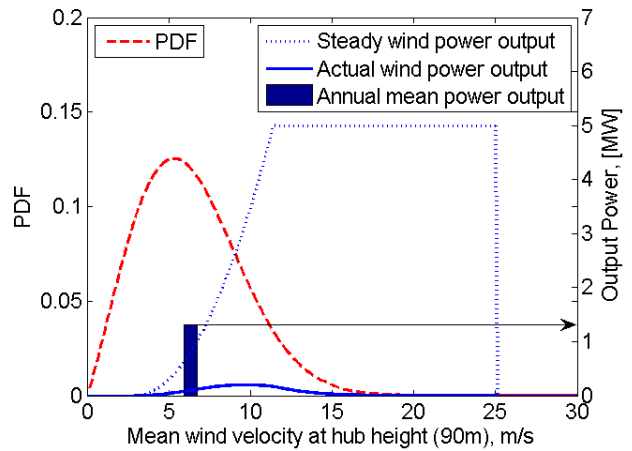
(a) Akron (Site 1)



(b) La Junta (Site 3)



(c) Fort Carson (Site 5)



(d) Denver – DIA (Site 7)

Figure 5-9 .Wind velocity probability density and output power at four typical sites

Figure 5-10 compares the fatigue life and the annual mean output power for the eight sites for an average turbulence intensity of 14%. In general, the annual mean output power is proportional to the annual mean wind velocity at each site. Although there is a significant different in fatigue life between site 5 (Fort Carson) and site 7 (Denver – DIA), the annual output power of these two sites is almost the same (almost 1.5 MW). This means that a wind power project at Denver – DIA (site 7) is far more economical than that at Fort Carson (site 5). These

figures can be used for evaluating a wind power project by comparing the amount of energy harvested during the entire service life and the associated cost for tower material.

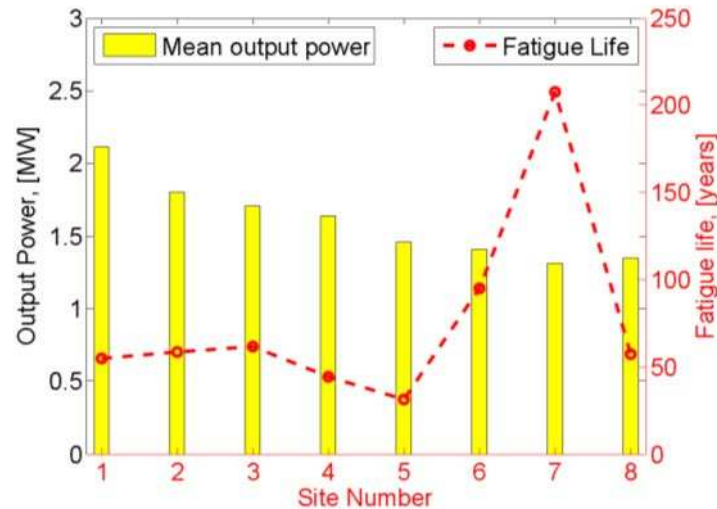


Figure 5-10. Annual mean output power and Fatigue life at 8 sites when TI=14%

### 5.1.3.3. Fatigue life using Paris's Law Model (crack propagation)

As mentioned, in reality, at the end of service life, the through-thickness cracks will continue to propagate until the tower collapses. By applying the Paris Law, the growth rate of crack for this connection can be determined as shown in Figure 5-11. There are three regions that define the fatigue growth rate of a crack. Region I is characterized by very small crack propagation behavior where the crack spends most of its life ( $\Delta K_{eff} < \Delta K_{th}$ ). Region II defines the stable crack propagation stage, which can be represented by the Paris Law. The stable growth is characterized by a propagation rate that varies linearly with the stress intensity range on a log-log scale until the maximum stress intensity factor reaches the fracture toughness of material ( $K_{max} < K_{IC}$ ) at which the growth rate is rapid and plastic collapse may occurs (region III). On the other hand, the crack size at onset of fracture is called the critical crack size (Figure 5-12), which depends on the annual mean wind speed.

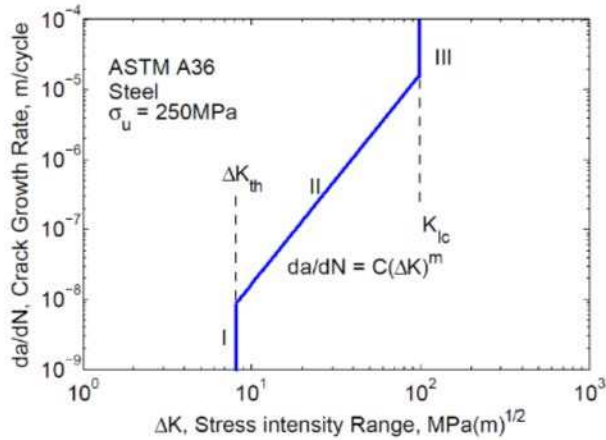


Figure 5-11. Crack growth rate

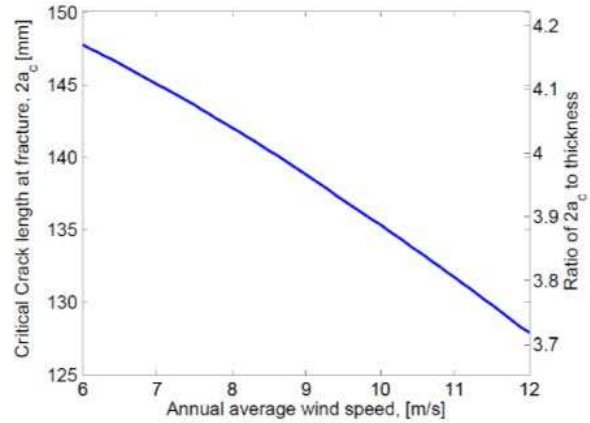


Figure 5-12. Maximum crack length

If the damage states are defined based on the ratio of crack size at failure ( $a_f$ ) to the wall thickness ( $T$ ), the extended life (time for an initial crack develop to crack size at failure) based on Equation (3-12) is shown in Figure 5-13. At an annual wind speed of  $8.5\text{m/s}$ , this tower can sustain up to four years from the initial crack development to the length of  $3T$  and nine years to the critical value. However, if the annual wind speed is  $12\text{m/s}$ , which is quite high, the extended life is just one year for the initial crack development to critical crack length.

In addition, Figure 5-14 shows a level 1A fatigue crack assessment based on BS7910 using the methodology presented herein. It can be seen from the Figure 5-14 that when the annual mean wind speed increases from  $6\text{m/s}$  to  $12\text{m/s}$ , all cases are well under the acceptable region, which means that plastic collapse (load ratio less than 0.8) or fracture (stress intensity less than 0.707) will not occur based on the BS7910 level 1A.

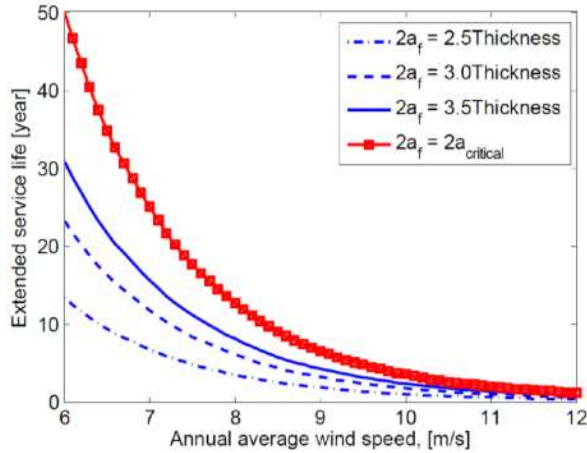


Figure 5-13. Extended service life after first through-thickness crack

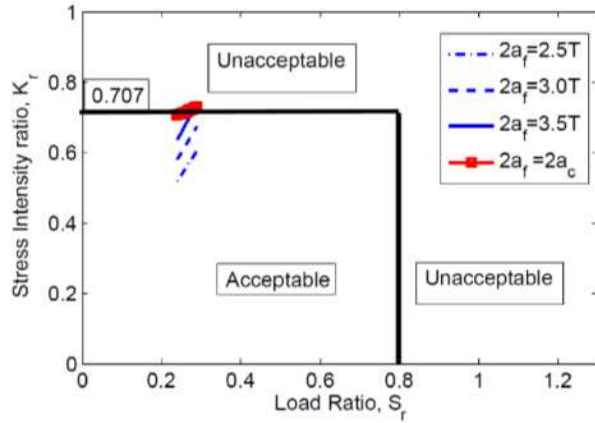


Figure 5-14. Level 1A FAD (BS7910:2005)

Since the fracture is critical as it defines the end of fatigue life, the ratio of the stress intensity factor to the critical stress intensity is allowed to reach 0.707. Using this information, the critical crack length is calculated ( $2a_f = 2a_c$ ). In case 1, when the limit on the crack length is  $2a_f = 2.5T$ , the load ratio increases from 0.24 to 0.29 and the stress intensity ratio increases from 0.52 to 0.60 when annual mean wind speed increase from 6 to 12m/s. In case 2, when the limit of crack length  $2a_f = 3.0T$ , the load ratio increases from 0.52 to 0.60 and the stress intensity ratio increases from 0.57 to 0.67 when annual mean wind speed increase from 6 to 12m/s. For this low stress level, stress intensity ratio limit can be increased up to 1 (based on level 2 FAD-BS7910) and hence, the critical crack length can be longer.

## 5.2. Performance-Based Design Example Using Fragilities

Performance-Based Design (PBD) using fragility curves is a new design, evaluation and construction methodology for engineering facilities subjected to uncertainty design parameters. This design approach was first developed for fire system safety and then for earthquake engineering (e.g. Rosowsky and Ellingwood 2002). For the fatigue life design carried out in this



study for wind turbines, only the uncertainty of the fatigue constant of the steel tower base connection provides the variability when constructing the fragility curves. This example considers two design variables: the outside diameter of the tower base ( $D$ ) and the tower wall thickness at the base ( $T$ ). The top diameter and thickness of the tower remain unchanged to keep the same connection to the nacelle on top of the tower. The thickness and diameter are assumed to be linearly tapered from the base to the top of the tower and only the tapering ratio is changed. These parameters will vary around the original values ( $T = 35mm$  and  $D = 6.0m$ ).

A fragility,  $F_r$ , can be expressed as

$$F_r = P[D > C|I] \quad (5-1)$$

where  $D$  is the demand,  $C$  is capacity, and  $I$  is the hazard intensity. In most cases, a fragility can be expressed (Rosowsky and Ellingwood 2002) using the assumption of lognormal peak responses for the structure of interest as,

$$F_R(I) = \Phi\left(\frac{\ln(I) - m_R}{\xi_R}\right) \quad (5-2)$$

in which  $\Phi()$  is cumulative distribution function (CDF) of the standard normal distribution,  $m_R, \xi_R$  are logarithmic mean and logarithmic standard deviation, respectively.

Figure 5-15 presents the fatigue life fragility for the tower-to-base plate welded connection when blades are rotating at the designed operation speed (12.1rpm). Figure 5-15 also shows that for this 5-MW wind turbine configuration, the fatigue life of the tower base connection can withstand 40 years, 30 years, and 20 years at annual mean wind speed of 7.5m/s, 7.9m/s, and 8.5m/s, respectively, with the same probability of failure of  $10^{-2}$ . If the tower is built at a site with 9m/s annual mean wind speed, there will be almost no chance of failure in the first 10 years. However, in the 20<sup>th</sup>, 30<sup>th</sup> and 40<sup>th</sup> year, the probability of failure would be 14%, 68% and 95%,

respectively. It is important to note that the results presented in Figure 5-15 only account for service fatigue life where a through-thickness crack becomes visible.

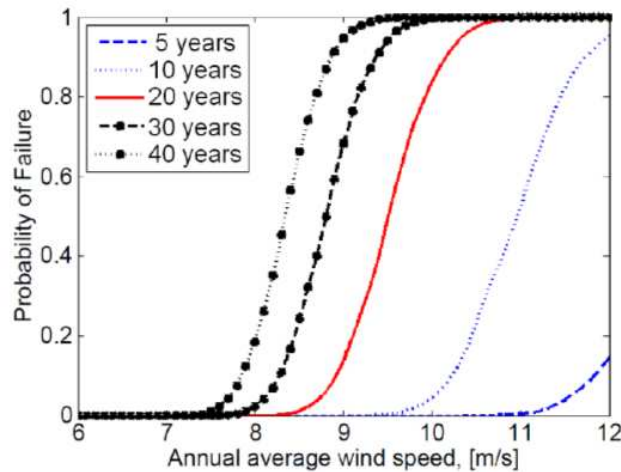
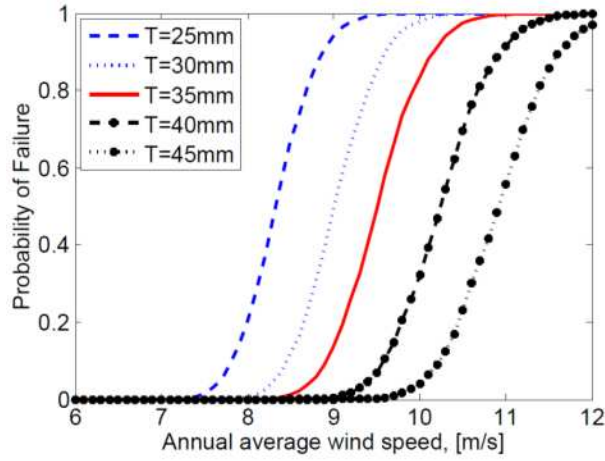
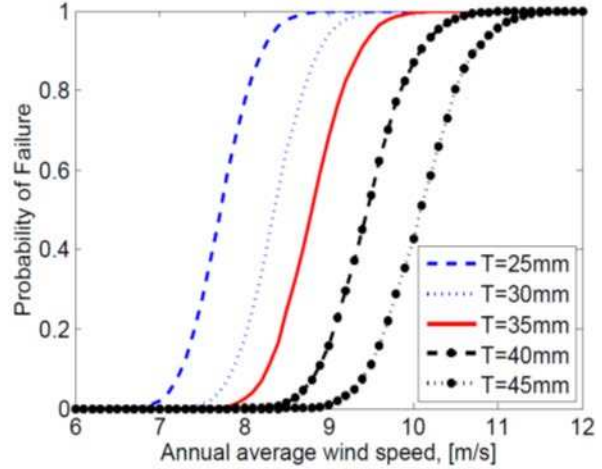


Figure 5-15. Fatigue life fragility for base Diameter =6.0m, Thickness =35mm

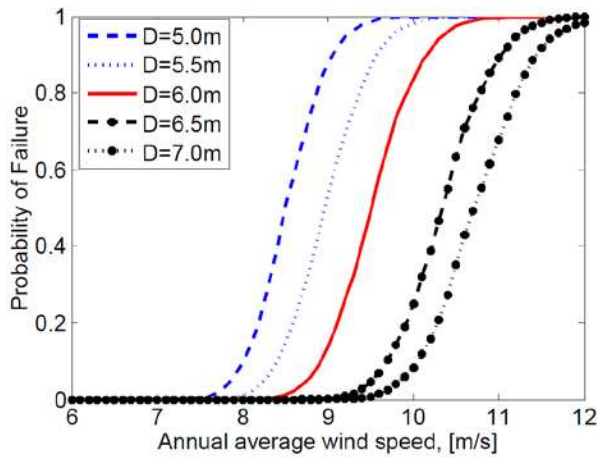
Fragility curves are developed for different design variables and are shown in Figure 5-16. The first two graphs present fragility curves showing the changes in the tower wall thickness at the base for a 20-year-PBD (Figure 5-16a) and 30-year-PBD (Figure 5-16b). A design example can be inferred from these charts that by increasing the tower thickness from original value of 35mm to 40mm in site with an annual wind speed of the 8.5m/s, the total fatigue life of the base tower connection can increase from 20 years to 30 years with the same probability of failure of  $10^{-2}$ . The same trends are for changing the tower outside diameters instead of the thicknesses can be observed in Figure 5-16c and Figure 5-16d. However, increasing the tower diameter will result in larger wind loading on the tower and therefore, the fatigue life will be affected. Based on Figure 5-16, designers can select which parameters to adjust to obtain the desired fatigue life (with some probability of exceedance) in the most economical way.



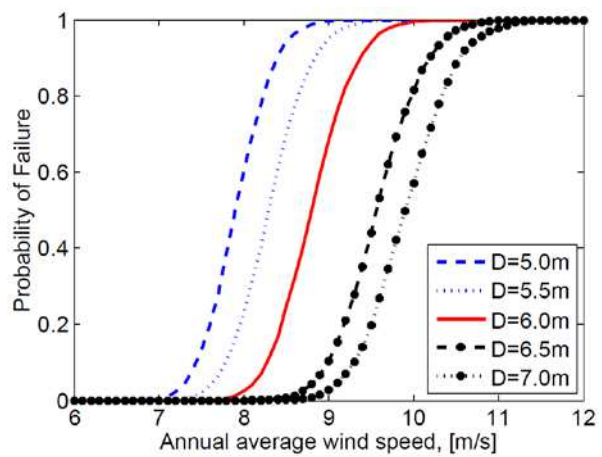
a) 20 years,  $D=6.0m$ ,  $BRS=12.1$  rpm



b) 30 years,  $D=6.0m$ ,  $BRS=12.1$  rpm



c) 20 years,  $T=35mm$ ,  $BRS=12.1$  rpm

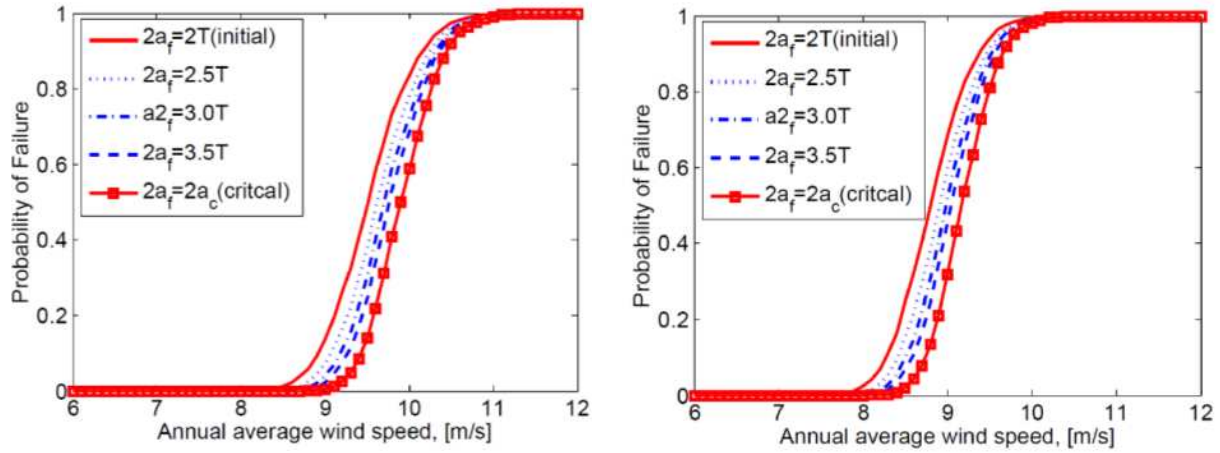


d) 30 years,  $T=35mm$ ,  $BRS=12.1$  rpm

Figure 5-16. Fatigue life Fragility for Performance-Based Design varying with different base outside diameters (**D**) and base thicknesses (**T**)

In terms of crack propagation, if the crack is allowed to propagate to different crack lengths before reaching the critical values, the extended life will be added to the initial service life. The resulting fragilities are shown in Figure 5-17, which shows that if crack propagation is allowed, a connection with service life of 20 years (no crack propagation) can be extended to 30 years with the same probability of failure. In other words, with the same target failure probability for a performance-based design, the tower may be able to tolerate higher annual

mean wind speeds. On the other hand, by controlling the crack lengths, the remaining service life of the wind tower can be predicted.



a) 20 years,  $T=35\text{mm}$ ,  $BRS=12.1\text{ rpm}$

b) 30 years,  $T=35\text{mm}$ ,  $BRS=12.1\text{ rpm}$

Figure 5-17. Combination Fatigue Life Fragility for crack propagating to different crack lengths

## Chapter 6 . WAVE-STRUCTURE INTERACTION MODEL VALIDATION USING EXISTING DATA

### 6.1. Tsunami loads on wood-frame wall at full scale test

Numerous experiments have been conducted in the 2-D wave flume at Oregon State University. One such test that was used for shear force validation of the ABAQUS model is the full scale light-frame wood wall test under tsunami loads tested by Linton et al. (Linton et al. 2013). The unprocessed data was compared to those from the undamaged test of 2x6 stud wall with stud spacing of 40.6cm subjected to offshore wave height of 0.30m. The tsunami loading was modeled as a single wave running up to the dry and flat shore line and hitting the transverse wall. Figure 6-1 presents a solid model of the numerical simulation of the wave flume with a light-frame wood wall.

Only three locations were used for validating the numerical model (Figure 6-1). The offshore wave height at location 1 was measured by wire resistance wave gauge while onshore wave at location 2 was measured with an ultrasonic wave gauge. Wave particle velocity was measured by acoustic-doppler velocimeter at 0.09m above the reef at location 2. The wall was equipped with 4 load cells at each corner to collect the horizontal forces on the wall. Finally, a linear variable differential transformer was used at middle of the bottom of the wall (location 3) to measure the wall displacement.

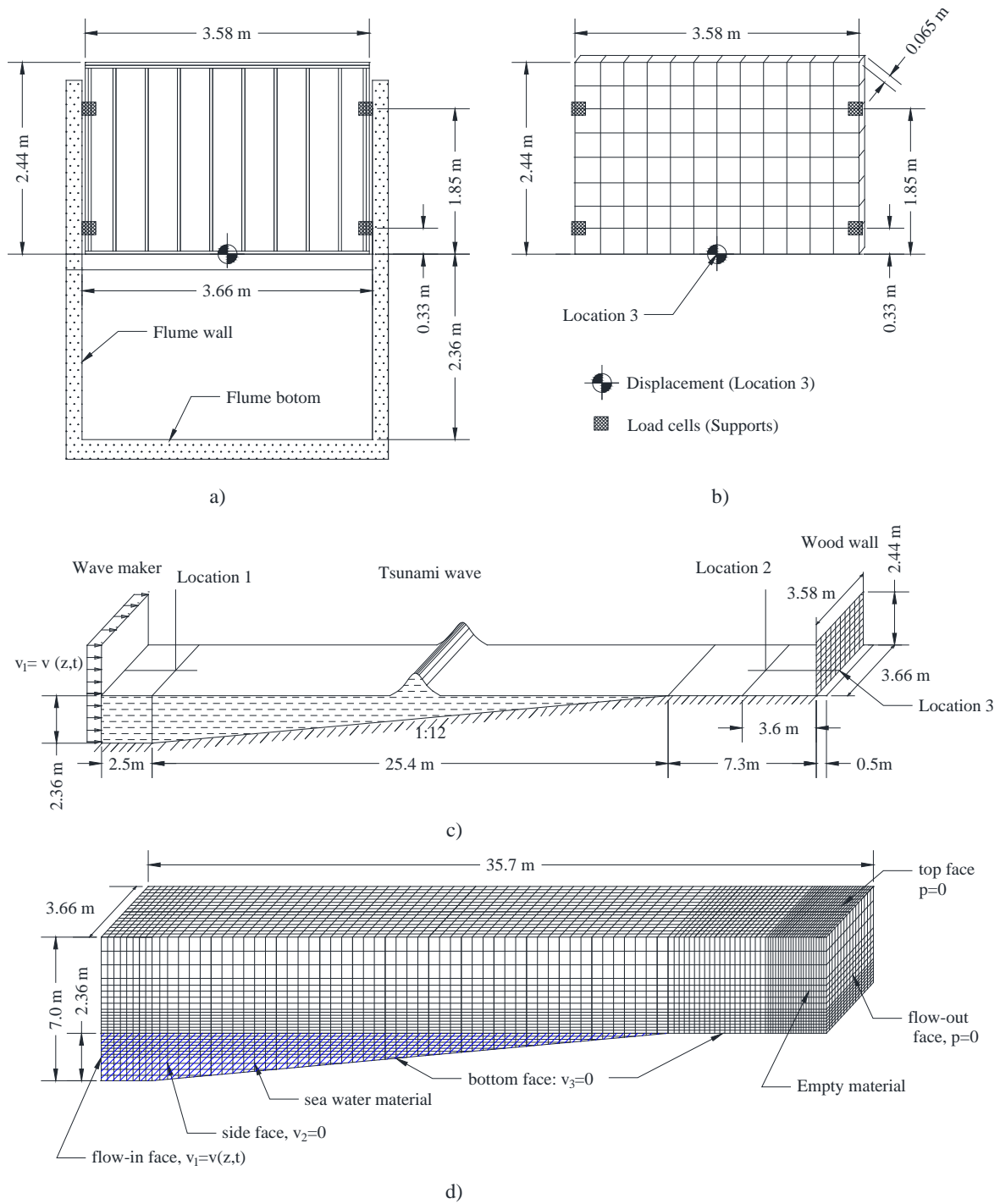


Figure 6-1. Tsunami on wall modeling configuration and meshes

a) Existing full scale wall test; b) Modeled wall and mesh and boundaries

c) Model configuration; d) Modeled flume mesh and boundaries

The numerical simulations were simplified slightly for computational efficiency with the idea that a large number of simulations would be needed to develop fragilities eventually. The transverse light-frame wood wall, as shown in Figure 1a, has dimension of  $2.24 \times 3.58 \text{m}$  and consisted of 2x6 studs sheathed with 13 mm plywood. This wall was modeled as a flat wood wall with an equivalent thickness of  $65 \text{mm}$  to have the same stiffness as the wall with 2x6 studs and plywood sheathing. The wall was modeled with shell elements with regular dimensions of approximately  $0.3 \text{m}$ . Load cells were modeled as fix supports at the four corners as shown in Figure 6-1b.

In addition, the model of the flume in ABAQUS was shortened from  $104 \text{m}$  to  $35.2 \text{m}$ , as shown in Figure 6-1c, to reduce computational time. The flat section of the flume bathymetry in front of the wave maker was reduced from  $29 \text{m}$  to  $2.5 \text{m}$ . The section after the wall, which is used to dissipate the wave, was reduced to only  $0.5 \text{m}$ , since numerically this could be done instantly. The flume consists of two parts: sea water material and empty material. Sea water material has been defined in section 2. The empty material part consisted of an empty mesh grid block. As the moving wave and hit the wall, water material will occupy the empty blocks. Wave height at a specific location is determined by the percentage of occupation and the height of each block in a vertical column of flume. Velocity and pressure can be collected at any grid node as the direct output variables from the model. As the water surface fluctuates mainly in the still water level and when water hits the wall, regular meshes at these locations are at higher resolution compared to other locations as shown in Figure 6-1d for saving computational cost. Boundary conditions were defined as shown in Figure 6-1d. The flume bottom was modeled as zero velocity, which does not allow water to slide at the flume bottom. However, at side faces, only the velocity component which is perpendicular to the flume side wall was set to zero. This

will allow the water to slide freely at the side walls to keep the 2D representation of the flume. At the flow-out face (flume end), pressure is set to be zero, which means water can run out freely. While a piston-type wave maker was used in the experiment, this was replaced by the velocity profile of the in-flow face in the numerical simulation. The frequency and amplitude of the input velocity was selected to generate same wave elevation that result in the experiment. Finally, general contact between the water and modeled transverse wall will allow water to move along with the wall in the horizontal direction, but move freely up in the vertical direction and drop due to gravity.

Initially, wave elevation time series were compared between the measured (tested) and the numerical model values at the toe of the slope (Location 1) which most accurately represents the offshore wave height and at 3.6 m seaward of the wall (Location 2) for the onshore wave height. The results are presented in Figure 6-2. From inspection of this figure, one can see that the model was able to reproduce the same wave as was tested in windows 2a and 2b. Other aspects such as wave velocity, wave flux and transient wave loading on the wall are also computed and presented in Figure 6-2c, 2d and 2e, respectively. All the results matched well with the test data. To our knowledge, this represents one of the first validations of the structural response of a full scale wood structure subjected to solitary (tsunami) force. The displacement is presented in Figure 6-2f, which recall was matched by using a flat wall in place of the 2x6 sheathing with plywood.



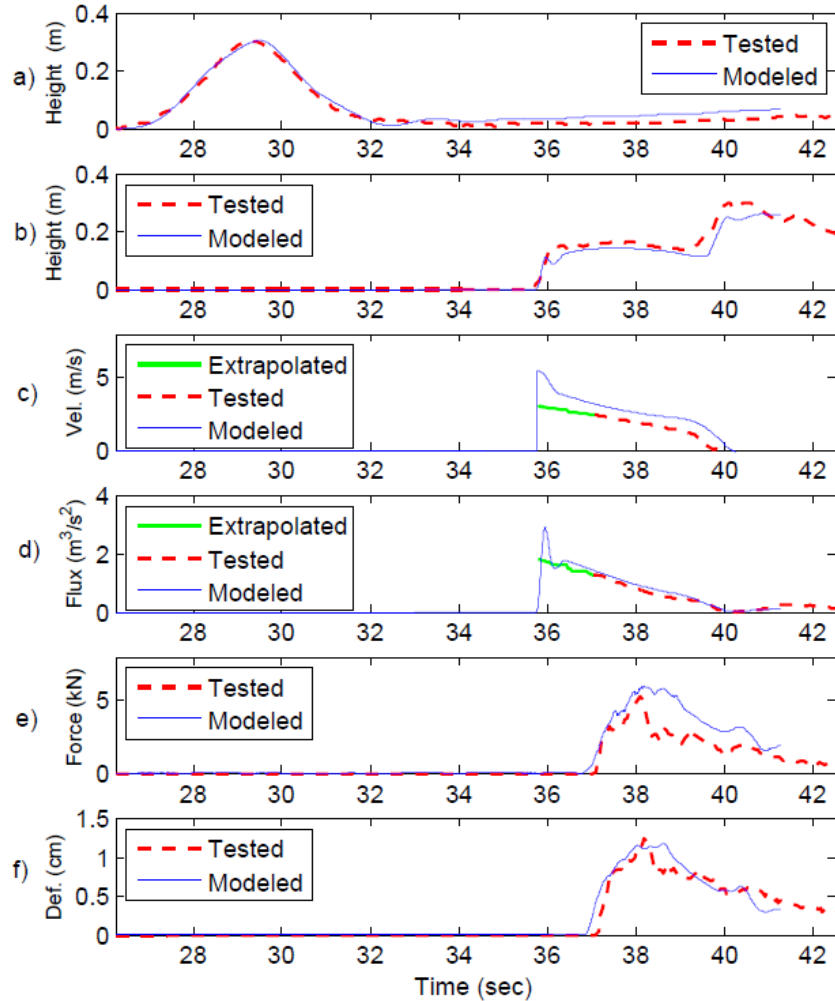


Figure 6-2. Numerical validation for Tsunami loads on transverse wall test at full scale

- a) Offshore wave height at location 1; b) Onshore wave height at location 2;
- c) Wave velocity at location 2; d) Momentum flux at location 2;
- e) Total horizontal force at 4 supports; f) Deflection at location 3

## 6.2. Uplift forces on a large scale bridge superstructure

While the first verification using the light-frame wood wall provided shear force validation for the modeling procedure, it was still necessary to validate the uplift forces. To accomplish this, the results from an experimental test of a 1:5 scale reinforced concrete bridge

super structure subjected to hurricane waves by Bradner et al. (Bradner et al. 2011) was used for comparison.

A simple layout of the test specimen can be found in Figure 6-3a & 3b. The bridge specimen has overall dimensions of  $1.94 \times 6.45m$  and height of  $0.28m$ . Vertical forces (up lift loads) were measured by four vertical load cell at four corners and two horizontal load cells at two offshore corners of the specimen. The bridge was mounted to the wave flume through reaction frame which can represent both rigid and flexible connections. For this validation, only rigid connections were considered. The load cells were modeled as two rigid supports at offshore corners and two simple supports at onshore corners. The bridge was modeled by solid elements with normal  $40psi$  concrete material properties.

The model of flume was also reduced as discussed earlier to reduce computational time. Only the horizontal section with a length of 30 m was modeled as shown in Figure 6-3c. The same modeling technique from the previous test was applied for the flume. The mesh distribution and boundary conditions were shown in Figure 6-3d.

Only one test trial was used herein. This consisted of a regular single wave that was generated from  $H = 0.5m$ ,  $T = 2s$ . The still water level was at the bottom of the bridge girders to model a level of inundation caused by surge that was observed during hurricane Katrina near New Orleans, Louisiana, USA, and was representative of the worst-case loadings. The total uplift load computed for the bridge is shown in Figure 4 compared to uplift load measured during the test. Inspection of Figure 6-4 shows an excellent match in the peak force and agreement in overall shape.

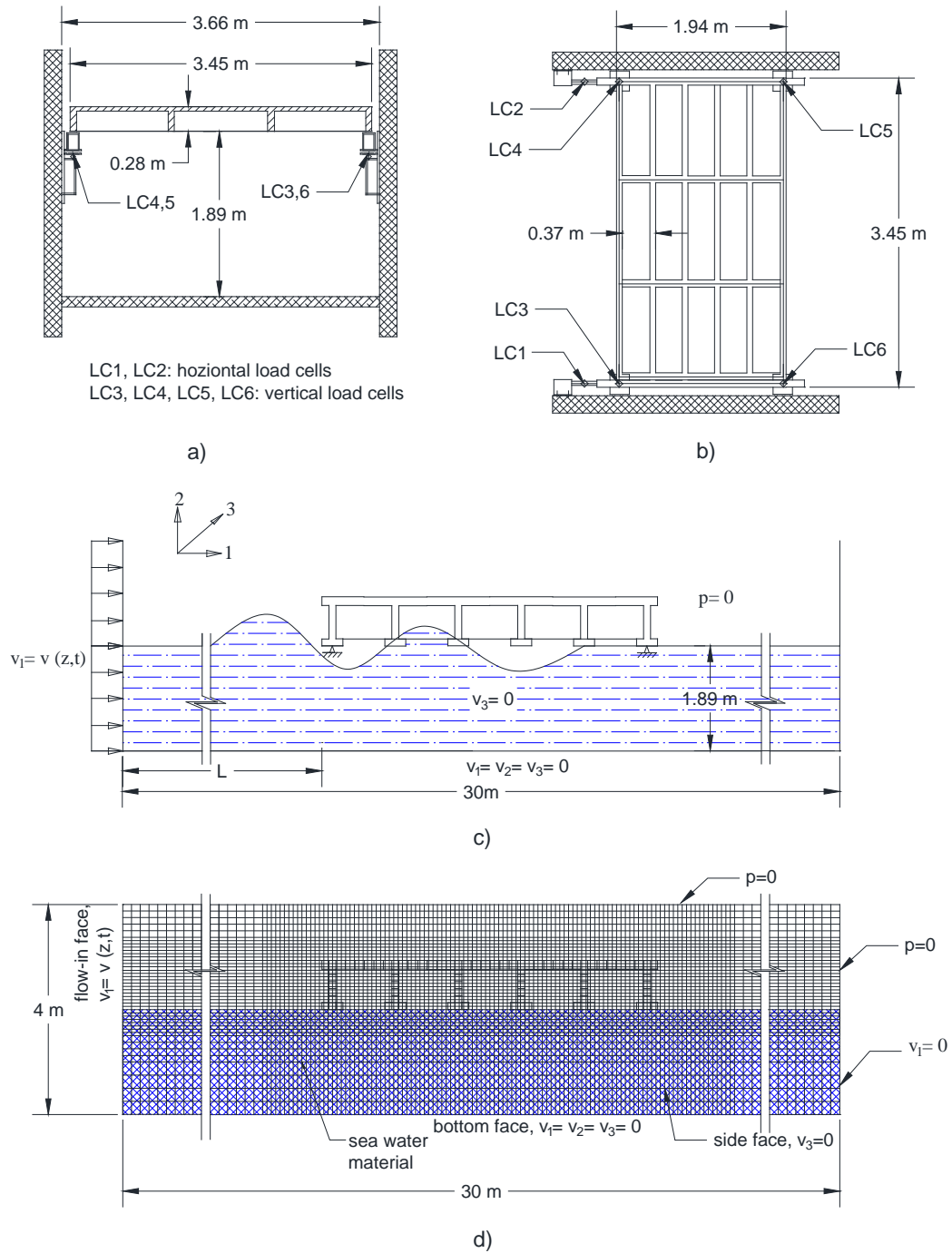


Figure 6-3. Test model set up for bridge subjected to waves

a) Flume cross view; b) Flume plan view and instruments layout

c) Numerical Model of flume model and bridge; d) Model flume mesh and boundary conditions

Based on the two examples presented herein, one for shear force and one for uplift force verification using two different specimen materials (wood, concrete), the numerical model is felt to match the test results well, and therefore the authors are confident that it can be used to develop the fragility curves as explained in a latter section.

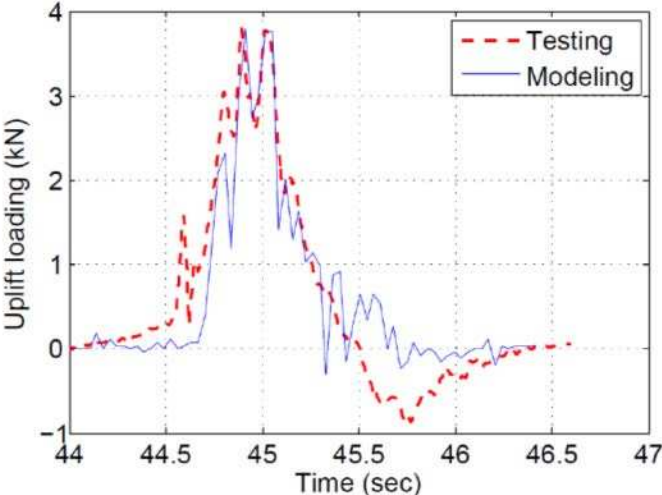


Figure 6-4. Comparison between tested and modeled uplift loading

Chapter 7 . **PERFORMANCE-BASED DESIGN OF ELEVATED COASTAL  
STRUCTURES: ILLUSTRATIVE EXAMPLES**

**7.1. Wave loading on elevated coastal structures**

*7.1.1. Wave loading on bridges using ABAQUS model*

Recall that the objective of this study was to illustrate a performance-based design methodology using fragilities for uplift capacity on elevated coastal structures subjected to wave loading. To accomplish this, a numerical wave flume, as described earlier, was utilized with a 3m height, 5m width and length of 100m. The sea floor was assumed to be flat for the illustrative examples in this study but could easily be altered for future studies. The other end of the flume was modeled as a wall with 3m height and had zero flow velocity to store the water in a resting or still condition. Water was modeled such that it had the ability to spill out of the flume end freely when the water level was above 3m by setting the zero pressure boundary condition. Flow velocity was also assumed to be zero at the bottom of the flume. Figure 7-1 shows the numerical model setup dimensions in a generic fashion for the prototype.

Prior to investigating the wave/structure interaction, generating a sea state from a given wave spectrum is required. In order to do that, only the wave flume and water were analyzed without the presence of the structure. The model of the wave flume mesh and boundary conditions can be found in Figure 7-1b but without the bridge section. Again, sea water material and empty material were used to define the flume. Initially, the sea water had dimensions of 10x5x3m. Water can freely occupy the empty material up to 6m above the initial water level. At the bottom face, all particle velocity components were set equal to zero which will not allow water to slide freely. At the side faces, the velocity component which is perpendicular to the face

was set to be zero to prevent water from running out. The out-flow face was divided into two parts. The lower part was associated with the initial water and had the same boundary conditions to that of the side face to keep the water in place. However, the higher part associated with the empty material was set to zero pressure, which means water can flow through the face when the water surface is higher than the still water level.

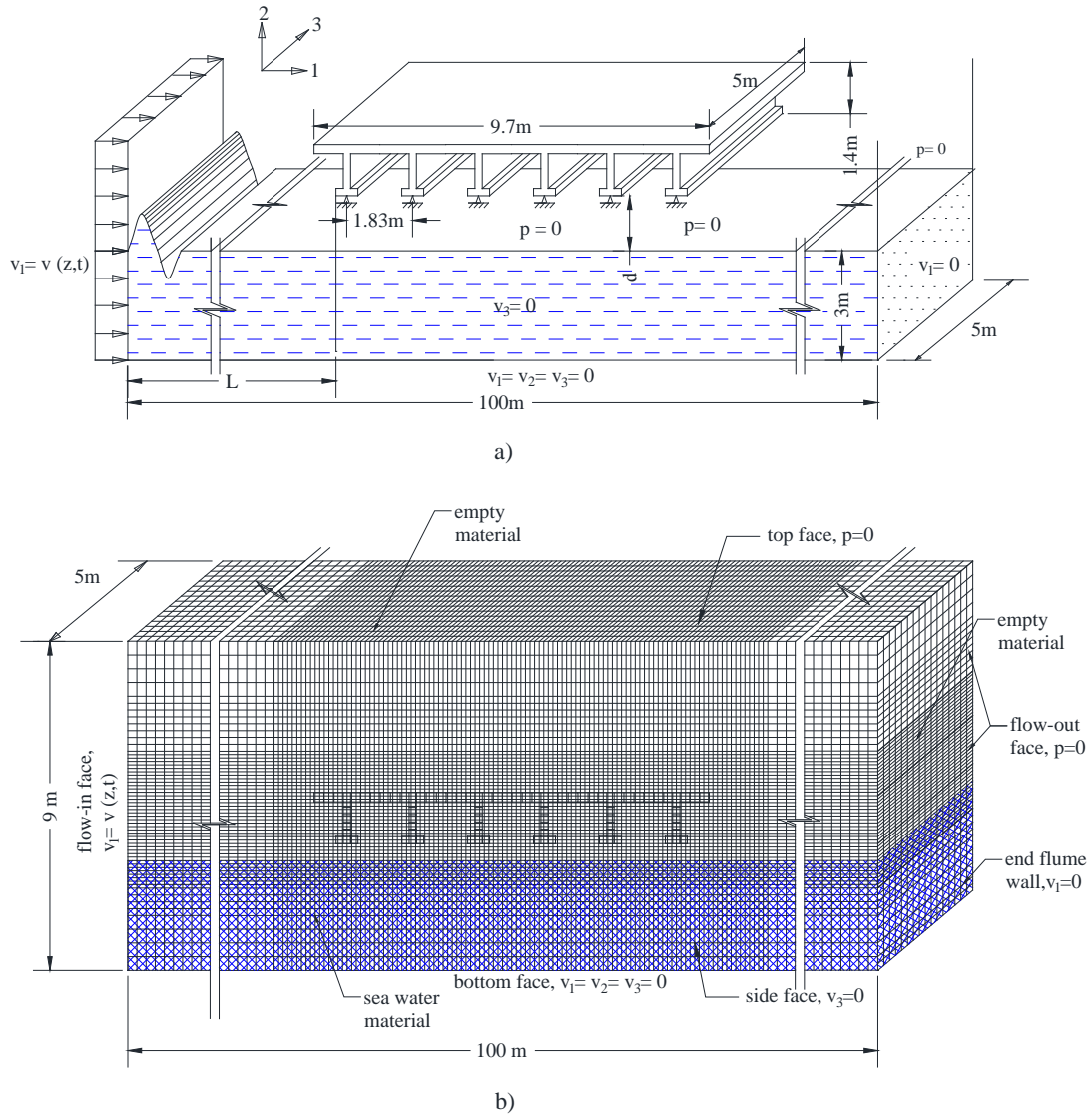


Figure 7-1. Full scale bridge section model and numerical wave flume

a) Bridge section and test set up ; b) Flume mesh and boundary conditions

This solution will reduce the effect of the reflecting wave when the wave hits the end wall of the wave flume. At the in-flow face, the input velocity profile,  $v_1 = vw(z, t)$ , was applied to generate waves. The wave spectrum was collected along the wave flume and compare to the target wave spectrum. The structure was then placed at the location where the generated wave spectrum fits the desire wave spectrum.

The structure was modeled as a section of the prototype I-10 bridge (Bradner et al. 2011) with simple supports at beam ends. The prototype bridge section is 5m long and the geometry was simplified slightly as shown the Figure 7-1a. The distance,  $L$ , from wave maker to the structure was set equal to the location in the analysis where wave spectrum matched the TMA spectrum. The clearance height,  $d$ , was set to 4 different values: 0.0, 0.5, 1.0, and 1.5m above the still water level as mentioned earlier.

The combinations of  $H_s$  and  $T_p$  used in this study for generating input velocities were from an environment contour having a 100-year return period for the Gulf of Mexico (Winterstein et al. 1996) as shown in Figure 7-2 for the 100-year pdf contour.

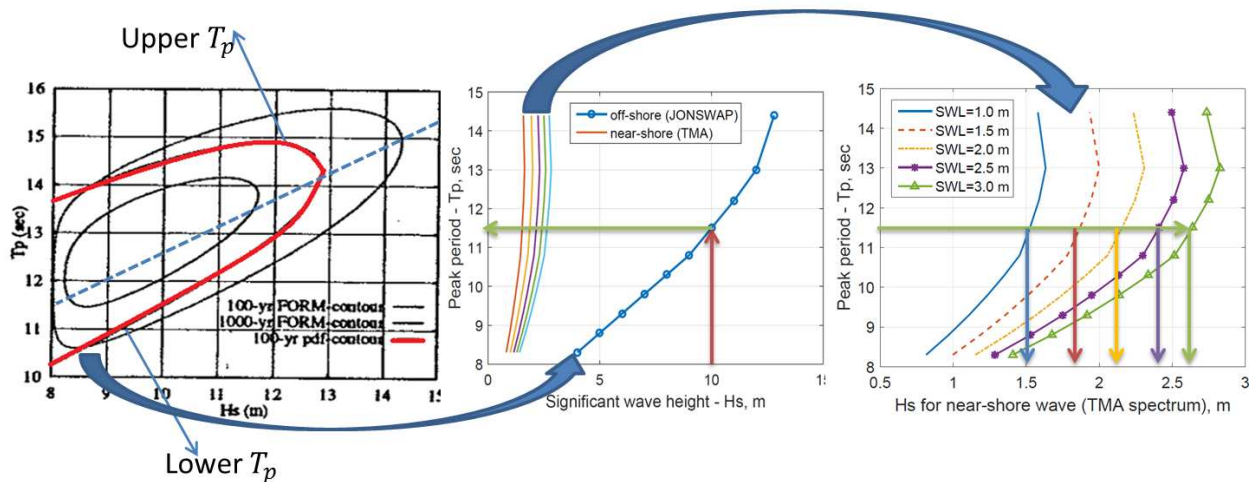


Figure 7-2. Environmental contours from deep to shallow water

The existing data set only used a sea state with  $H_s$  equal to or greater than  $8m$ . Sea states with  $H_s$  smaller than  $8m$  were obtained by extrapolation. The peak period was modeled as conditional probability in relation to significant wave height, thus there are two values of peak period ( $T_p$ ) which have the same probability of occurrence termed the upper and lower  $T_p$  (Table 7-1).

Table 7-1. Sea state from 100-year PDF environmental contour for Gulf of Mexico

	$H_s$ (m)									
	4	5	6	7	8	9	10	11	12	12.8
<b>Upper <math>T_p</math> (s)</b>	11.6	12.1	12.6	13.1	13.6	14.1	14.5	14.7	14.9	14.4
<b>Lower <math>T_p</math> (s)</b>	8.3	8.8	9.3	9.8	10.3	10.8	11.5	12.2	13.0	14.4

Figure 7-3 through Figure 7-6 present the results for a specific sea state ( $H_s = 12m, T_p = 13s$ ). The JONSWAP wave power spectrum of each sea state ( $H_s, T_p$ ) for deep water waves was transformed to the TMA spectrum for a 3 m depth shallow water wave and is shown in Figure 7-3. From the TMA spectrum, a time series for the sea state was simulated numerically using the procedure described earlier in section 5 (step 7). This simulated time series of a sea state (water elevation) was then transformed to the frequency domain for comparison to the target spectrum in Figure 7-4a. It should be noted that the term “simulated” indicates the time series wave is transformed directly from TMA spectrum, matching the target TMA spectrum as described in the procedure. Recall that the time series also follows the Weibull distribution as the prescribed distribution. Finally, through this process the velocity profile for the numerical wave maker can be obtained.



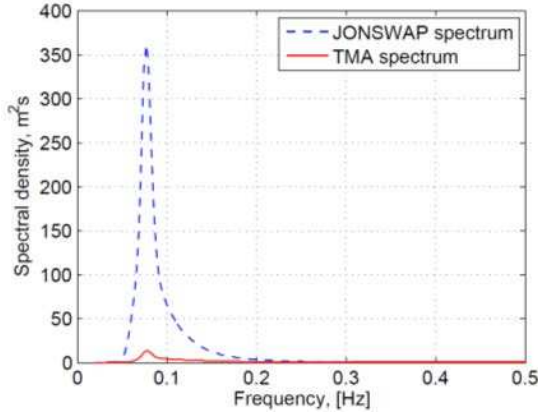


Figure 7-3. Transform action for the JONSWAP spectrum to the TMA spectrum for  $H_s = 12\text{ m}$ ,  $T_p = 13\text{ s}$ , shallow water at height  $h = 3\text{ m}$

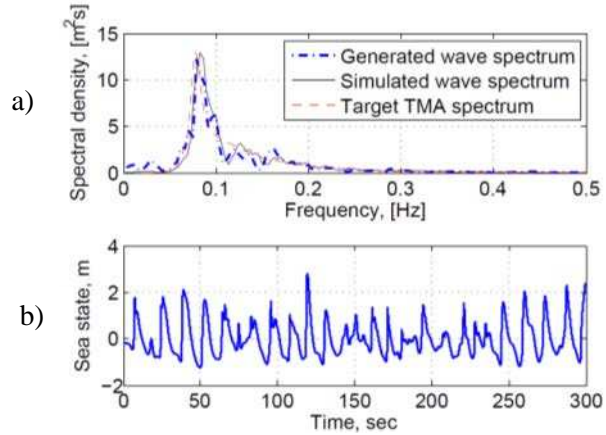


Figure 7-4. Generated versus Simulated wave spectrum and generated sea state for  $H_s = 12\text{ m}$ ,  $T_p = 13\text{ s}$ ,  $h = 3\text{ m}$

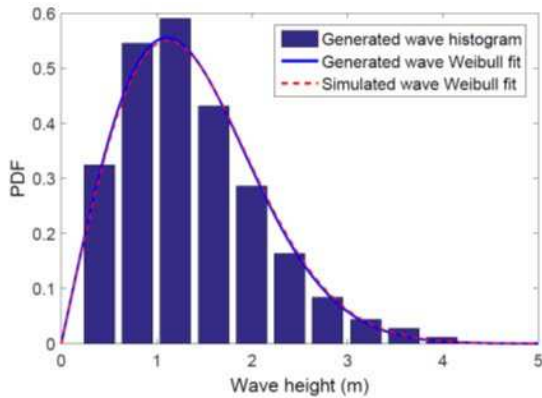


Figure 7-5. Wave height distribution for  $H_s = 12\text{ m}$ ,  $T_p = 13\text{ s}$ ,  $h = 3\text{ m}$

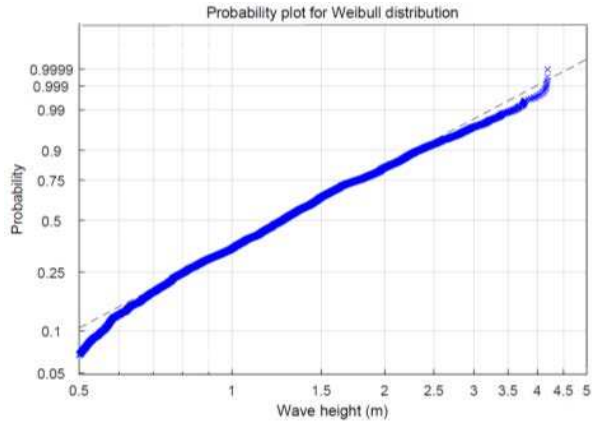


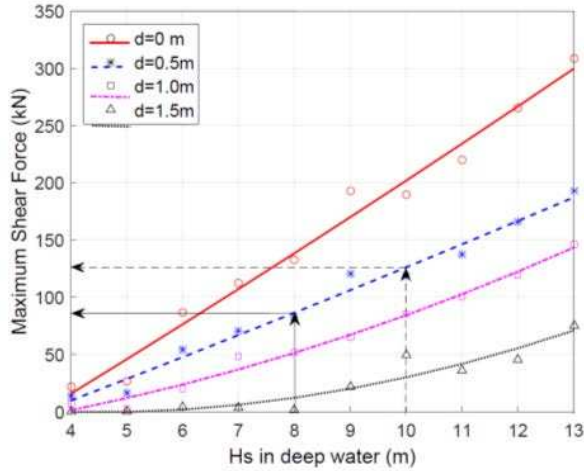
Figure 7-6. Weibull fit for generated wave height distribution

This velocity profile was then applied to the numerical water flume in step 8 to generate the numerical waves. The time series for the water surface elevation generated using this procedure were specified as the “generated” waves as shown in Figure 7-4b. This generated time series was then transformed to the frequency domain to create the “generated” wave spectrum shown in Figure 7-4a. The generated wave distribution in the Figure 7-4a is very closely matches

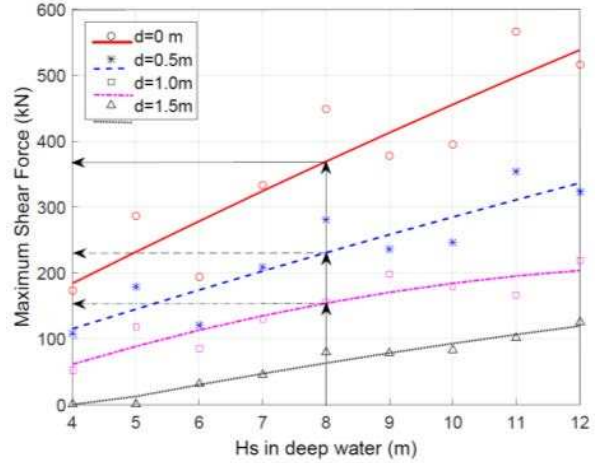
the simulated wave distribution and the Weibull distribution as shown in Figure 7-5 and Figure 7-6. This generated wave spectrum can be compared to the measured wave spectrum from the experimental wave flume. The area under the spectrum represents the variance of sea surface displacement,  $\sigma^2$ . The generated significant wave height was determined as  $H_{sg} \cong 4\sigma$ . This  $H_{sg}$  decreases as the distance from the wave maker to the measurement location increases due to energy loss.

The model for the bridge in the numerical wave flume in ABAQUS were presneted earlier Figure 7-1. The maximum values for shear and uplift when the wave hits the structure for four different clearance heights ( $d = 0m, d = 0.5 m, d = 1.0m, \text{ and } d = 1.5m$ ) are illustrated in Figure 7-7. In this Figure, the left windows show the results for the upper peak period while the other side shows for the lower  $T_p$  values. It should be noted that all these  $H_s - T_p$  combinations have an equal occurrence probaility. In addition, the  $H_s$  in deep water is shown on the abscissa of each window plot and therefore represents the reference significant wave height prior to its being converted to the TMA spectrum since seastates are typically defined for deep water with a time series generated for subsequent analysis. Shear and uplift forces were obtained directly from the support reactions. In these figures, linear regression was used to fit to the data.

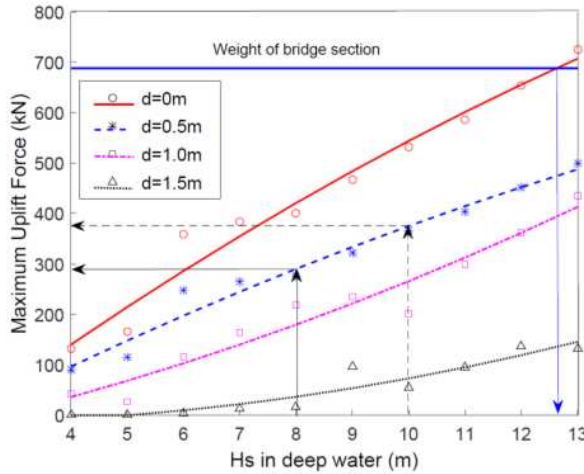
Inspection of Figure 7-7 indicates that wave loading appears to escalate almost linearly with significant wave height in most cases. For example, an increase in significant wave height from 8 m to 10m increases the maximum shear from 86kN to 126kN in Figure 5-7a if  $d = 0.5m$ . as shown through the insert arrows. At the same time, in Figure 7-7b, the maximum uplift force increases 290kN to 375kN for  $d = 0.5m$ .



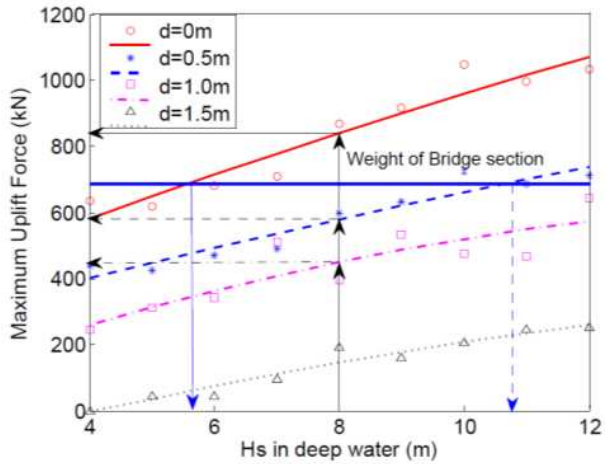
(a) Shear force, upper  $T_p$



(c) Shear force, lower  $T_p$



(b) Uplift force, upper  $T_p$



(d) Uplift force, lower  $T_p$

Figure 7-7. Maximum impact loadings on bridge model

In addition, also from Figure 7-7, it is apparent that for the same significant wave height, the sea states with a shorter peak period experience higher wave forces. For example, maximum shear observed in the lower  $T_p$  (Figure 7-7c) are almost double the case for the upper  $T_p$  (Figure 7-7a). In terms of maximum uplift force, it is interesting that in the upper case, maximum uplifts do not exceed the self weight of the bridge section although the wave surge level are at the bottom of the bridge girder and  $H_s$  is at a height of 12m (Figure 7-7b). However, the uplift

forces exceed the self weight of structure in the lower case (Figure 7-7d) for  $d = 0m$  and  $d = 0.5m$ , which may result in damage to the structure. The observation that (1) shorter periods results in substantially larger uplift forces, and (2) certain combinations of  $H_s$  and  $T_p$  results in uplift forces greater than the self-weight of the bridge, is consistent with the conclusion from Brader et al. (Bradner et al. 2008) experimental work.

In addition, increasing the clearance height of the structure will also reduce the effects of wave loading and is a routinely utilized approach, but can be costly if approaches to the bridge are taken into account. For example, maximum shear decreases from  $370kN$  to  $230kN$  and  $155kN$  when the clearance height is increased from  $0.0m$  to  $0.5m$  and  $1.0m$ , respectively, for the lower  $T_p$  case with  $H_s = 8m$  (Figure 7-7c). Similar trends were observed for uplift forces. For the same conditions, the maximum uplift force falls from  $840kN$  to  $580kN$  and  $450kN$  (Figure 7-7d).

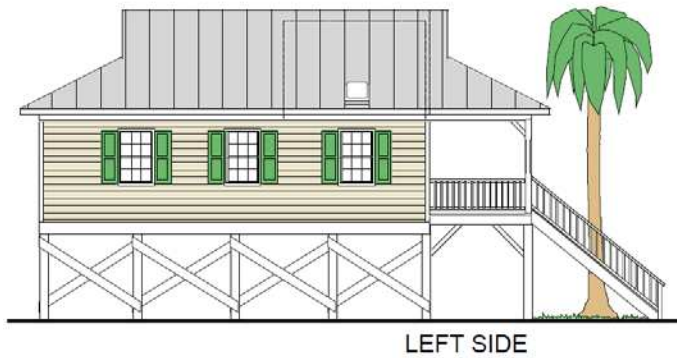
### *7.1.2. Wave loading on buildings using the ANSYS Fluent Model*

#### *7.1.2.1. One-story elevated residential building*

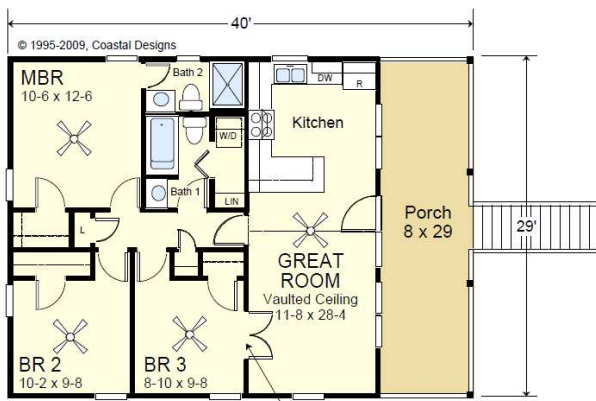
A typical one-story coastal elevated residential building (Figure 7-8) was served as example for an elevated residential building in a coastal zone. First, the building was modeled using solid elements in ANSYS as shown in Figure 7-9. Next, the fluid domain around the building was modeled as a rectangular block which has dimensions of  $700 \times 1000 \times 320in$  (approximately  $17.8 \times 25.4 \times 8.1m$ ). For one-way fluid/structure interaction modeling, the fluid domain was subtracted from the building making internal boundary surfaces for the fluid domain. In this analysis, the internal walls for building were removed and all building windows and doors were opened. This internal boundary for the fluid domain remain as fixed walls for the fluid during the analysis.



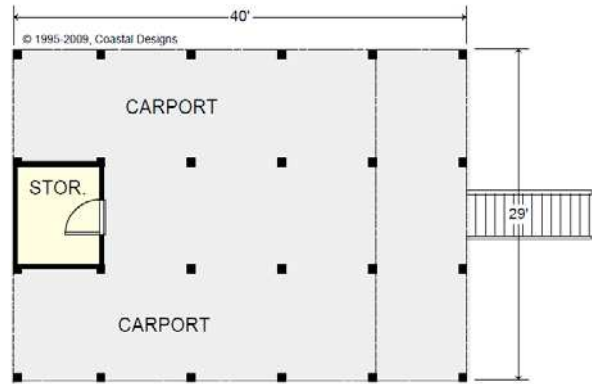
a) Front view



b) Side view



c) Floor plan view



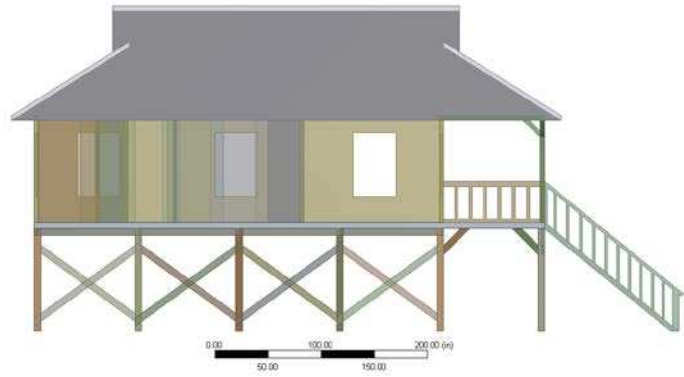
d) Ground plan view

Figure 7-8. Example of one –story elevated residential building in Carolina Island

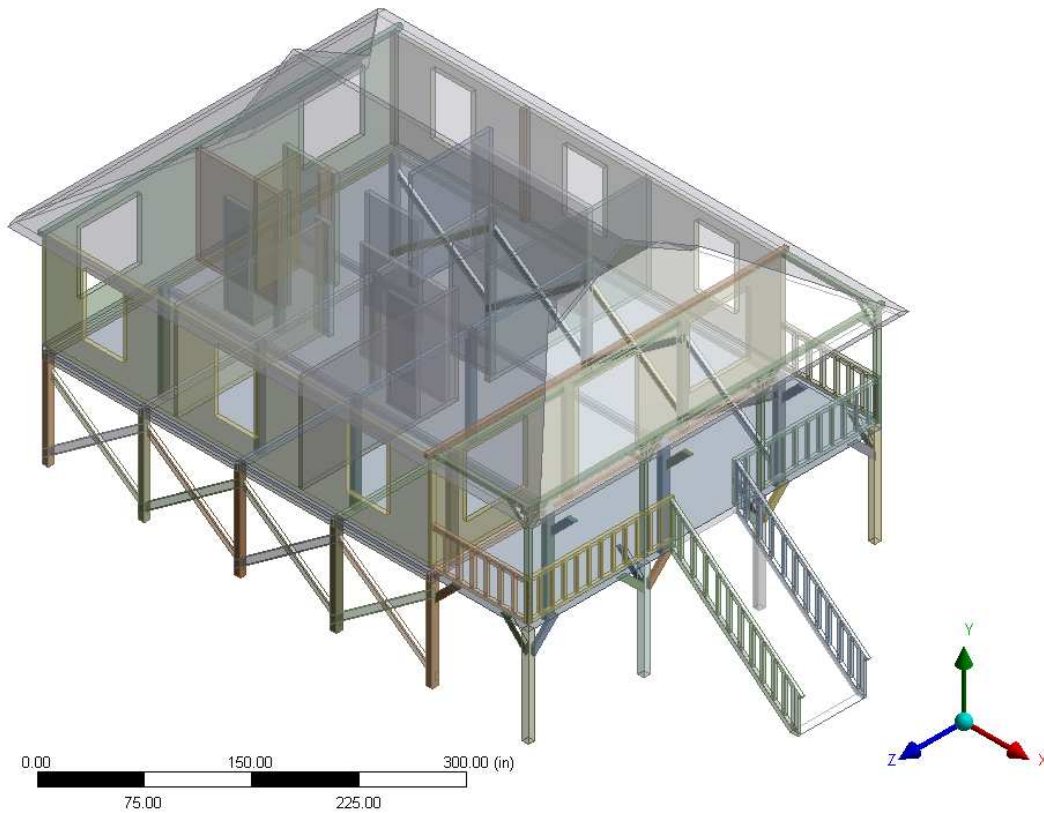
([www.coastaldesign.com](http://www.coastaldesign.com))



a) Front view



b) Side view



c) 3-D view

Figure 7-9. Model of the one-story elevated near coast building in ANSYS, all windows and doors are opened

The fluid domain consists of two different mediums, namely air with a density of  $1.225\text{kg}/\text{m}^3$  and sea water with a density of  $1003\text{kg}/\text{m}^3$ . The cut-cell mesh method (ANSYS

2013) with cubic element dominant was applied to mesh the fluid. The element size of the fluid domain was set to 12 inches which is felt to be fine enough to load the structure effectively. For the five layers next to the building contact surfaces, the element size was reduced smoothly to 3 inches with a grow rate of 1.2. There were total 967,615 elements and 880,474 nodes, which are shown in Figure 7-10.

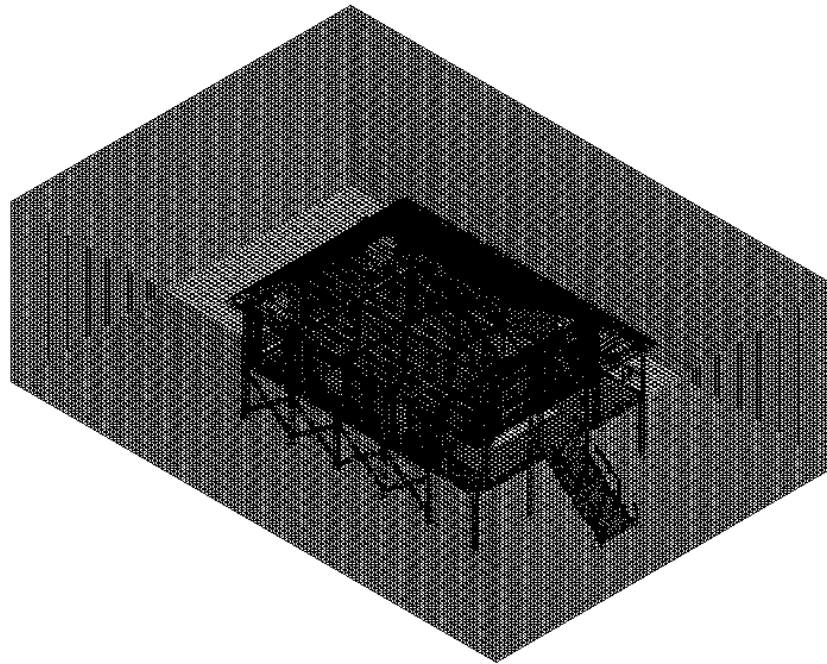


Figure 7-10. Fluid domain meshed for one-story elevated building in ANSYS

Boundary conditions then were applied to the model. Wave direction was assumed perpendicular to the front of the building. At the flow-in face of the fluid domain, open channel boundary conditions with a TMA wave spectrum were applied. The initial water surface was set to be a wavy condition to save time for wave development as shown in Figure 7-12a. Input parameters for the TMA wave spectrum are the significant wave height ( $H_s$ ), peak period ( $T_p$ ), surge level ( $S$ ) or water depth level. Figure 7-11 explains the definition of surge level and clearance height used in this study. It is noted that significant wave height in shallow water depends on surge level and surge level is also a variable (Figure 7-2). Therefore, reference



significant wave heights used in this analysis are of deep water only. The cut-in and cut-out frequency are  $0.1\text{rad/s}$  and  $2.0\text{rad/s}$ , respectively with a resolution of 50. The flow-out face of the fluid domain was also set to be zero pressure with open channel boundary condition and surge level was set to be the same to the in-flow face.

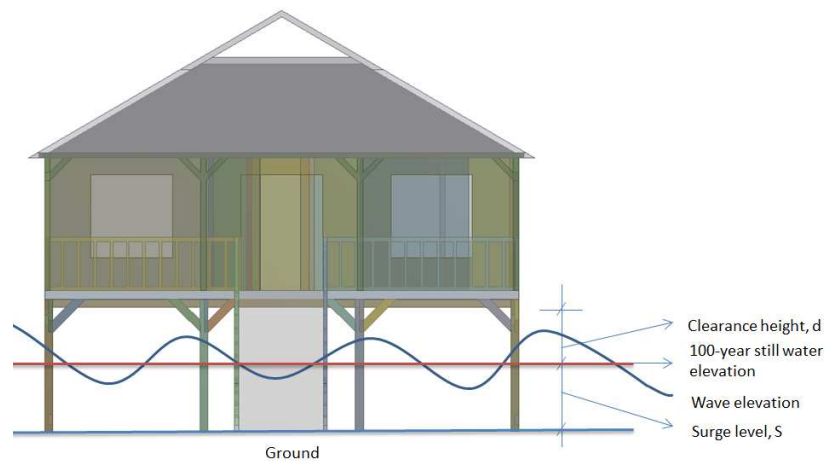
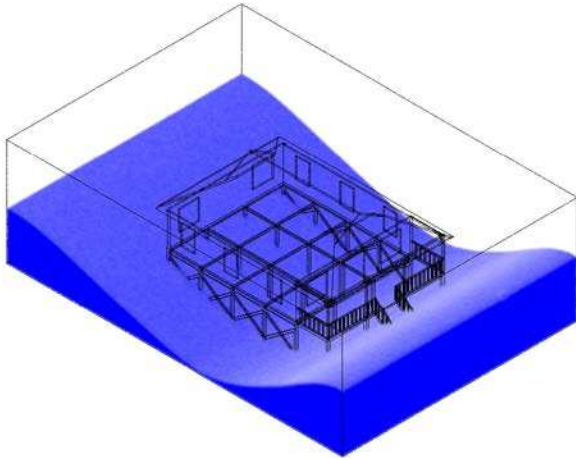


Figure 7-11. Define of surge level and clearance height

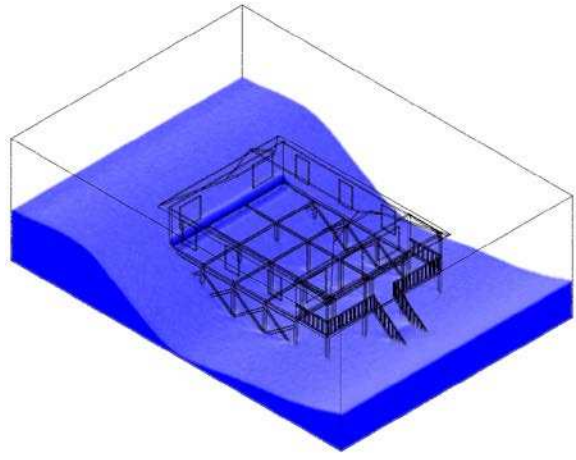
For each case of wave height and surge level, the analysis was run for 300 seconds using Compute Clusters at Colorado State University with 24 cores for each job. It takes 8 to 10 hours to complete analysis for one case.

Figure 7-12 shows the case of hurricane wave with the TMA spectrum of significant wave height at deep water  $H_s = 6\text{m}$ ,  $T_p = 9.3\text{s}$  hitting the elevated building. It can be seen that the start of water action to the building wall and slab occurs at 1.0 second (Figure 7-12b). Then, it propagates through the opened window as shown in Figure 7-12c and Figure 7-12d. The last two windows of Figure 7-12 show the water break after the wave hits the building.

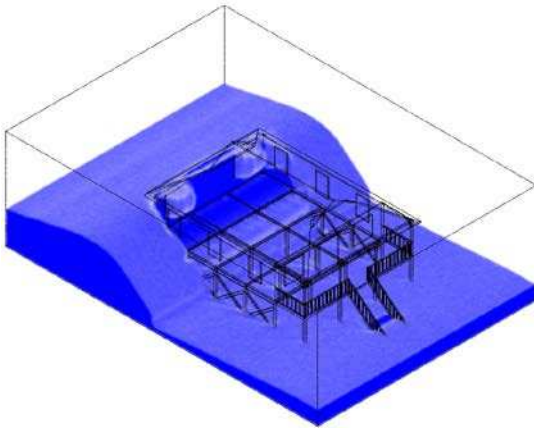




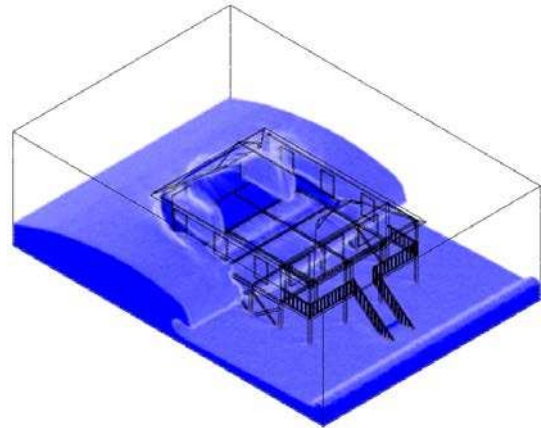
a) At 0.0 second



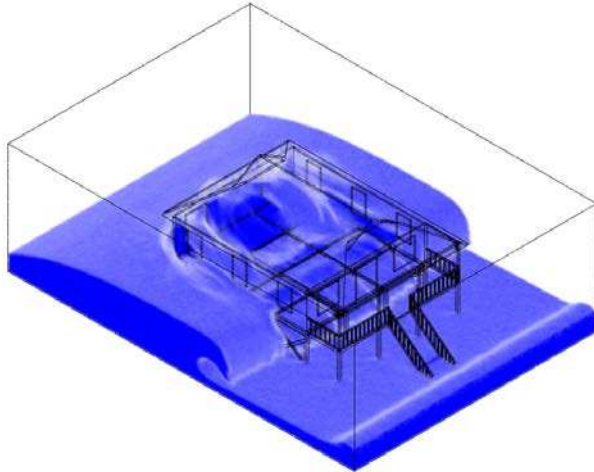
b) At 1.0 second



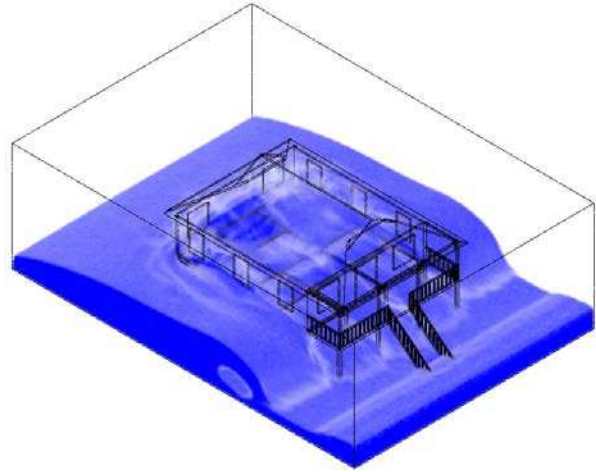
c) At 2.0 second



d) At 3.0 second



e) At 3.5 second



f) At 4.0 second

Figure 7-12. Rendering of the volume fraction for the sea water phase

Total shear and uplift on the building walls and slab were collected during analysis and presented in Figure 7-13 through Figure 7-16. At surge level of 3.0m, shears and uplifts increase

with the increase of significant wave heights. At the same trend, shear and uplift are also increase when surge level grows from 1 to 3m at significant wave height of 9.0m.

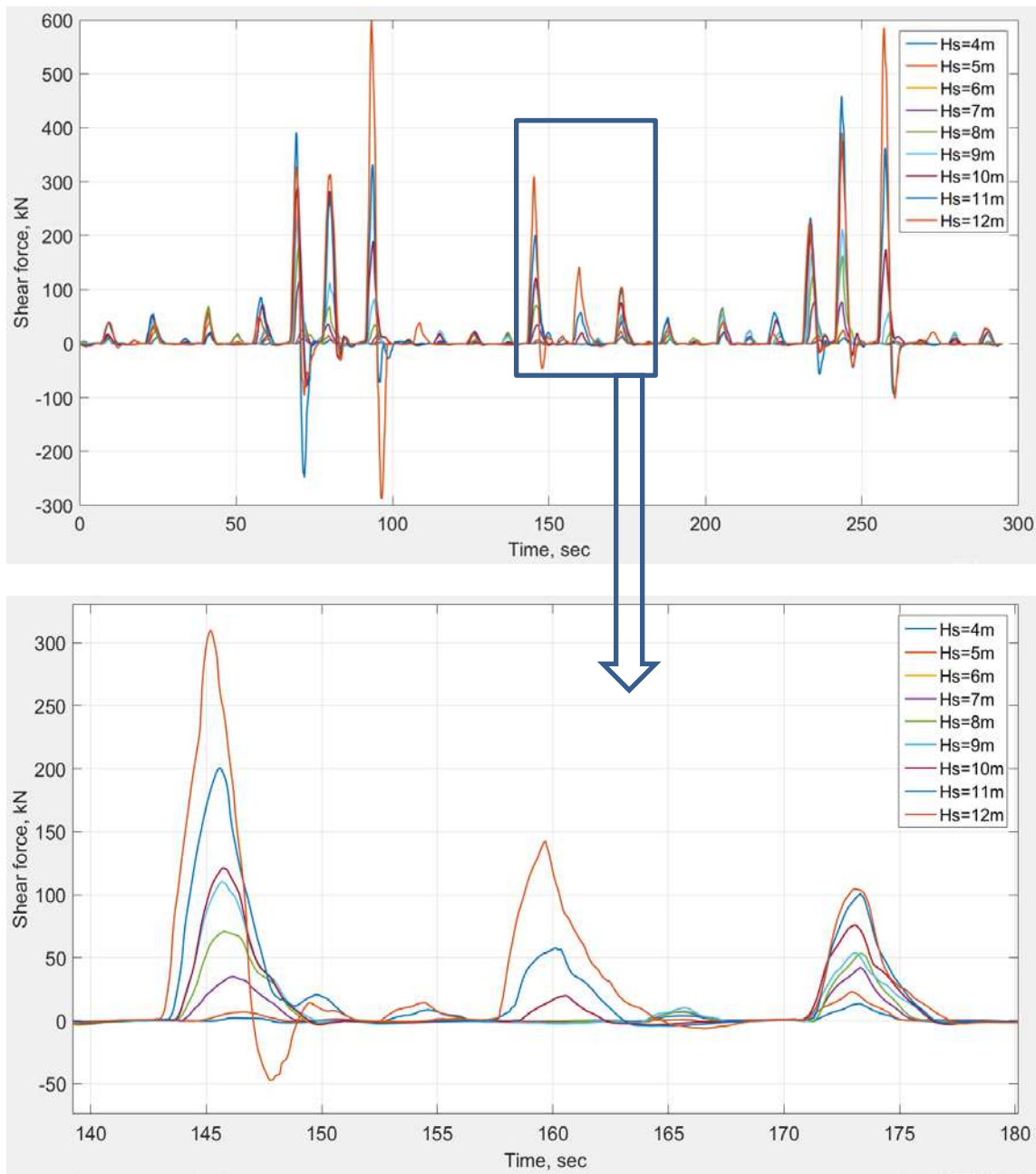


Figure 7-13. Total shear force for different wave heights at surge level = 3m

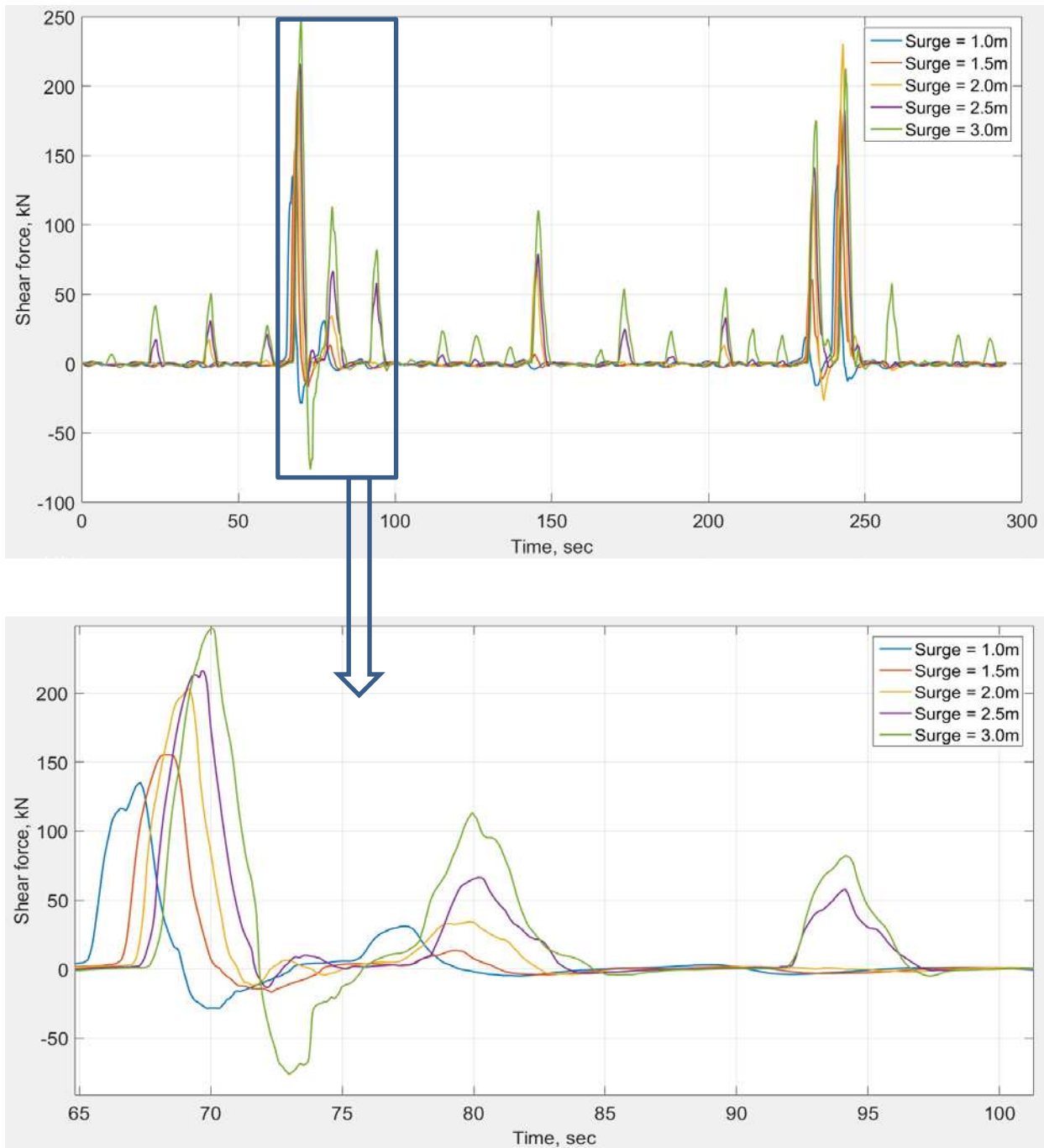


Figure 7-14. Total shear force for different surge levels at  $H_s = 9$  m,  $T_p = 10.8$  sec

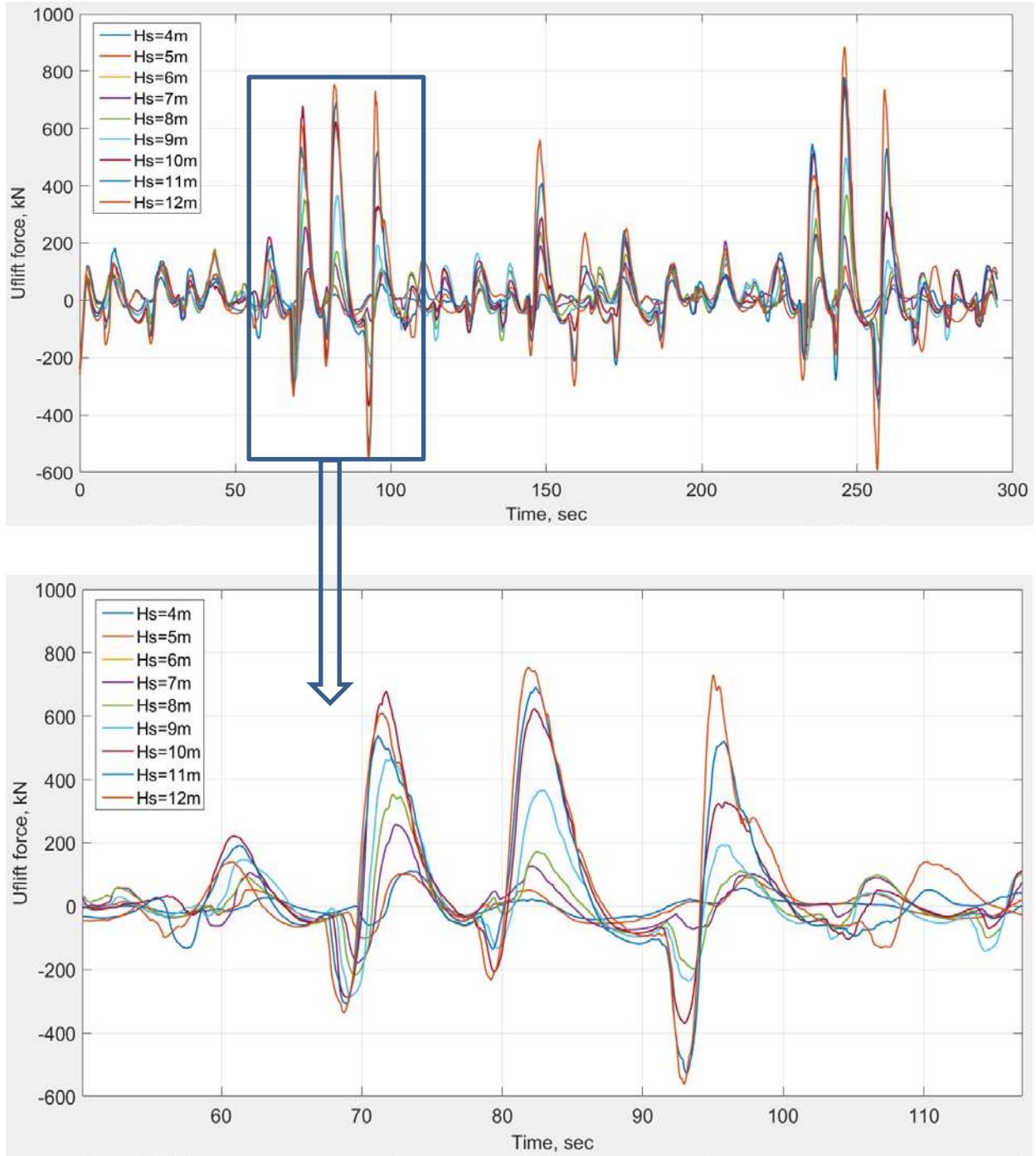


Figure 7-15. Total uplift force for different wave height at surge levels of 3.0 m



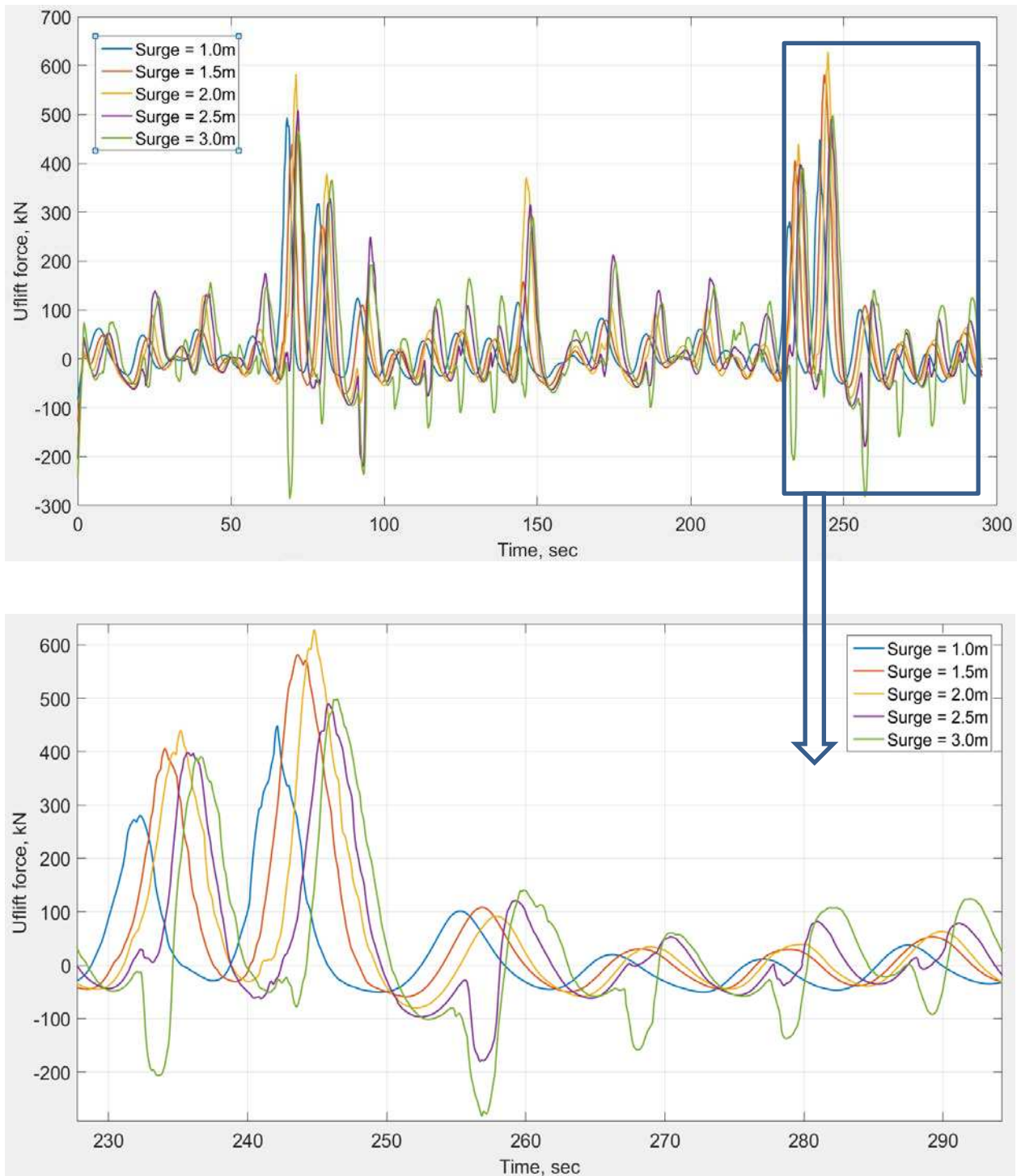


Figure 7-16. Total uplift force for different surge levels at  $H_s = 9$  m,  $T_p = 10.8$  sec

Total of 45 combinations of significant wave height and surges were analyzed in this study for the one-story building. Numbers of peak values for shear/uplift were determined by the number of zero up-crossing during the 300-second analysis for each combination. For every zero up-crossing event, a peak value of shear/uplift was collected. The mean values of the peaks for shear/uplift for every combination are shown in Figure 7-17. It is interesting that the means of the peaks also increase gradually with significant wave height and surge. This feature is very important for developing a fragility surfaces later in this study to ensure that probability of failure increases monotonically with the hazard intensity such as the combination of significant wave height and surge level.

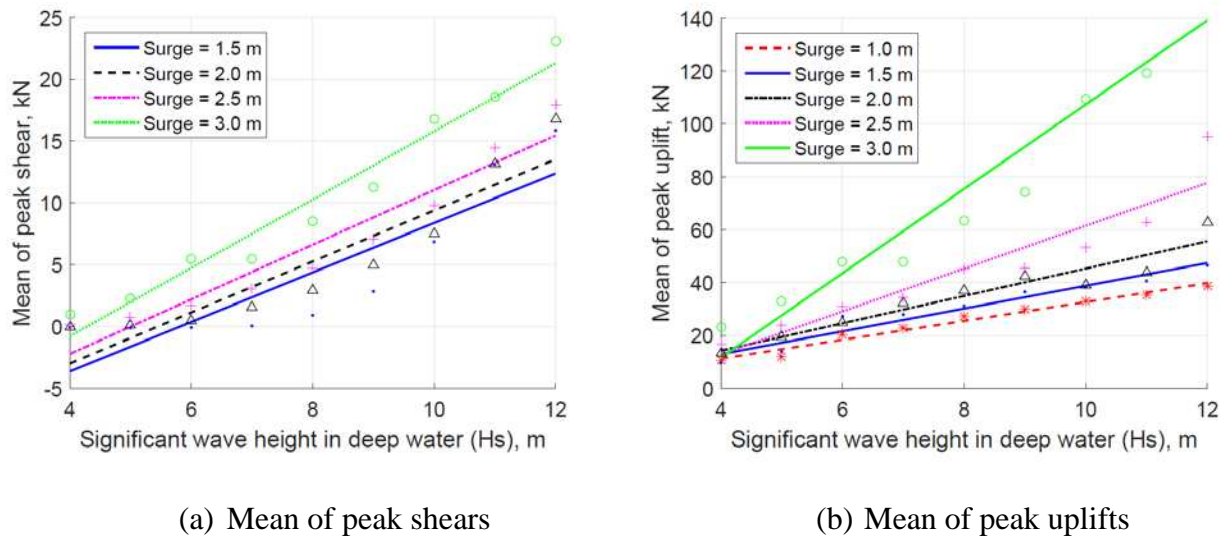


Figure 7-17. Mean of peak up lift and shear per unit width for one-story building

7.1.2.2. *Two-story elevated residential building*

A typical two-story coastal elevated residential building (Figure 7-18) was used as an example for this elevated building example.. Again, the building was model in ANSYS but all windows and doors were now closed (Figure 7-19). The building was elevated to 3m from the ground.



Figure 7-18. Example of two –story elevated building in Carolina Island

([www.coastaldesign.com](http://www.coastaldesign.com))

The fluid domain has dimensions of  $1700 \times 1500 \times 600in$  (approximately  $43.2 \times 38.1 \times 15.2m$ ) and the wave direction was assumed to be perpendicular to the left side (which has uncovered porch) of the building. The fluid domain mesh technique was used, which was as the one-story building and element size was consistent with the earlier example. Finer

resolution of the mesh was applied to the contact surfaces and the five layers next to building walls with a full mesh presented in Figure 7-20. There were a total of 1,567,005 nodes and 1,432,613 elements. Mesh resolution was optimized to save computing resources and to ensure that the analysis obtained convergence within 20 iterations at each time step of 0.001 seconds. The boundary conditions were exactly the same as the one-story case. The analysis was also for a time duration of 300 seconds. With the same 24 core for each job, it took about 12 to 15 hours to complete one analysis. Figure 7-21 presents the results of wave-structure interaction for one wave with  $H_s = 12m, S = 1.5m$ .

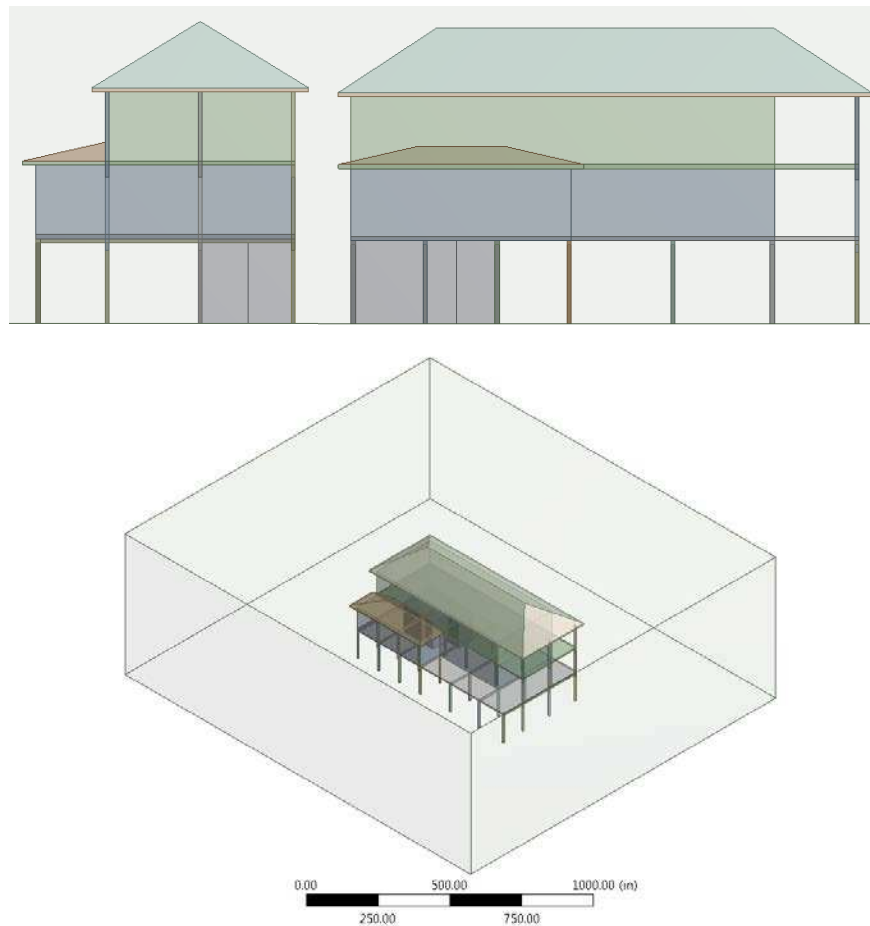


Figure 7-19. Model for two-story elevated building in ANSYS, all windows and doors are closed



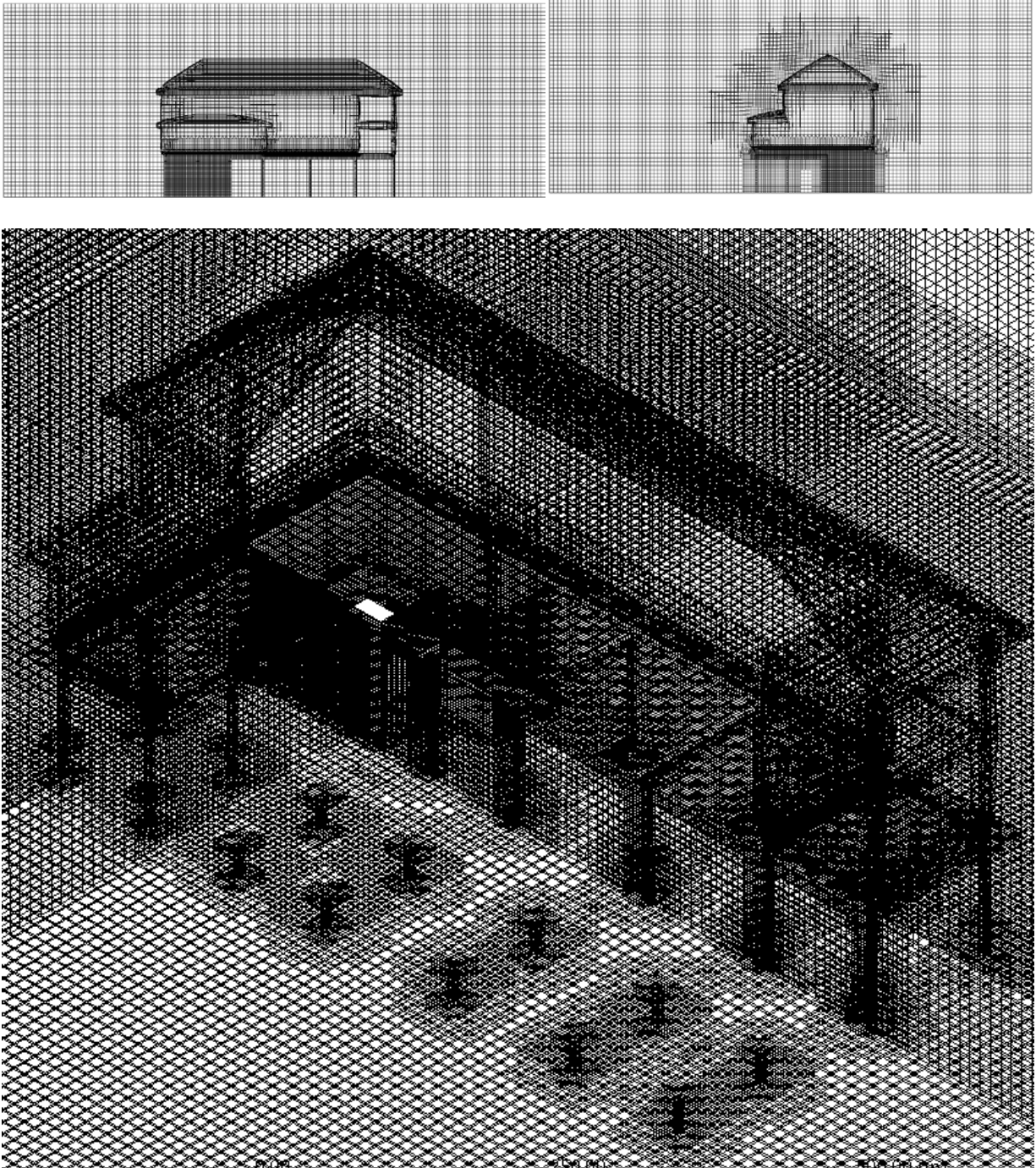
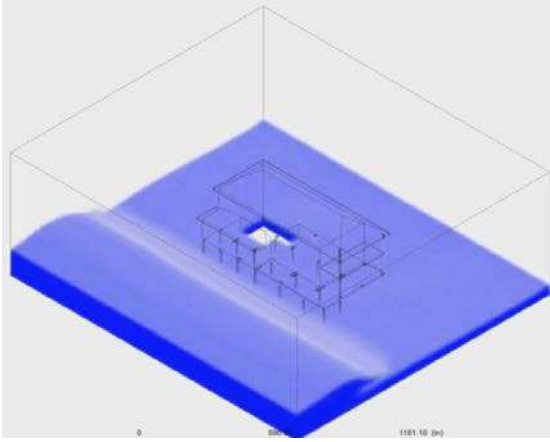
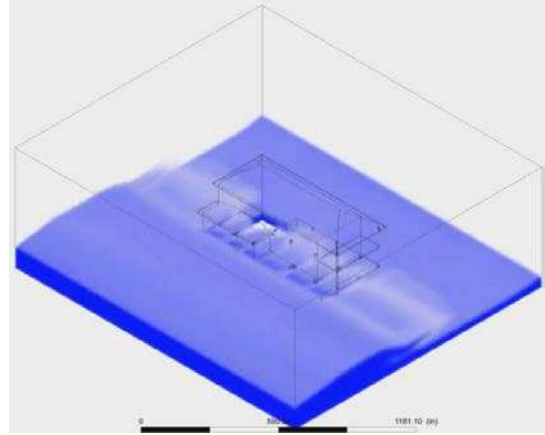


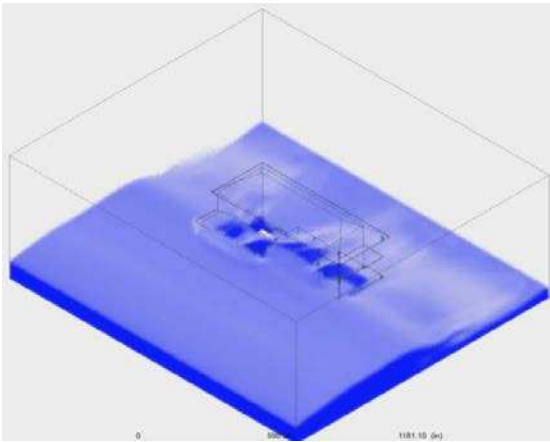
Figure 7-20. Mesh of the fluid domain for two-story building in ANSYS with smaller elements near the building surfaces



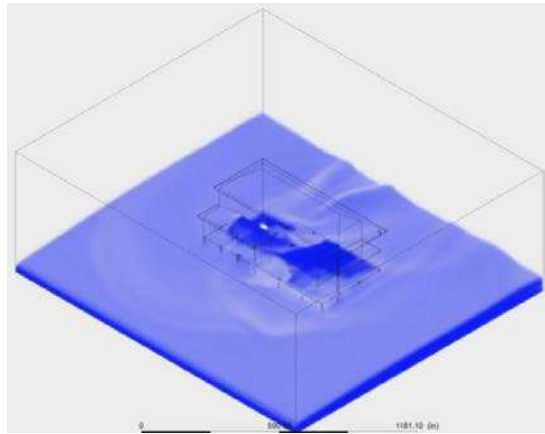
a) At 0.0 second



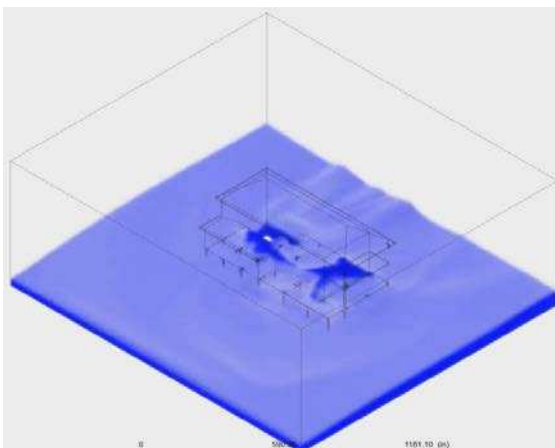
b) At 0.5 second



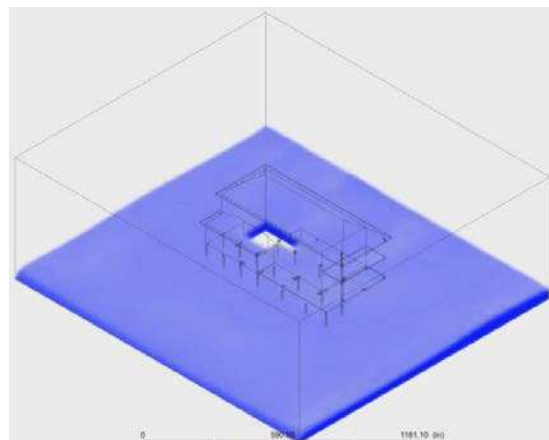
c) At 1.0 second



d) At 1.5 second



e) At 1.75 second



f) At 2.0 second

Figure 7-21. Wave-structure interaction for  $H_s = 12m, S = 1.5m$

The results of shear and uplift for 45 combinations of sea-state with reference significant wave height at deep water, ranging from 4 to 12m; and surge from 1.0 to 3.0m are shown in Figure 7-22. Total shear/uplift per unit width can be compared between the one-story and two-story building by contrasting Figure 7-17 and Figure 7-22. It can be seen that total shear forces observed for the two-story building are about 1.5 times those for the one-story building. However, total uplifts are essentially the same as one would expect.

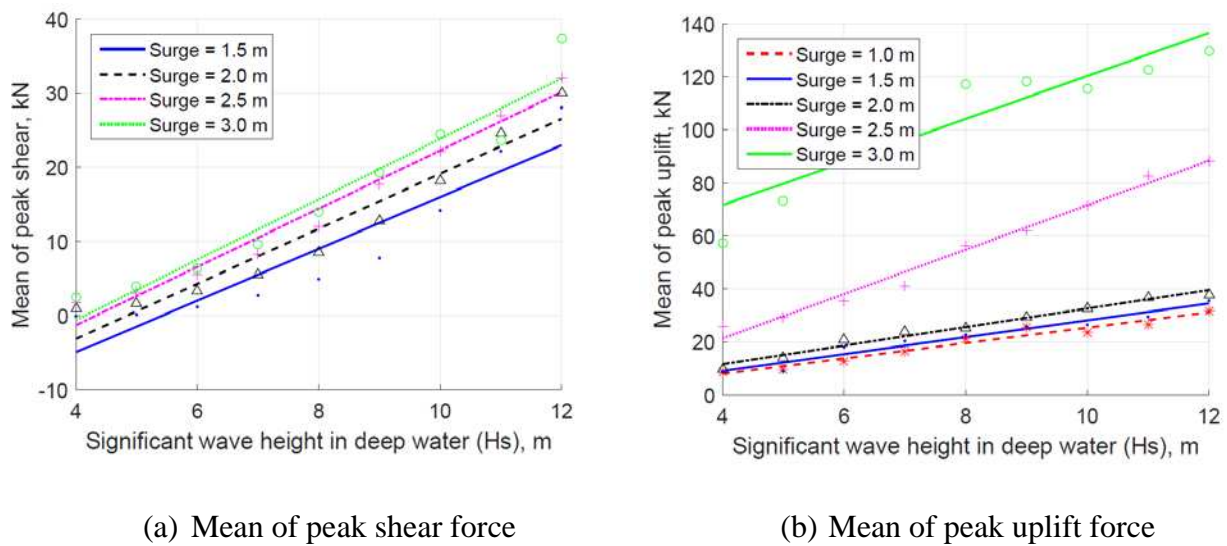


Figure 7-22. Mean of shear force and uplift force per unit width for the two-story building

## 7.2. Performance-Based design of elevated coastal structures using fragility methodology

### 7.2.1. Performance-Based design concept of elevated coastal structures

As discussed earlier, performance-based design is a concept used to design structures to meet predefined and desired levels of performance under usually extreme hazard conditions such as earthquake, hurricane waves, wind, tornado, fire, etc. To define the levels of damage or performance, large scale or full scale tests are required to determine the levels of damage that correlate to the hazard intensities. Figure 7-23 explains the concept of performance-based design

for elevated coastal structures proposed in this dissertation. For example, at a certain wave height and surge level, the performance of a structure can be divided into levels such as: 1.) there is no damage or the structure is still fully operational, 2.) the structure has light damage and can be used after some repairs, 3.) the structure has severe damage and cannot be fixed, however, it is not collapsed and still has enough time for evacuation and therefore there is likely no loss of life, and 4.) structure has collapsed and there is likely loss of life. To quantify the four articulated levels of performance, some levels of capacity (uplift and shear, etc.) must be defined for design. If the wave loading (demands) exceed these capacities, the structure is assumed to have failed. The probability that the wave loadings exceed some structural capacity given conditions such as wave heights and surge levels is known as fragility curves and are conceptually illustrated in Figure 7-23.

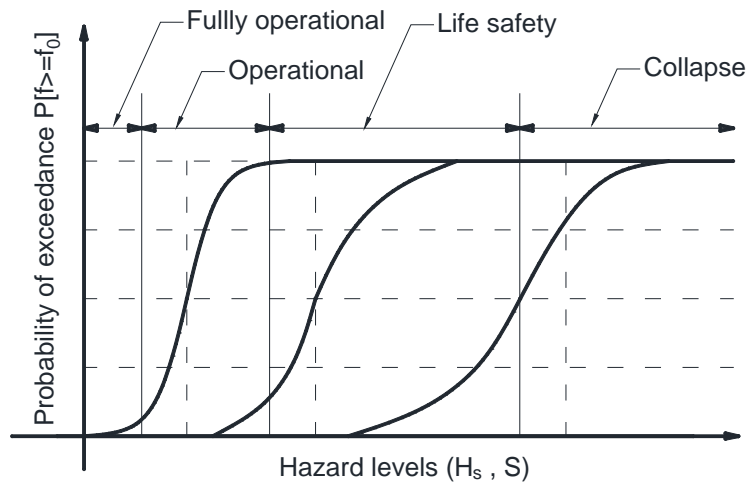


Figure 7-23. Conceptual fragility curves for elevated coastal structures

The procedure for constructing a fragility curve for a elevated coastal structure for a specified significant wave height ( $H_{Si}$ ) and surge level ( $S_i$ ) is explained in Figure 7-24. Surge level can also be treated as a design variable, namely as clearance height,  $d$  (Figure 7-11). For each combination of significant wave height and surge level, a time history of uplift and shear

force ( $f_{ij}$ ) can be collected from the analysis models described earlier. Then,  $N$  peak values of the force correlated with  $N$  zero up crossings are collected. The probability of the peak values exceeding a certain capacity,  $f_o$ , is defined as one point of the fragility curve as  $F_{ij}$ . Finally, a lognormal curve will be obtained to fit all the  $F_{ij}$ 's points to make a complete fragility curve as shown in Figure 7-24.

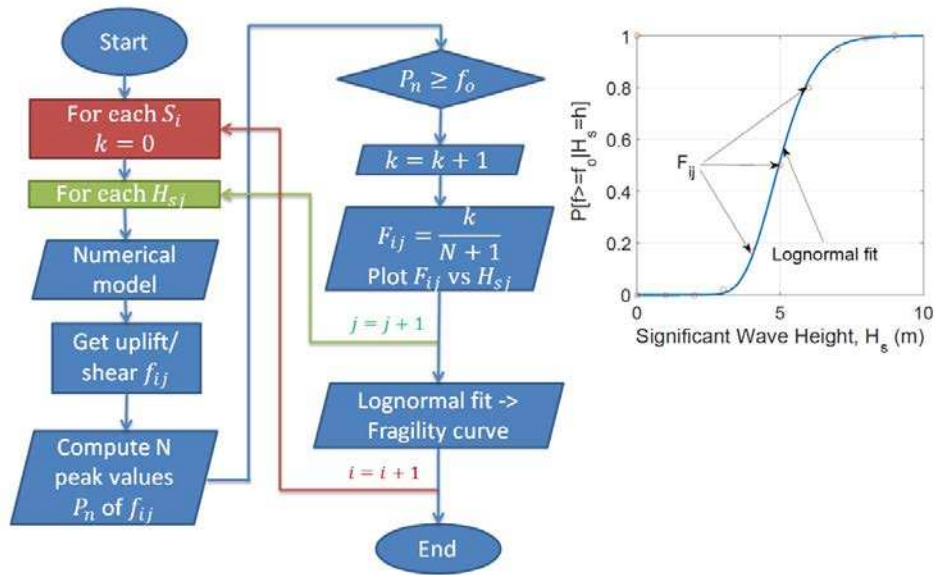


Figure 7-24. Procedure for constructing a fragility curve for structure under wave load

### 7.2.2. Performance-Based design of coastal bridge using fragility curves

In this design example, fragility curves are constructed only for the uplift forces as a function of  $H_s$  and surge level or clearance height,  $d$ , for illustrative purposes. Further, fragility curves are only generated for the case of the lower  $T_p$  which resulted in higher significant wave heights in shallow water and larger wave loading as shown earlier in Figure 7-7. The probability of failure in a 300 second sea state (5 minutes) for an uplift force time series was determined by the number of maximum uplift in each event that exceeds the capacity,  $f_o$ , divided by the total number of wave events. The number of wave events in a specific time period was determined as the total time divided by the peak period for each sea state. The fragility curves were constructed

by applying the lognormal fit to all the single failure points as shown in Figure 7-25a, Figure 7-25b, and Figure 7-25c for  $d = 0.5m$ ,  $d = 1.0m$ , and  $d = 1.5m$ , respectively. Three levels of capacity were specified to illustrate three different fragility curves for each case. The levels of capacity are assumed to be  $400kN$ ,  $600kN$  and  $800kN$ , which are equal to 60%, 90%, and 120% of the self-weight of the prototype bridge structure. The capacity level of  $800kN$  represents a case when the structure has been retrofitted to resist uplift force that can exceed its self-weight.

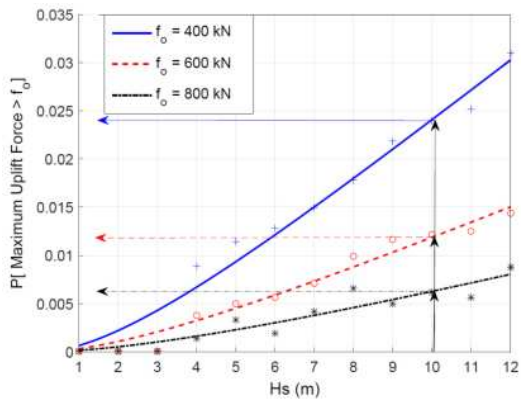
In general, the probability of failure increases with the significant wave height and decreases with an increase in clearance height,  $d$ , as one might logically anticipate. When  $d = 0.5m$  and  $H_s = 9m$ , for example, the probabilities that the maximum uplift exceeds three different levels of capacity are  $24 \times 10^{-3}$ ,  $11.8 \times 10^{-3}$ , and  $6.4 \times 10^{-3}$ , respectively, as shown by the arrows in Figure 7-25a. However, if the clearance height is raised to  $d = 1.5m$ , these numbers decrease significantly to  $2.3 \times 10^{-3}$ ,  $0.15 \times 10^{-3}$ , and  $0.71 \times 10^{-3}$ , respectively, as shown in Figure 7-25c.

Obviously, hurricanes do not last for only 300 seconds. To explain the probability of failures for a hurricane with a longer duration (e.g, 3 hours of a particular sea state), the transform action function which was modified from the equation by Luco et al. (Luco et al. 2007) as

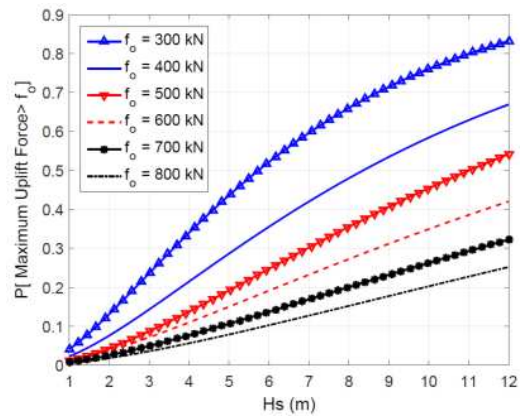
$$P_f[ \text{in } X \text{ hours} ] = 1 - (1 - P_f[ \text{in } Y \text{ hours} ])^{\left(\frac{X}{Y}\right)} \quad (7-1)$$

can be used. This indicates that the probability of failure in 3 hours is, of course, larger than that for a shorter duration, i.e. 300 seconds. The fragility curves for uplift loadings in 3 hours are presented in Figure 7-25d, Figure 7-25e, and Figure 7-25f for  $d = 0.5m$ ,  $d = 1.0m$ , and  $d = 1.5m$ , respectively.

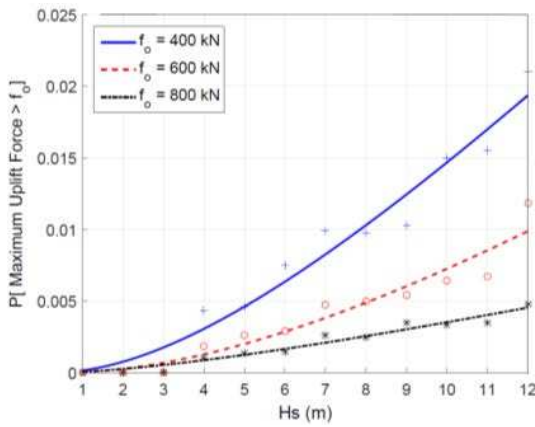




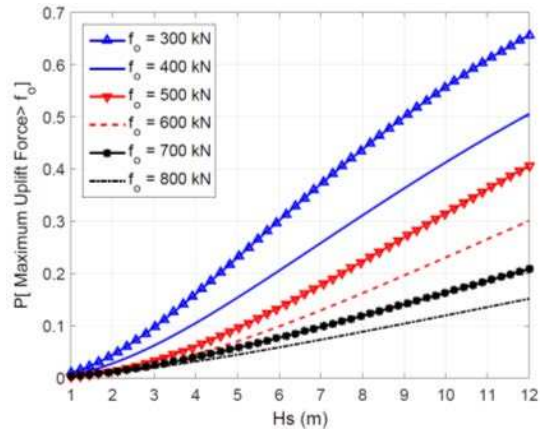
(a)  $d = 0.5 \text{ m}, t = 300 \text{ s}$



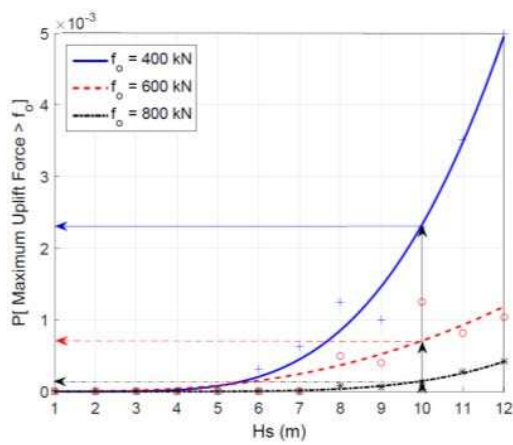
(d)  $d = 0.5 \text{ m}, t = 3 \text{ hour}$



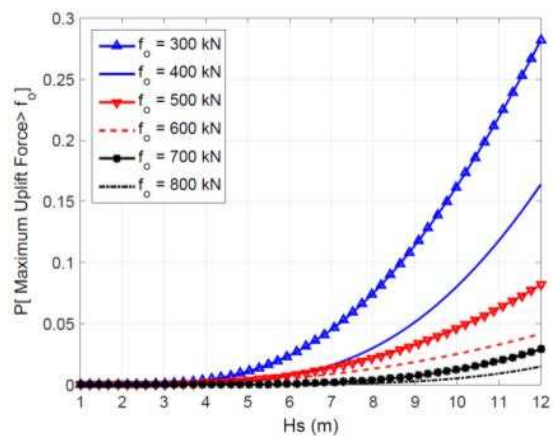
(b)  $d = 1.0 \text{ m}, t = 300 \text{ s}$



(e)  $d = 1.0 \text{ m}, t = 3 \text{ hour}$



(c)  $d = 1.5 \text{ m}, t = 300 \text{ s}$



(f)  $d = 1.5 \text{ m}, t = 3 \text{ hour}$

Figure 7-25. Fragility curves for impact loading on structure

From these figures for a known sea state, a design optimization can be established. In these figures, six levels of capacity are presented. To design a structure for uplift loading with a target probability of failure,  $P_f$ , one can adjust the uplift capacity,  $f_o$ , or change the clearance height,  $d$ . For example, a structure with an uplift capacity of  $600kN$  and clearance height of  $0.5m$  has a probability of failure equal to  $0.31$  during a hurricane with  $H_s = 9m$  (Figure 7-26). By raising the clearance height to  $1.0m$ , the same probability of failure can be achieved with an uplift capacity somewhere between  $400kN$  and  $500kN$ , as shown in Figure 7-26. By applying linear interpolation, the capacity for obtaining the same probability of failure when raising a structure to  $1.0m$  is approximately  $450kN$ .

To reduce the probability of failure, one can also obviously consider raising the clearance height to reduce the uplift force. For the same significant wave height of  $9m$ , if a structure with capacity of  $600kN$  is raised from  $0.5m$  to  $1.0m$  or to  $1.5m$ , the probability of failure decreases from  $0.31$  to  $0.19$  and  $0.02$ , respectively as shown in Figure 7-27a. If a retrofit solution was applied to increase the uplift capacity to  $800kN$  (120% self-weight), the probability of failure decreases significantly as one can see in comparing Figure 7-27a and Figure 7-27b.

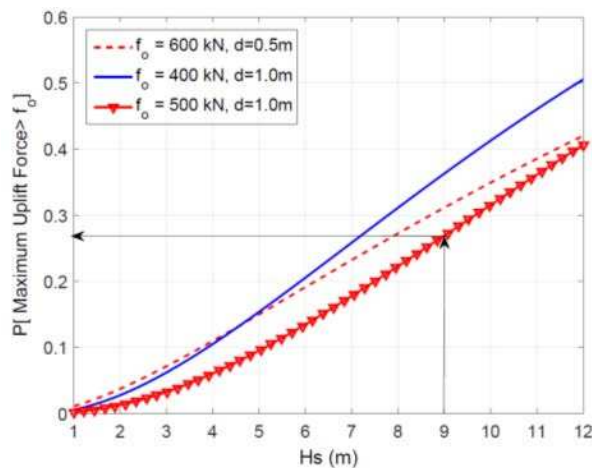
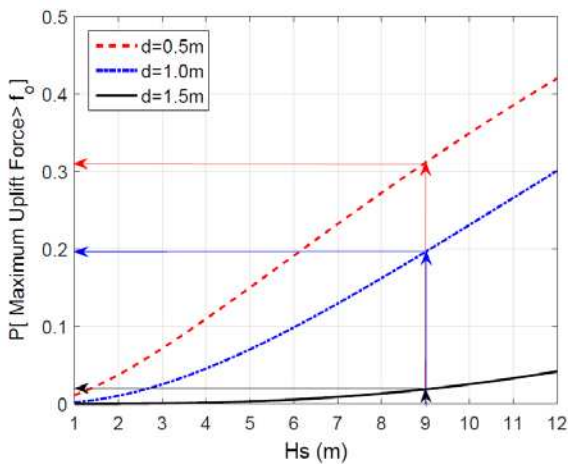


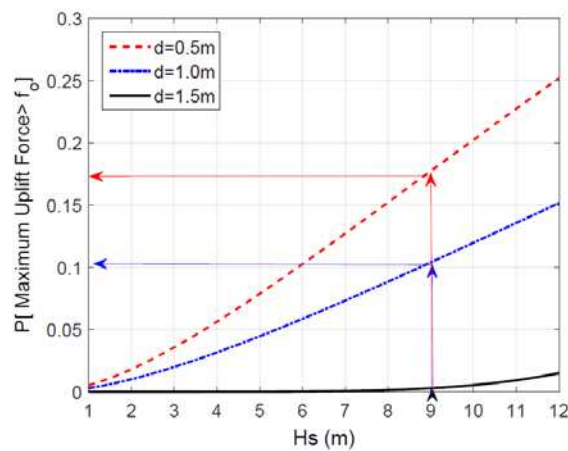
Figure 7-26. Design example using fragility curves for the same probability of failure



It is noted that although the probabilities of failure in the examples mentioned above are significantly high, these are conditional probabilities (fragilities) and assume the occurrence of an extreme event. If an unconditional probability of failure was desired, the fragility would be convolved with a hazard curve for the location of interest. The failure probabilities computed herein were based on the assumption that a hurricane with the stated significant wave height occurred for 3 hours. The clearance height of an elevated structure also depends on the surge level which could be varied in further analysis. The combination of significant wave height distribution and surge level with the proposed fragility curves will result in a complete model of probability of failure during a hurricane.



(a) uplift capacity  $f_o = 600 \text{ kN}$



(b) uplift capacity  $f_o = 800 \text{ kN}$

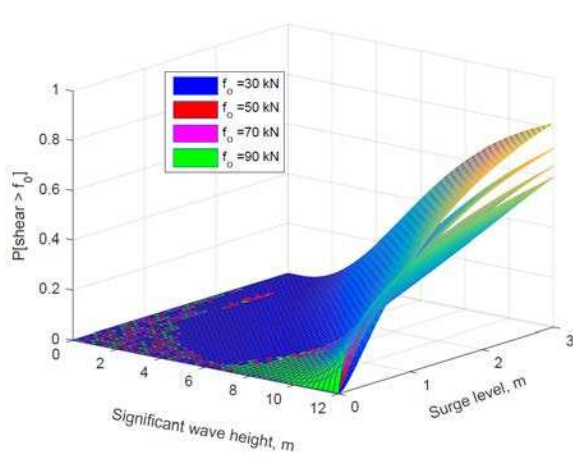
Figure 7-27. Design example using fragility curves to reduce probability of failure

### 7.2.3. Fragility surfaces for Performance-Based design of coastal residential buildings

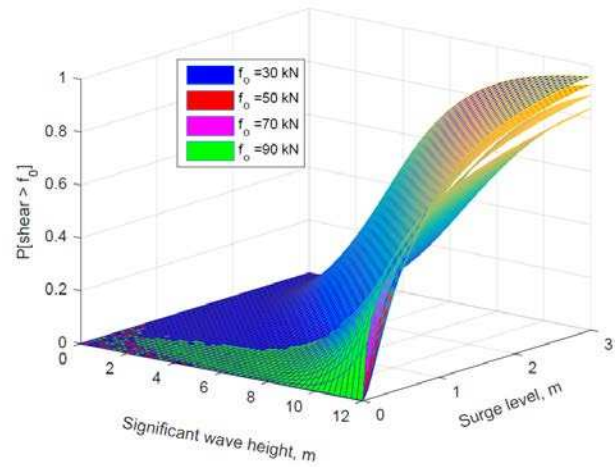
Fragility surfaces for shear/uplift are the conditional probability of shear/uplift exceeding specified capacity level given hazard intensity defined as a combination of significant wave height ( $H_s$ ) and surge level ( $S$ ). The capacities levels explained in the previous section are based on the guidelines at which the building will experience different performance levels. In this

study, four levels of capacity are investigated. For shear design, it is assumed that building will remain operational if total shear is less than or equal to  $30kN$  per unit width. If shear force is smaller than  $50kN$ , the building will experience some light damage and can be returned to normal operation after some repairs. If shear force is greater than  $50kN$  but less than  $70kN$ , the building will experience severe damage and cannot be repaired. When shear force is greater than  $90kN$ , the building may fail and life safety is an issue. The four capacity levels for uplift corresponding to these levels of performance for the building are assumed to be  $150kN$ ,  $200kN$ ,  $250kN$ , and  $300kN$ , respectively. For each of 45 combinations of significant wave height and surge level for each building, the peak values of uplift and shear are collected. Probability of failure then was determined by taking the number of peak that exceeds the capacity over the total number of zeros up crossings in 300 seconds. The procedure to get probability of failure in 3 hours from the probability of failure in 300 seconds has already mentioned earlier using Equation (7-1).

Fragility surfaces for shear and uplift for one-story and two-story building during a 3-hour hurricane have been demonstrated in Figure 7-28 and Figure 7-29. The figures show the effects of two hazard intensities to the probabilities of exceedance of shear/uplift. From the figures, specific probabilities of exceedance can be found if the significant wave height and surge level are given.

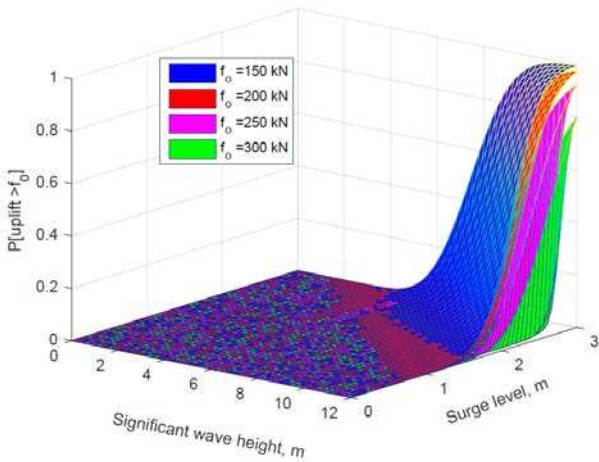


(a) one-story building

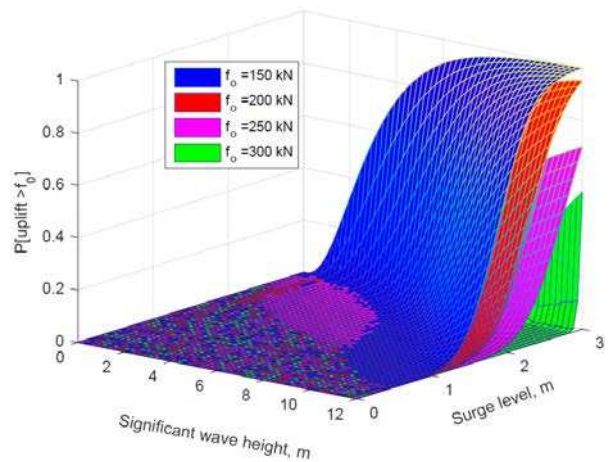


(b) two-story building

Figure 7-28. Fragility surfaces for shear during a 3-hour hurricanes



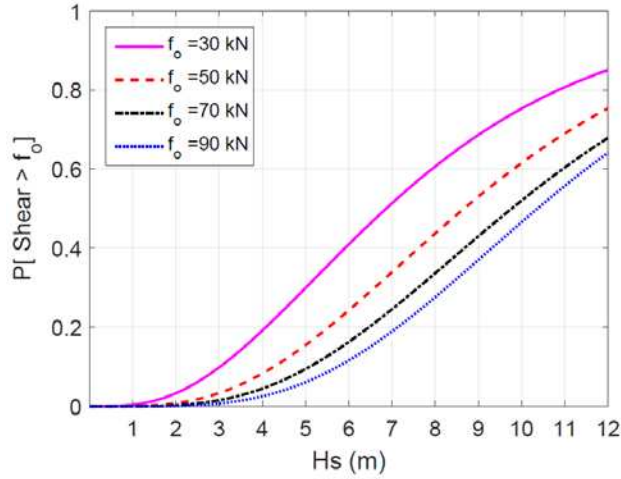
(a) one-story building



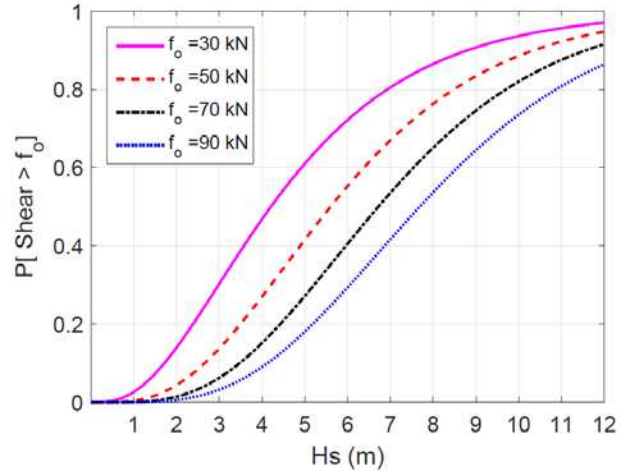
(b) two-story building

Figure 7-29. Fragility surfaces for uplift during 3-hour hurricanes

When the surge level set equal to a single value at 3.0m for example, fragility curve is obtained from fragility surfaces by taking a slide at that surge level, as shown in Figure 7-30 and Figure 7-31. These fragilities can be used for performance-based design as shown in the earlier bridge example.

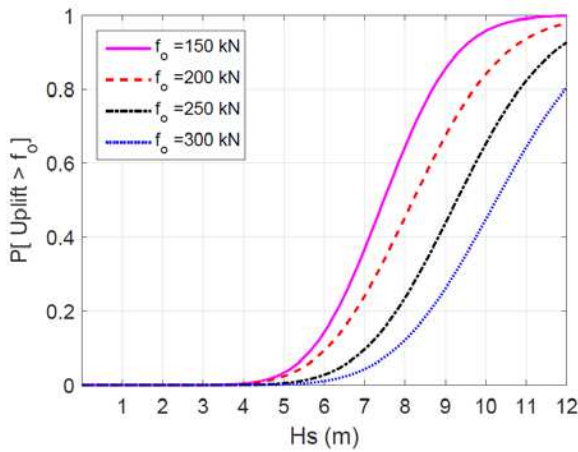


(a) one-story building

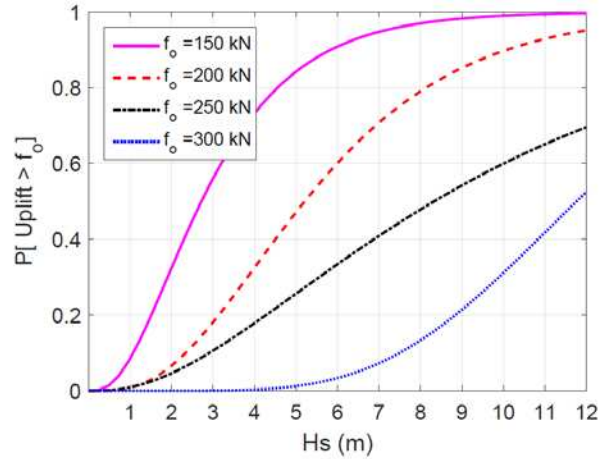


(b) two-story building

Figure 7-30. Fragility curves for shear at surge level of 3.0m during three-hour hurricanes



(a) one-story building,



(b) two-story building

Figure 7-31. Fragility curves for uplift at surge level of 3.0m during three-hour hurricanes

## Chapter 8 . SUMMARY, CONCLUSIONS, CONTRIBUTIONS, AND FUTURE WORK

This study examined the development of a performance-based design methodology for two fluid-structure interaction problems: wind and wind turbines, and hurricane waves and elevated coastal structures.

For the wind and wind turbine problem, a simplified coupled dynamic model was developed and used to compute the vibration of wind turbines for application in fatigue life problems and a fatigue-related design approach. Coupling time-domain analysis with a finite element model, the relative wind loading on the structure was determined at each time step. The simplified coupled dynamic model presented was used for this fatigue analysis under serviceability state design only which has limitations for other aerodynamic effects. An important assumption made in this study is that the tower base weld connection has no initial crack. After reaching its service life, which is defined by the S-N curve, a through-thickness crack was allowed to develop with its initial length double the tower wall thickness. If the crack is allowed to propagate to its critical length, the estimated fatigue life of the connection can be extended significantly. The tower was analyzed for both fracture damage due to fatigue and plastic collapse due to bending stresses. It is clear that the life time of wind tower is dominated by fatigue and fracture rather than by plastic collapse, as one would expect.

On the other hand, the computational demand of applying relative motion analysis in the time-domain for wind turbine blades is warranted since the along-wind motion velocity of blades is close to the wind velocity which therefore results in a significant change in the net wind loading on the structure. By applying relative motion analysis through Morison's equation, the fatigue life is shown to be longer since actual wind loading on the structure is reduced.

The method was applied to obtain fragility curves for application of performance –based design concepts to a typical 5-MW wind turbine. The resulting fragility curves can be used as design aids for selection of basic wind turbine design parameters based on a specific site location having a specific average mean wind speed.

The method then was applied for specific wind sites in Colorado. An assessment of wind power at different sites in Colorado was made by comparing the amount of harvested energy for a given fatigue life. The analyses showed that Eastern Colorado has more potential for wind turbine development which is supported by the fact that most wind farms in Colorado are currently located in the east side. In addition, the turbulence intensity of the wind velocity plays a very important role in evaluating the fatigue life of a wind turbine to the extent that it can overshadow the mean wind velocity itself. In addition, the minimum required steel for a turbine tower can be obtained at each combination of the tower thicknesses and diameters at different wind sites in Colorado by applying performance-based design.

For hurricane wave and elevated coastal structures problem, a performance-based design approach for elevated coastal structures when a prescribed extreme sea state is considered using fragility methodology. The closed-form numerical method for generating random shallow water waves from a target wave power spectrum and the distribution type was presented. Different hurricane sea states ( $H_s, T_p$ ) for deep water (the JONSWAP spectrum) were transformed to shallow water (TMA spectrum) at a 3 m depth where the hypothetical structure was located. The numerical generation method was validated itself by comparing the output and the input wave power spectrum and the distribution type. The benefit of this method is the generation of full scale waves, which typically cannot be replicated in a laboratory. By applying the coupled Eulerian-Lagrangian model for fluid/structure interaction in ABAQUS and ANSYS-Fluent, a

numerical water flume simulation was utilized. The fragility methodology was then explored to illustrate the ability to select from various design options (combinations of clearance height and capacity) to obtain a target probability of failure for a specified hurricane/sea state. The illustrative example for a coastal bridge and buildings design based on a target failure probability demonstrates how the concepts presented herein could be applied for performance-based design of coastal structures.

Several key contributions result from the work presented in this dissertation:

Contribution 1: The fragility methodology was refined and illustrated for complex fluid-structure interaction problems thereby providing a mechanism to extend these to full performance-based design when needed.

Contribution 2: The bridge and residential structures analyzed in Chapter 7 with some refinements represent archetypes for investigation of mitigation strategies in future analyses at a single building or community level.

Contribution 3: The fatigue life based design approach showed that there is significant fatigue life after crack initiation for wind turbine base connections.

Contribution 4: The coupled dynamic FEM model for the wind turbine using Morison's equation was able to capture the relative motion in the time-domain for wind turbine blades and the along-wind direction.

Recommended future work:

- 1- Develop a risk-informed design methodology by integrating the fragility curve with hazard curves for combined wave and surge to obtain the risk of a structure during its lifetime.

- 2- Develop predictive tools for hurricane loss by combining the developed fragility curve with hurricane track and surge levels for a specified coastal region or city.
- 3- Develop a model for wind-wave-surge for structures to investigate the response of structures under an actual hurricane event; there are regressive approaches but much of the statistics are not available at this point.
- 4- Investigate the community level response of buildings and utility facilities to hurricane wave and surge which can be used for community resiliency assessment.
- 5- Investigate the different wave angles reaching the structure and the effects of wave breaking on one structure to another structure.



## REFERENCES

- AASHTO. (2012). *AASHTO LRFD Bridge Design Specifications, 6th Edition - June 2012*. American Association of State Highway and Transportation Officials, Washington D.C.
- Aas-jakobsen, K., and Strommen, E. (2001). “Time domain buffeting response calculations of slender structures.” *Journal of Wind Engineering and Industrial Aerodynamics*, 89, 341–364.
- ABAQUS. (2011a). *Abaqus Analysis Users Manual. Formulation of Eulerian– Lagrangian contact Section 14.1.1. Abaqus Analysis Users Manual. Version 6.11.*, Dassault Systèmes, RI, USA.
- ABAQUS. (2011b). *Abaqus Analysis Users Manual. Version 6.11. Section 24.2.1. Equation of state. Abaqus User Manual. Version 6.11*, Dassault Systèmes, RI, USA.
- ANSYS. (2013). *ANSYS FLUENT User’s Guide 15.0 Release*. ANSYS, Inc., Canonsburg, PA.
- Atadero, R. A., van de Lindt, J. W., and Goode, J. S. (2008). *Characterization of wind Distributions for Fatigue Assessment of Structural Supports in Colorado*,. Colorado Department of Transportation Safety and Traffic Engineering Branch, Denver, CO.
- Bea, R. G., Xu, T., Stear, J., and Ramos, R. (1999). “Wave Forces on Decks of Offshore Platforms.” *Journal of Waterway, Port, Coastal, and Ocean Engineering (ASCE)*, 125 (3)(May/June), 136–144.
- Biéssel, F., and Suquest, F. (1951). “Les appareils générateurs de houle en laboratoire (Translated by St. Anthony Falls Hydrolic Lab, University of Minnesota, Report No. 39).” *La Houille Blanche*, 6(2,4 et 5).
- Bouws, E., Günther, H., Rosenthal, W., and Vincent, C. L. (1985). “Similarity of the Wind Wave

- Spectrum in Finite Depth Water, Part I-Spectral Form.” *Journal of Geophysical Research*, 90(C1), 975–986.
- Bozorgnia, M., Lee, J.-J., and Raichlen, F. (2011). “Wave Structure Interaction: Role of Entrapped Air on Wave Impact and Uplift Forces.” *Coastal Engineering Proceedings*, 1, 1–12.
- Bradner, C., Schumacher, T., Cox, D., and Higgins, C. (2011). “Experimental Setup for a Large-Scale Bridge Superstructure Model Subjected to Waves.” *Journal of Waterway, Port, Coastal, and Ocean Engineering (ASCE)*, 137:3(January/February), 3–11.
- Bradner, C., Schumacher, T., Cox, D. T., and Higgins, C. (2008). “Large-scale laboratory measurements of wave forces on highway bridge superstructures.” *31st International Conference on Coastal Engrg, ASCE*, 3554 – 3566.
- BS7910. (2005). “Guide to methods for assessing the acceptability of flaws in metallic structures.” BSI Group, London, UK.
- Chen, L. F., Zang, J., Hillis, A. J., Morgan, G. C. . . , and Plummer, A. R. (2014). “Numerical investigation of wave-structure interaction using OpenFOAM.” *Ocean Engineering*, Elsevier, 88, 91–109.
- Chen, X., Li, J., and Chen, J. (2009). “Wind-induced response analysis of a wind turbine tower including the blade-tower coupling effect.” *Journal of Zhejiang University SCIENCE A*, 10(11), 1573–1580.
- Chopra, A. K. (2012). *Dynamics of Structures - Theory and Applications to Earthquake Engineering*. Prentice-Hall International, Boston.
- Chung, H., Manuel, L., and Frank, K. H. (2003). *Optimal Inspection of Fracture-Critical Steel Trapezoidal Girders*. Report Number: FHWA/TX-04/0-2135-1. Texas Department of

Transportation, Austin Texas.

Como, A., and Mahmoud, H. (2013). “Numerical evaluation of tsunami debris impact loading on wooden structural walls.” *Engineering Structures*, Elsevier Ltd, 56, 1249–1261.

Cox, D. T., and Scott, C. P. (2001). “Exceedance probability for wave overtopping on a fixed deck.” *Ocean Engineering*, 28, 707–721.

Crandall, S. ., and Mark, W. D. (1963). *Random Vibrattion in Mechanical Systems. ASM Hanbook*, Academic Press, New York.

Cuomo, G., Shimosako, K. I., and Takahashi, S. (2009). “Wave-in-deck loads on coastal bridges and the role of air.” *Coastal Engineering*, Elsevier B.V., 56(8), 793–809.

Dawood, M., Goyal, R., Dhonde, H., and Bradberry, T. (2013). “Fatigue Life Assessment of Cracked High Mast Illumination Poles.” *Journal of Performance of Constructed Facilities*, (DOI: 10.1061/(ASCE)CF.1943-5509.0000438).

Deodatis, G., and Micaletti, R. C. (2001). “Simulation of Highly Skewness Non-Gaussian Stochastic Processes.” *Journal of Engineering Mechanics*, 127(December), 1284–1295.

Do, T. Q., Van de Lindt, J. W., and Mahmoud, H. (2015). “Fatigue Life Fragilities and Performance-Based Design of Wind Turbine Tower Base Connections.” *Journal of Structural Engineering*, ASCE, 141(7), 1–13.

Dowling, N. E. (2007). *Mechanical Behavior of Materials*. Pearson Prentice Hall, Upper Saddle River, New Jersey.

FEMA. (1996). *Performance-Based Seismic Design of Building (FEMA 283)*. *International Seminar on Sesmic Engineering for Tomorrow*, Federal Emergency Management Agency, developed by the UC Berkeley Earthquake Engineering Research Center, Washington D.C.

Frese, T., and Dalhoff, P. (2000). “Fatigue Analysis of Bolted and Welded Joints.” *NAFEMS*

- Seminar: Fatigue Analysis*, Wiesbaden, Germany, 1–18.
- Goda, Y. (2000). *Random Seas and Design of Maritime Structures*. World Scientific Publishing Co. Pte. Ltd., Singapore.
- Goode, J. S. (2007). “Correlated Wind Turbulence and Aeroelastic Instability Modeling for 3-D Time-Domain Analysis of Slender Structural Systems.” Colorado State University.
- Goode, J. S., and van de Lindt, J. W. (2006). “Development of a Reliability-Based Design Procedure for High-Mast Lighting Structural Supports.” *Structures Congress 2006, ASCE*, ASCE, St. Louis, MO, 1–10.
- Goode, J. S., and van de Lindt, J. W. (2007). “Development of a Semiprescriptive Selection Procedure for Reliability-Based Fatigue Design of High-Mast Lighting Structural Supports.” *Journal of Performance of Constructed Facilities*, 21(6), 193–206.
- Gramhry, E. (1963). *Wave forces on a dock, Technical Rep. No.HEL-9-1*. Berkeley, CA.
- Griffis, L. G. (1993). “Serviceability Limit States Under Wind Load.” *Engineering Journal, AISC*, 30(1), 1–16.
- Grigoriu, M. (1998). “Simulation of stationary non-gaussian translation processes.” *Journal of Engineering Mechanics Division, ASCE*, 124(2)(FEBRUARY), 121–126.
- Grigoriu, M. (2009). “Existence and construction of translation models for stationary non-Gaussian processes.” *Probabilistic Engineering Mechanics*, 24(4), 545–551.
- Hanaki, S., Yamashita, M., Uchida, H., and Zako, M. (2010). “On stochastic evaluation of S–N data based on fatigue strength distribution.” *International Journal of Fatigue*, Elsevier Ltd, 32(3), 605–609.
- Hasselmann, K., Barnett, T. P., Bouws, E., Carlson, H., Cartwright, D. E., Enke, K., Ewing, J. A., Gienapp, H., Hasselmann, D. E., Kruseman, P., Meerburg, A., Muller, P., Olbers, D. J.,

- Richter, K., Sell, W., and Walden, H. (1973). *Measurements of Wind-Wave Growth and Swell Decay during the Joint North Sea Wave Project (JONSWAP)*. Deutsches Hydrographisches Institut, Hamburg, Germany.
- Holmes, J. D. (2002). “Fatigue life under along-wind loading — closed-form solutions.” *Engineering Structures*, 24(1), 109–114.
- Holmes, J. D. (2004). *Wind Loading on Structures*. Spon Press, London, UK.
- Hughes, S. A. (1984). *The TMA Shallow-Water Spectrum Description and Applications*. Technical Report CERC-84-7, Vicksburg, Mississippi.
- IEC. (2005). *International Standard IEC 61400-1*. International Electrotechnical Commission, Geneva, Switzerland.
- IRENA. (2012). *Renewable Energy Technologies: Cost Analysis Series*. Issue 1/5, International Renewable Energy Agency, Bonn, Germany.
- Jeong, M.-S., Lee, I., Yoo, S.-J., and Park, K.-C. (2013). “Torsional Stiffness Effects on the Dynamic Stability of a Horizontal Axis Wind Turbine Blade.” *Energies*, 6(4), 2242–2261.
- Jiao, G., and Moan, T. (1990). “Probabilistic analysis of fatigue due to Gaussian load processes.” *Probabilistic Engineering Mechanics*, 5(2), 76–83.
- Jonkman, J., Butterfield, S., Musial, W., and Scott, G. (2009). *Definition of a 5-MW Reference Wind Turbine for Offshore System*. Report Number: NREL/TP-500-38060, National Renewable Energy Laboratory, Golden, CO.
- Jonkman, J. M., and Buhl Jr., M. L. (2005). *FAST User’s Guide*. Report number: NREL/EL-500-38230, National Renewable Energy Laboratory, Golden, CO.
- Kaplan, P. (1992). “Wave Impact Forces on Offshore Structures: Re-Examination and New Interpretations.” *Offshore Technology Conference*, Offshore Technology Conference,

- Houston, TX, 79–86.
- Kaplan, P., Murray, J. J., and Yu, W. C. (1995). “Theoretical analysis of wave impact forces on platform deck structures.” *Proceedings of the 14th International Conference on Offshore Mechanics and Arctic Engineering*, ASME, Copenhagen, Denmark, 189–198.
- Kennedy, A., Rogers, S., Sallenger, A., Gravois, U., Zachry, B., Dosa, M., and Zarama, F. (2011). “Building Destruction from Waves and Surge on the Bolivar Peninsula during Hurricane Ike.” *Journal of Waterway, Port, Coastal, and Ocean Engineering*, 137(3), 132–141.
- Kim, H., and Shields, M. D. (2015). “Modeling strongly non-Gaussian non-stationary stochastic processes using the Iterative Translation Approximation Method and Karhunen–Loève expansion.” *Computers & Structures*, 161(September), 31–42.
- Kitaigorodskii, S. A., Krasitskii, V. P., and Zaslavskii, M. M. (1975). “On Phillips’ Theory of Equilibrium Range in the Spectra of Wind-Generated Gravity Waves.” *Journal of Physical Oceanography*, 5, 410–420.
- Kooijman, H. J. T. (1996). *Bending-torsion coupling of a wind turbine rotor blade*, ECN-I-96-060. Netherlands.
- Kriebel, D. L., and Dawson, T. H. (1993). “Nonlinearity in Wave Crest Statistics.” *Proc. of the 2nd Int. Symp. on Ocean wave measurement and Analysis, Wave '93*, ASCE, New Orleans, Louisiana, 61–75.
- Kumar, K. S., and Stathopoulos, T. (1998). “Fatigue analysis of roof cladding under simulated wind loading.” *Journal of Wind Engineering and Industrial Aerodynamics*, 77-78(1 (September)), 171–183.
- Laino, D. J., and Hansen, A. C. (2001). *USER ’ S GUIDE to the Computer Software Routines*

*AeroDyn Interface for ADAMS*®. Salt Lake City, UT: Windward Engineering LLC,  
Prepared for the National Renewable Energy Laboratory under Subcontract No. TCX-9-  
29209-01.

- Lawrance, A. . J. ., and Lewis, P. . A. . W. . (2014). “Modelling and Residual Analysis of Nonlinear Autoregressive Time Series in Exponential Variables.” *Journal of the Royal Society, Series B*, 47(2), 165–202.
- Lee, D., Hodges, D. H., and Patil, M. J. (2002). “Multi-flexible-body Dynamic Analysis of Horizontal Axis Wind Turbines.” *Wind Energy*, 5(4), 281–300.
- Li, J., and Li, C. (2012). “Simulation of Non-Gaussian Stochastic Process with Target Power Spectral Density and Lower-Order Moments.” *Journal of Engineering Mechanics Division, ASCE*, 138(May), 391–404.
- Linton, D., Gupta, R., Cox, D., van de Lindt, J., Oshnack, M. E., and Clauson, M. (2013). “Evaluation of Tsunami Loads on Wood-Frame Walls at Full Scale.” *Journal of Structural Engineering, ASCE*, 139(8), 1318–1325.
- Luco, N., Kimball, J. K., Specialist, T., and Kircher, C. A. (2007). “Risk-Targeted versus Current Seismic Design Maps for the Conterminous United States.” *SEAOC 2007 CONVENTION PROCEEDINGS*, Structure Engineering Association of California, California, 1–13.
- Madsen, P. H., and Frandsen, S. (1984). “Wind-induced failure of wind turbines.” *Engineering Structures*, 6, 281–287.
- Mahmoud, H. N., and Dexter, R. J. (2005). “Propagation rate of large cracks in stiffened panels under tension loading.” *Marine Structures*, 18(3), 265–288.
- Manwell, J. F., MCGowan, J. G., and A.L. Rogers. (2009). *Wind Energy Explained- Theory, design and Application, Second Edition. The Royal Academic of Engineering*, John Wiley &

Sons, Ltd., Chichester, U.K.

Masters, F., and Gurley, K. R. (2003). “Non-Gaussian Simulation: Cumulative Distribution Function Map-Based Spectral Correction.” *Journal of Engineering Mechanics*, 129(12), 1418–1428.

Matsuichi, M., and Endo, T. (1968). “Fatigue of metals subjected to varying stress.” *Proc. Japan Soc. Mech. Engineering*, Tokyo.

Miner, M. A. (1945). “Cumulative damage in fatigue.” *Journal of Applied Mechanics*, 12, A159–A164.

Morgan, J. (2010). “Comparing Energy Costs of Nuclear , Coal , Gas , Wind and Solar.” <http://http://nuclearfissionary.com/2010/04/02/comparing-energy-costs-of-nuclear-coal-gas-wind-and-solar/>.

Mori, N., and Cox, D. T. (2003). “Statistical Modeling of Overtopping for Extreme Waves on Fixed Deck.” *Journal of Waterway, Port, Coastal, and Ocean Engineering*, 129(August), 165–173.

Morison, J. R. (1953). “The Force Distribution Exerted by Surface Waves on Piles.” *Technical Report Series 3, Issue 345*, Berkeley, CA.

Murtagh, P. J., Basu, B., and Broderick, B. M. (2004). “Wind force time-history generation by discrete Fourier transform ( DFT ).” *Multi-body dynamics-monitoring and simulation Techniques -III*, John Wiley & Sons, Ltd., New York, 147–154.

Murtagh, P. J., Basu, B., and Broderick, B. M. (2005). “Along-wind response of a wind turbine tower with blade coupling subjected to rotationally sampled wind loading.” *Engineering Structures*, 27, 1209–1219.

Newmark, N. M. (1959). “A Method of Computation for Structural Dynamics.” *Journal of the*



- Engineering Mechanics Division*, 85(7), 67–94.
- Nijssen, R. P. L. (2007). *Fatigue Life Prediction and Strength Degradation of Wind Turbine Rotor Blade Composites*. Delft, the Netherlands.
- Noda, M., and Flay, R. G. J. (1999). “A simulation model for wind turbine blade fatigue loads.” *Journal of Wind Engineering and Industrial Aerodynamics*, 83(1-3), 527–540.
- Ochi, M. K. (2003). *Hurricane-Generated Seas*. (R. Bhattacharyya and M. E. McCormick, eds.), Elsevier Ltd, Oxford, UK.
- Padgett, J., Desroches, R., Nielson, B., Yashinsky, M., Kwon, O., Burdette, N., and Tavera, E. (2008). “Bridge Damage and Repair Costs from Hurricane Katrina.” *Journal of Bridge Engineering, ASCE*, 13(January), 6–14.
- Paris, P., and Edorgan, F. (1963). “A Critical Analysis of Crack Propagation Laws.” *Journal of Fluids Engineering, ASME*, 85(4), 528–533.
- Quilligan, A., O’Connor, A., and Pakrashi, V. (2012). “Fragility analysis of steel and concrete wind turbine towers.” *Engineering Structures*, Elsevier Ltd, 36, 270–282.
- Reddy, J. N., and Gartling, D. K. (2010). *The finite element method in Heat Transfer and Fluid Dynamics*. CRC Press LLC, Boca Raton, FL.
- Repetto, M. P., and Solari, G. (2009). “Closed form solution of the alongwind-induced fatigue damage to structures.” *Engineering Structures*, Elsevier Ltd, 31(10), 2414–2425.
- Repetto, M. P., and Solari, G. (2010). “Wind-induced fatigue collapse of real slender structures.” *Engineering Structures*, Elsevier Ltd, 32(12), 3888–3898.
- Repetto, M. P., Solari, G., and Asce, M. (2012). “Closed-Form Prediction of the Alongwind-Induced Fatigue of Structures.” *Journal of Structural Engineering, ASCE*, 138(9), 1149–1160.

- Rosowsky, D. V., and Ellingwood, B. R. (2002). “Performance-Based Engineering of Wood Frame Housing: Fragility Analysis Methodology.” *Journal of Structural Engineering, ASCE*, 128(1), 32–38.
- Saravia, C. M., Machado, S. P., and Cortínez, V. H. (2013). “A composite beam finite element for multibody dynamics: Application to large wind turbine modeling.” *Engineering Structures*, 56, 1164–1176.
- Sarpkaya, T., and Isaacson, M. (1981). *Mechanics of Wave Forces on Offshore Structures*. Van Nostrand Reinhold Company, New York.
- Shields, M. D., and Deodatis, G. (2013a). “A simple and efficient methodology to approximate a general non-Gaussian stationary stochastic vector process by a translation process with applications in wind velocity simulation.” *Probabilistic Engineering Mechanics*, Elsevier, 31, 19–29.
- Shields, M. D., and Deodatis, G. (2013b). “Estimation of evolutionary spectra for simulation of non-stationary and non-gaussian stochastic processes.” *Computers and Structures*, Elsevier Ltd, 126(1), 149–163.
- Simiu, E., and Scanlan, R. H. (1986). *Wind Effects on Structures*. John Wiley and Sons, New York.
- Wang, H. (1970). “Water Wave Pressure on Horizontal Plate.” *Journal of the Hydraulics Division, ASCE*, 96(10), 1997–2017.
- Wiebe, D. M., Park, H., and Cox, D. T. (2014). “Application of the Goda Pressure Formulae for Horizontal Wave Loads on Elevated Structures.” *KSCE Journal of Civil Engineering, Korean Society of Civil Engineers*, 18, 1573–1579.
- Winterstein, S. R. (1988). “Nonlinear Vibration Models For Extremes and Fatigue.” *Journal of*

*Engineering Mechanics, ASCE*, 114(10), 1772–1790.

Winterstein, S. R., Ude, T. C., Bazzurro, P., and Cornell, C. A. (1996). “Ocean Environment Contours for Structural Response Analysis and Experiment Design.” *Probabilistic Mechanics and Structural and Geotechnical Reliability*, ASCE, Worcester, MA, 592–595.

Wiser, R., and Bolinger, M. (2013). “2012 Wind Technologies Market Report.” *U.S. Department of Energy, Office of Energy Efficiency and Renewable Energy*, Washington D.C., (August).

Xu, Y., Liu, T., and Zhang, W. (2009). “Buffeting-induced fatigue damage assessment of a long suspension bridge.” *International Journal of Fatigue*, Elsevier Ltd, 31(3), 575–586.

Yamazaki, F., and Shinozuka, M. (1988). “Digital Generation of Non-Gaussian Stochastic Fields.” *Journal of Engineering Mechanics Division, ASCE*, 114(7), 1183–1197.